The Search for the 2^+ Excitation of the ^{12}C Hoyle State using the ^{12}C(^{12}C,^{12}C[3α])^{12}C reaction

by

Tomás Muñoz-Britton

A thesis submitted to
The University of Birmingham
for the degree of
Doctor of Philosophy

School of Physics and Astronomy
The University of Birmingham
July 2011

Abstract

A search was conducted for the 2_2^+ excitation of the 7.65 MeV, 0_2^+, Hoyle state in ^{12}C using the ^{12}C(^{12}C,^{12}C[3α])^{12}C reaction. The analysis focussed primarily on the 9.7 MeV region in the ^{12}C excitation energy spectrum and no evidence of a resonance was found. Monte Carlo simulations were used to investigate the minimum strength at which a resonance would need to exist in order to be resolved by the experimental setup used. The possibility was also investigated that the 2_2^+ resonance may be observed in the ^{12}C(^{12}C,^{12}C[^{8}Be*+α])^{12}C reaction channel, though the methods contained within this thesis allowed only limited analysis of reaction channels involving non-zero spin states in the intermediate ^{8}Be nucleus; no evidence of a resonance was found. Further analysis of the 9.6 MeV and 10 MeV regions of the ^{12}C excitation energy spectrum also revealed no clear sign of a 2_2^+ resonance.

Acknowledgements

Having reached the completion of my thesis I have spent time reflecting on the support and encouragement that so many people have given to me over the years. Though there are far too many to mention everyone by name, I would like to pause and say thank you to a few individuals in particular who have helped in their own different ways throughout my career in physics thus far.

I must start by thanking my supervisor Martin Freer, who has shown endless patience in guiding and motivating me through my studies, something for which I am extremely grateful. That he has been able to pass on even a modicum of his knowledge and enthusiasm is a testament to his abilities as a physicist, mentor and teacher. Within the CHARISSA collaboration I also owe a huge debt of thanks to Neil Curtis and Nick Ashwood for showing me what life as an experimental physicist is all about, as well as for all their efforts in helping me with my analysis - surely a task which would have been the undoing of lesser men. I would like to thank Carl Wheldon for the help he has given me during my time as a PhD student and especially to his seemingly encyclopaedic knowledge of how to make XmGrace do quite what is required. I must also thank Victor Ziman for letting me anywhere near the group's computers, he is a brave man indeed. Beyond CHARISSA I must also say thank you to Garry Tungate, whose guidance stretches all the way back to my first days at the university and has always been appreciated, and to Peter Jones for letting me into the group in the first place.

I must also give a big mention to the various personalities with whom I have had the pleasure of sharing E320 - surely some of the finest and most upstanding reprobates a

man could ever wish to know. Though I cannot mention everyone by name I must say a particular thanks to Simeon Spencer for reminding me that all the greatest computer games were written prior to 1983, to Jonathan Malcolm for helping me understand that no matter what the question the answer is always beer, and to Matthew Barr for his unwavering support of my use of 'goto' loops.

Outside of the university I also owe a special debt of thanks to both Matt Tovey and Rich Clayton for all those evenings spent searching for happiness at the bottom of a whisky glass. Hopefully the fact that we have already found what we were looking for won't get in the way of us continuing to search for many years to come. Thanks too both to Megan and Frank for always keeping me full to the brim with so much fine food and all that even finer wine.

I would also like to say a special thanks to my family. I cannot find the words to convey just how grateful I am to my parents for their unwavering support and encouragement over the years and the belief they have instilled in me to always follow my own direction. There are few certainties in life, but without them I do know I could not have made it this far. I must also thank my little sister, 'Zanny', whose ongoing pride in my efforts is always both heartwarming and reassuring (even if possibly misplaced). Thanks Sis!

Finally, I must of course also thank Ro. Her love, her friendship and at times her patience is more than I could possibly deserve. Without her support I know this thesis would never have been written. Thank you Ro, for the happiness and laughter you have brought to the past ten years and for all those years yet to come.

For my parents.

Contents

List of Figures

List of Tables

Chapter 1

Introduction

The data presented in this thesis reflect a measurement of the sequential breakup of ^{12}C into 3α-particles through the ^{12}C(^{12}C,^{12}C[3α])^{12}C reaction and was carried out by the *Charissa* collaboration at the Australian National University (ANU) in 2005. It concerns the structure of ^{12}C above the 3α decay threshold and the belief that this is dominated by states with a 3α cluster structure. Chapter 1 of this thesis gives an overview of the history of studies into cluster structure in nuclei, and in particular cluster structure in so-called "α-conjugate" nuclei. A discussion is also included on the experimental motivation behind the analysis contained within this thesis, and the aims at the outset of the analysis.

1.1 Clustering in nuclei

The concept of the existence cluster structures within the nucleus was conceived in the earliest days of nuclear physics. The observation of spontaneous α-decay in the early 1900's led to the idea that the α-particle could pre-exist in the nucleus prior to decay [1]. The high binding energy of the ^{4}He nucleus, alongside the fact that the first excited state lies at 20.21 MeV, lent further weight to the suggestion that it could survive, relatively unperturbed, within the nucleus [2]. It was also noticed that light even-even 'N = Z' nuclei (^{8}Be, ^{12}C, etc.) have higher binding energies than 'non even-even' isotopes, which may reflect an internal α-particle structure.

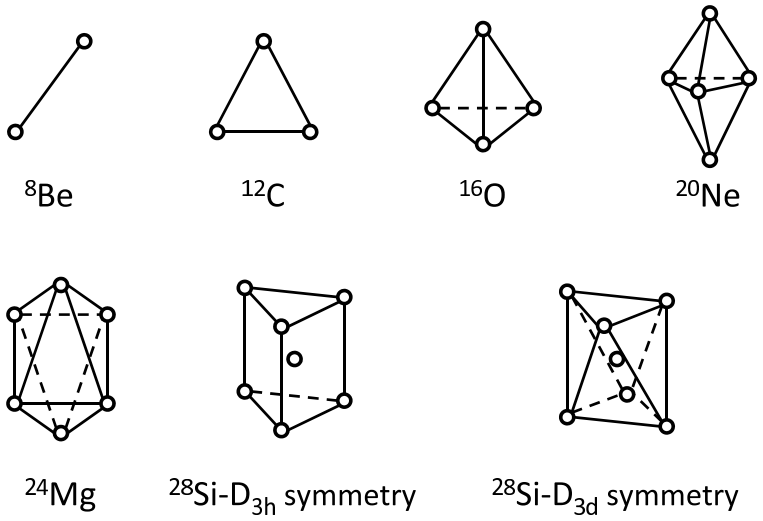

Figure 1.1: Crystalline structures in α-conjugate nuclei, as predicted by Brink [8].

Chadwick's discovery of the neutron [3], in 1932, resulted in α-clustering ideas becoming superceded as the single-particle nature of the nucleus became the focus, however a small part of the physics community continued to investigate the phenomenon and this work led to the development of the α-cluster model in the late 1930's [4, 5, 6]. In 1938, Hafstad and Teller developed an α-cluster model which particularly focused on A = 4n nuclei (known as 'alpha conjugate nuclei') [7] and investigated the link between the binding energy and number of interactions between α-particles. They concluded that the binding energy is proportional to the number of 'bonds' ($\alpha - \alpha$ pairs that can be formed) and predicted the geometric arrangements for various light α-conjugate nuclei (a dumbbell shape for ^{8}Be, an equilateral triangle for ^{12}C etc.). This paved the way for the geometrical model developed by Brink [8] (Figure 1.1), which replicates many of the structures suggested by Hafstad and Teller, and also Morinaga's 1956 postulate that α-particles within the nucleus should be able to arrange themselves into a linear configuration [9].

Early cluster models predicted ground states of nuclei would exist as geometric arrangements of α-particles. However, it was actually found that most nuclei have a more compact ground state in which any cluster structure is suppressed. In the late 1960's, Ikeda *et al.* [10] proposed that, for A = $4N$ nuclei (where N is the number of α-clusters), cluster structures would not be manifest in the ground state, but would become dominant in the energy region

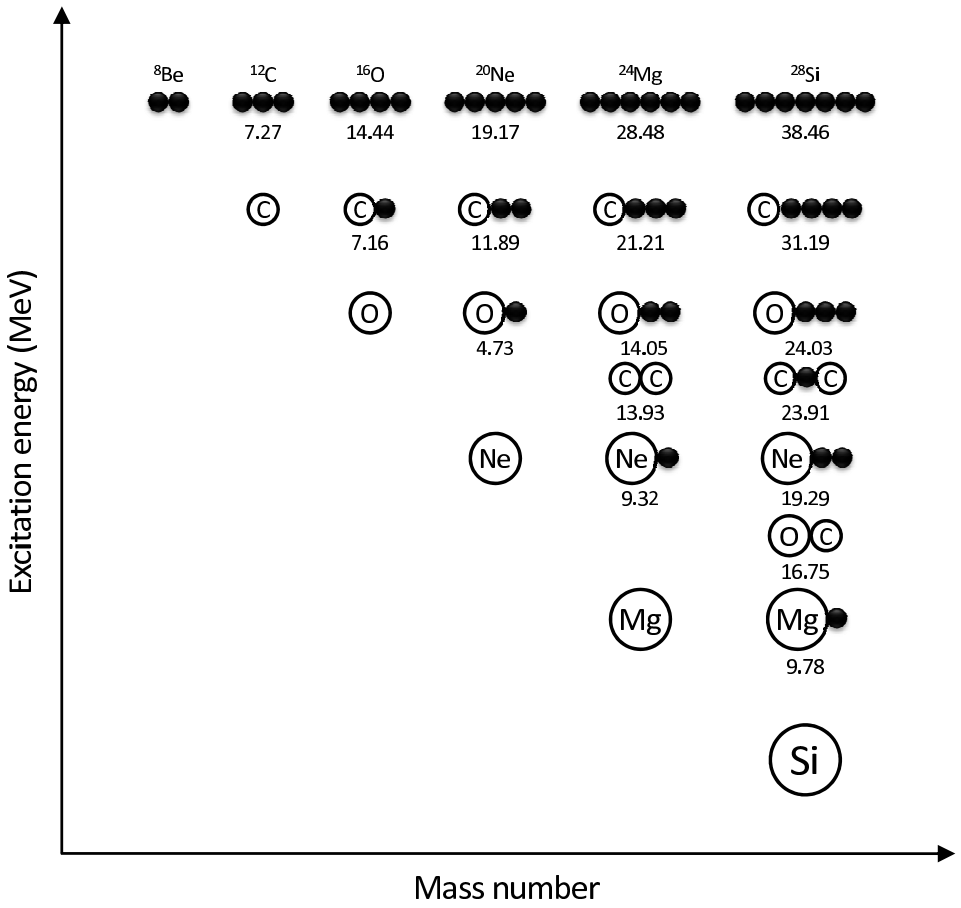

Figure 1.2: The 'Ikeda diagram' (from [11]), showing the development of cluster structure within α-conjugate nuclei as excitation energy is increased.

close to (and probably slightly below) the corresponding cluster decay threshold. The justification was based on the idea that as the excitation energy of a nucleus increases, the internal structure will be rearranged into structures that increase the binding energy of constituent clusters. The high binding energy of the ^{4}He nucleus means that as the excitation energy increases, an α-cluster will form outside of a *core* made up of the remaining nucleons. Since the core is also an A $= 4N$ nucleus this process can be repeated until the initial nucleus is separated entirely into α-particles and has formed an Nα structure. The α-particle break-up threshold lies at a point which requires minimal internal rearrangement to form the ejectile α-particle, i.e. close to the energy at which the nucleus has adopted a clustered structure. Figure 1.2 illustrates the cluster structures of A $= 4N$ nuclei up to and including A $= 28$.

In the following decade developments in theoretical methods allowed more sophisticated calculations, which predicted that as nuclear density falls to below one third of that at the

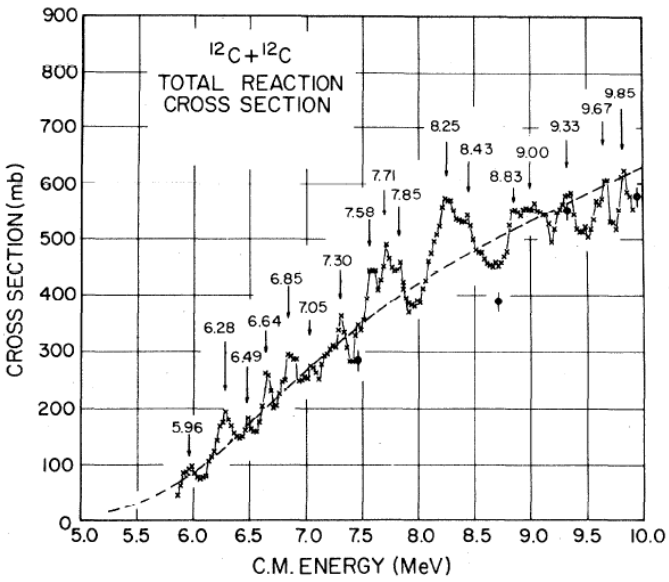

Figure 1.3: Excitation function for the ^{12}C + ^{12}C total reaction cross section as determined by Erb *et al.* [14]. The dashed line shows the theoretical prediction (which fails to reproduce the resonances seen in the experimental data).

centre of the nucleus, a phase change occurs causing the protons and neutrons to condense into α-particles [12]. This led to the suggestion that α-particles may be formed on the surface of nuclei, leading to the idea that a nucleus might be described as an α-particle orbiting a nuclear core (e.g. a ^{20}Ne nucleus could be described as an ^{16}O nucleus plus orbiting α-particle). Calculations performed on nuclei such as ^{16}O (^{12}C + α) were able to accurately reproduce experimental measurements such as α-decay widths and r.m.s. radii [13].

At about the same time, an increase in experimental efforts into the area of nuclear clustering began to confirm Ikeda's ideas. This evidence came, for example, from scattering experiments; the measurement of the total cross-section from the collision of two ^{12}C nuclei, as a function of beam energy, resulted in the appearance of a series of narrow resonances [14], as shown in Figure 1.3. This result was unexpected, as processes involving the collision of two nuclei typically result in a smooth variation in cross-section with changing energy. In addition, the narrow widths (typically $\sim$ 100 keV) indicated an interaction time of $\sim 10^{-21}$ s, which is significantly longer than that associated with a direct collision. It was therefore postulated that the two ^{12}C nuclei were trapped in a state described as a *molecular resonance*,

a ^{24}Mg nucleus existing as two interacting ^{12}C nuclei, orbiting one another. Further studies revealed a sequence of previously unknown resonances extending to an excitation energy of 60 MeV [14]. Perhaps the strongest evidence to support the idea of a nuclear molecule arose from considering that non-spherical structures gain energy from rotation. The rotational energy of a rigid body is given by

$$E = \frac{\hbar^2}{2\mathcal{I}} j\,(j+1) + E_0\ , \tag{1.1}$$

where $\mathcal{I}$ is the moment of inertia, j is the angular momentum and E_0 is the minimum energy of the rotating body for a given set of (rotational and vibrational) quantum numbers. In the nuclear case an increase in j corresponds to increasing the rotational energy of the nucleus, resulting in a rotational band. If the excitation energy of the states is plotted against $j\,(j+1)$ the gradient can be used to find the moment of inertia of the nucleus. When the spins of the resonances in the ^{12}C + ^{12}C scattering experiments were measured [15] they were found to increase with energy as would be expected for a pair of touching ^{12}C nuclei (figure 1.4). The multiplicity of states observed for a given spin, j, has been attributed to vibrational states superimposed upon the rotational modes [16].

1.2 Specific examples within light nuclei

1.2.1 Clustering in ^{8}Be

The ^{8}Be nucleus is perhaps the simplest example of α-clustering within nuclei, and is important as an example for cluster structure appearing from mean-field calculations. *Ab initio* approaches such as *ab initio* Greens function Monte Carlo (GFMC) calculations have been performed for the ^{8}Be nucleus [17], and predict a 2α clustered structure for the ground state (figure 1.5). This result is important as the calculations use all possible two-body and three-body nucleon-nucleon interactions, meaning that the interaction is not an effective one. The GFMC results show that a cluster structure in ^{8}Be arises directly from mean-field and does not require an underlying assumption of clustering to be included within a model. Models

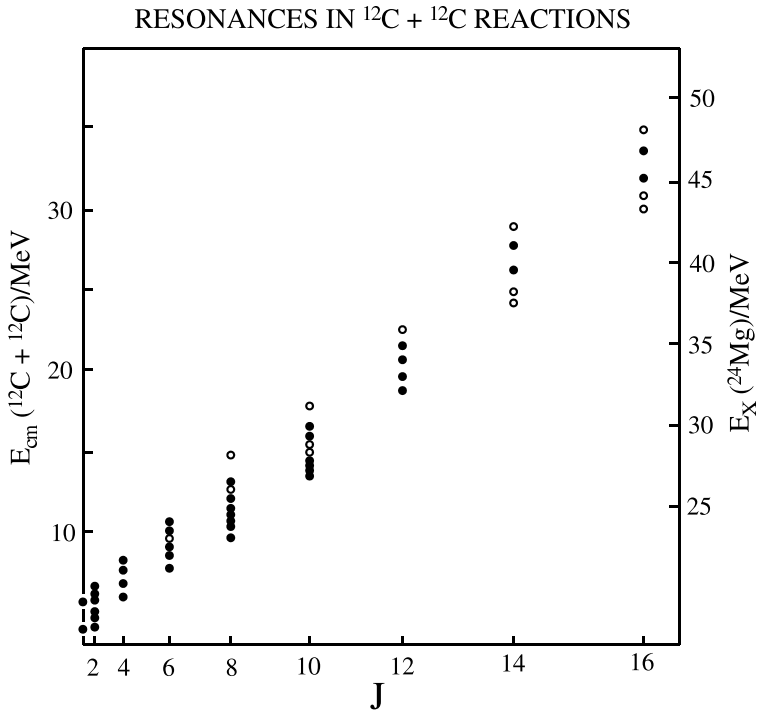

Figure 1.4: The energy-spin systematics of a ^{12}C + ^{12}C scattering measurement. The resonances increase with energy as would be expected for a rotational band with a moment of inertia consistent with a pair of touching ^{12}C nuclei (from [15]).

such as antisymmetrized molecular dynamics (AMD) (section 2.1.4) and fermionic molecular dynamics (section 2.1.5) are further examples of *ab initio* calculations which predict cluster structure within α-conjugate nuclei. Both are particularly relevant to the work contained within this thesis, as they have been extensively applied to investigating cluster structure within the ^{12}C nucleus [18, 19, 20].

1.2.2 The Hoyle state in ^{12}C

Beyond ^{8}Be, there remain many unanswered questions regarding the cluster structure of light nuclei, and in particular the ^{12}C nucleus. It is known that the ground state possesses a triangular triple-α symmetry, but lies far enough below the α-decay threshold so as its explicit cluster structure is reduced. The ground state thus possesses an oblate deformation and the first excited state at 4.44 MeV (2^+_1) and also the state at 14.08 MeV (4^+_1) are the corresponding rotational excitations. However, the second excited state at 7.65 MeV (0^+_2) is that of greatest interest, and also significance. Lying just above the α-decay threshold

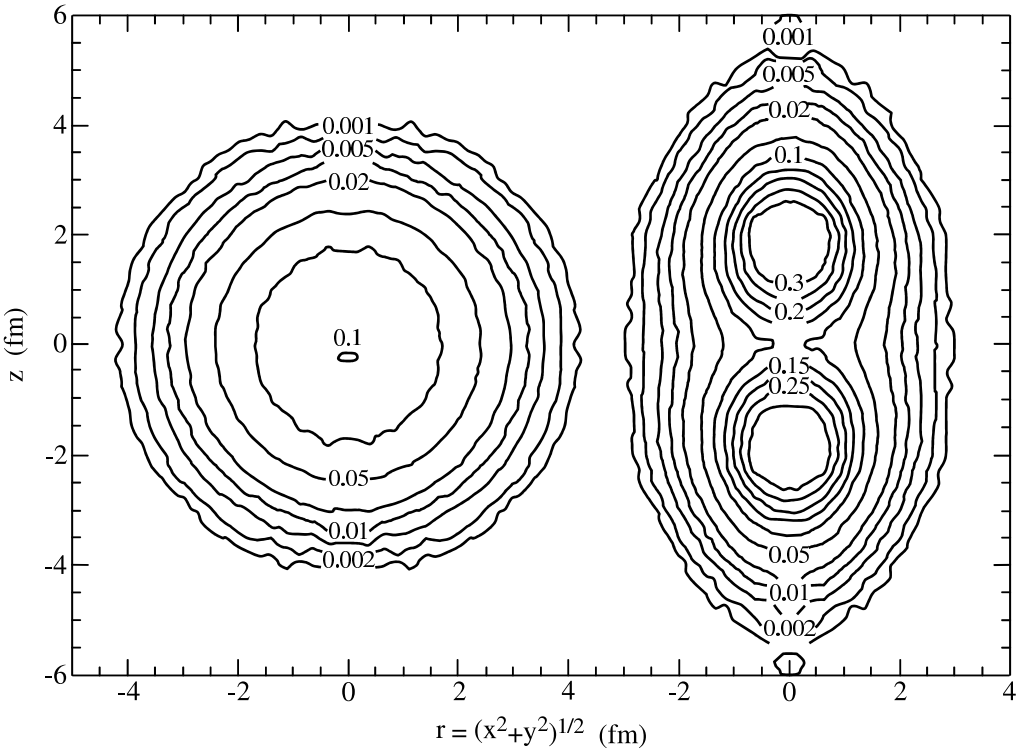

Figure 1.5: GFMC calculations of the density of ^{8}Be. The left- and right-hand images are the densities calculated in the laboratory and intrinsic frames, respectively [17].

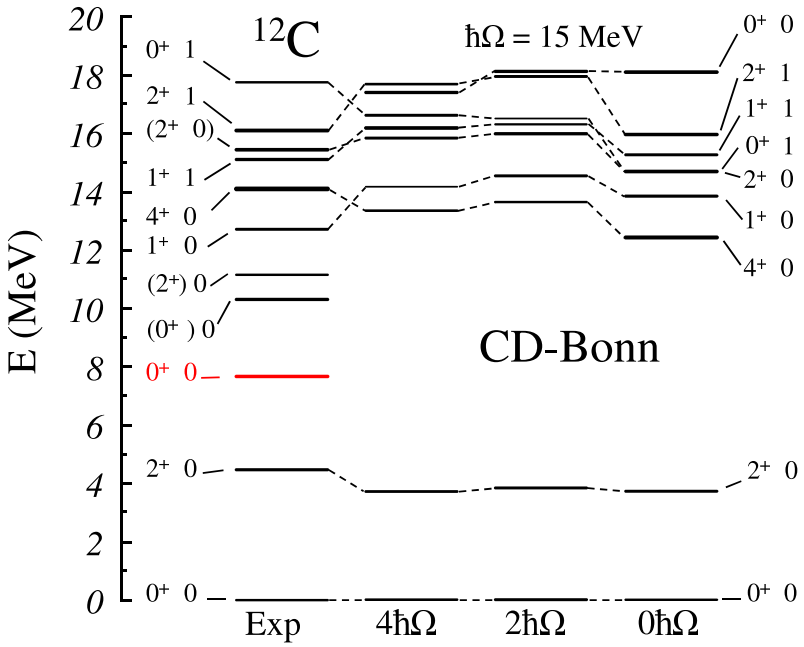

Figure 1.6: No core shell model calculations for ^{12}C. The left hand part shows experimental results; the state marked in red is the 0_2^+ "Hoyle" state at 7.65 MeV. Calculations using the CD Bonn N - N interaction with increasing numbers of oscillator orbits are shown on the right (from [21]).

($\sim$ 7.3 MeV) this resonance is not predicted by, e.g., the no-core shell model [21] (see Figure 1.6). The almost complete failure for shell models to predict the existence of this state suggests it has a distinctly different structure to the surrounding resonances, and it is indeed now known to have a strong clustered structure.

Perhaps one of the most well known resonances in nuclear physics, this state is referred to as the "Hoyle Resonance" and was first proposed by Fred Hoyle [22] in 1954 as a way to explain elements of stellar nucleosynthesis. ^{12}C plays a key role in the CNO cycle in stars, using hydrogen burning to produce helium through a series of (p,γ) reactions and β^+ emissions, as well as being important for the production of heavier elements. Neutron, proton and ^{4}He capture by ^{4}He all lead to the production of unstable nuclei which immediately decay and thus it was assumed that ^{12}C was formed by the coincident fusion of three α-particles. However, when the abundance of ^{12}C in the universe was measured, the observed amount could not be accommodated by such a three-body process. Hoyle proposed a process by which ^{8}Be (which has a lifetime of $\sim 10^{-16}$ s) could undergo an (α,γ) reaction and produce

^{12}C, and that a (0^+) resonance would exist at an energy of 7.65 MeV through which the capture should proceed. In line with Hoyle's prediction, within a few years, a 0^+ resonance was indeed found at 7.65 MeV [23].

The exact nature of the Hoyle state remains a topic for debate. It has been shown experimentally that this state has a large charge radius [24, 25], and for several years was thus believed to correspond to a linear chain of 3α-particles. However, problems arise with this interpretation. If the state is indeed a linear α-chain then a 2^+ rotational excitation of the state should exist in the region of $\sim$ 8.4 MeV [26], though the nearest 2^+ candidate lies several MeV higher in energy (at 11.16 MeV). This has led to the modification of the 3α-chain idea and suggestions that the actual configuration could instead be a bent chain or another similar configuration which possesses a suitably reduced moment of inertia [27, 28, 29]. The Hoyle state's large volume ($\sim$ 3-4 times larger than the ground state) has given rise to an alternative theoretical proposition. It is predicted that the increased volume will reduce the overlap of the α-particles and allow them to obtain their quasi-free characteristics in something approaching an α-particle gas, or bosonic condensate (BEC) [30]. It should be noted that although various models do indeed predict a system composed of weakly bound α-particles, the structure is found to be more complicated than that described by the strict definition of a BEC − further underlying structures are also predicted to exist and care must be taken not to take the BEC description too literally[1].

1.2.3 Clustering in ^{16}O and ^{20}Ne

Cluster structure in ^{16}O was a topic of interest from the earliest models. Hafstad and Teller modelled the nucleus as a tetrahedral arrangement of α-particles [7] (similar to that shown in figure 1.1), which would in turn be associated with a compact ground state in the Ikeda picture. From figure 1.2, the $\alpha + ^{12}$ C cluster structure should appear at 7.16 MeV, and the 4α-structure at 14.44 MeV. Of these, the 6.05 MeV, 0^+, state lies close to the $\alpha + ^{12}$ C break-up threshold (7.16 MeV) and the rotational characteristics of the state are well-represented

[1]Models such as Fermionic Molecular Dynamics (FMD), which predict such a structure, are discussed further in section 2.1.

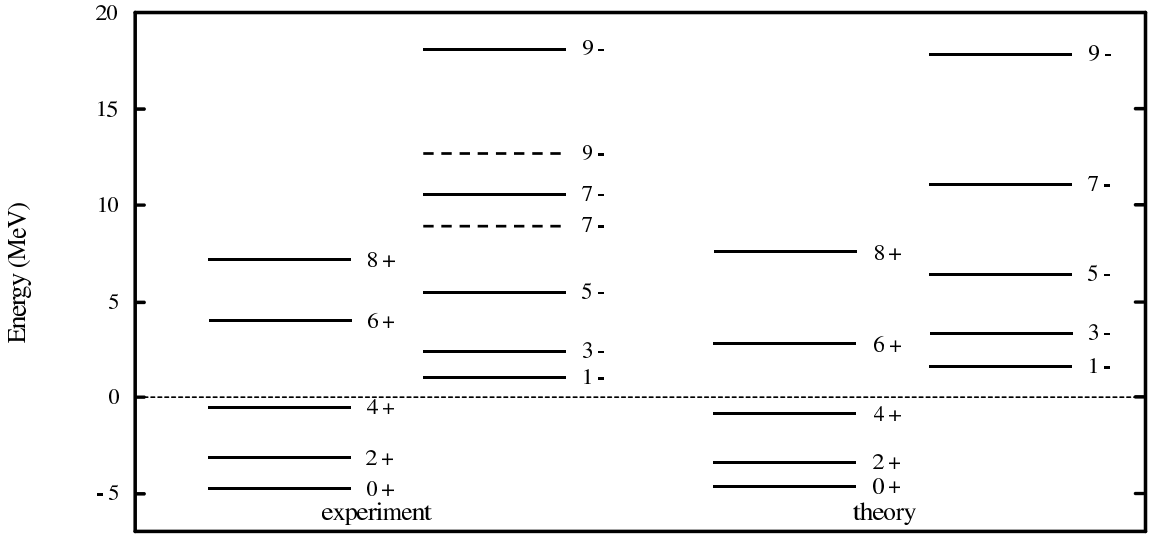

Figure 1.7: A comparison of the (positive and negative parity) experimental rotational bands in ^{20}Ne, and the α + core model predictions. The zero energy on the vertical axis is the α-decay threshold, 4.73 MeV. Adapted from [35].

by models such as, e.g., the α-cluster model[2] (ACM). Unlike the first excited state however, model predictions about the 4α configuration at 14.44 MeV remain a challenge to verify due to the challenge of studying the state experimentally. It might be expected that the break-up of a linear chain state in ^{16}O would result in two ^{8}Be nuclei, and this is the final state of the ^{12}C(α,^{8}Be) reaction – from which the final state experimental evidence for the linear structure comes [31, 32]. Unfortunately, measurements of other reactions which decay into two ^{8}Be nuclei in this region found there exists a broad spectrum of states [11], leaving the situation regarding definitive identification of chain-states in ^{16}O unclear.

Beyond ^{16}O, the ^{20}Ne nucleus has been cited as a good example of cluster structure in light nuclei [33, 34] and, in the case of the α + core model, ^{20}Ne can be represented by an α-particle+^{16}O nucleus. Given that both the α-particle and ^{16}O nucleus are closed shell-nuclei, it is perhaps unsurprising that the core + α model of Buck *et al.* [35] accurately predicts the energy levels of low-lying positive and negative parity bands seen in figure 1.7. Note that it is the mass asymmetry of an α+^{16}O ground state that results in an octupole

[2]The principles of which are discussed further in section 2.1.3.

parity doublet of $K^\pi = 0^\pm$ bands [36, 37], which occurs from the intrinsic structure not possessing good parity. It is also noteworthy that an alternative approach, in the form of anti-symmetrized molecular dynamics (AMD – discussed in more detail in chapter 2.1.4), is also capable of reproducing the cluster structure within ^{20}Ne [38]. The importance of the AMD approach lies in its freedom from any intrinsic clustering being assumed (i.e. there are no constraints on the arrangement of the individual nucleons). This level structure of $^{16}\mathrm{O} + \alpha$ states in ^{20}Ne has been confirmed experimentally in terms of bands [34, 39]; it has also been experimentally proven that these states possess large α-reduced widths, confirming their clustered nature [40].

1.3 Experimental motivation

Theoretical calculations for the 3α-chain of Ikeda's diagram would place a 2_2^+ excitation at 0.8 MeV above the Hoyle state [26], whereas FMD [20], BEC [41] and generator-coordinate method (GCM) [42] calculations put the energy at 1.3-2.8 MeV above the 0_2^+ state. It is predicted that the state should be broad [43], is thought to exist in a region dominated by other states, and has thus proven to be extremely difficult to observe experimentally. In 2004, Itoh *et al.* [44] published work describing an (α,α') scattering measurement which suggested tentative evidence of a state in the region $E_x \simeq 10$ MeV, though the poor energy resolution (150 keV) associated with the measurements mean this has not been widely accepted. More recently, a (p,p') scattering measurement performed at iThemba LABS by Freer *et al.* [45], with a much improved energy resolution (24 keV), also found evidence of a 2^+ resonance, this time at 9.6 MeV.

Whilst evidence exists to support the existence of a 2^+ resonance in the region E_x = 9-10 MeV, other measurements have been performed which suggest the state may lie outside of this region. In 2005, in an attempt to verify the accuracy of the NACRE (Nuclear Astrophysics Compilation of Reaction Rates) compilation of astrophysical reaction rates, Fynbo *et al.* used β-decay measurements from ^{12}N and ^{12}B to access various resonances in ^{12}C. In addition to dismissing the existence of a 2^+ resonance which had been thought

to exist at 9.1 MeV, they were unable to find any evidence of a 2^+ state anywhere below $\sim$ 14 MeV.

Though this latter experiment may initially suggest that a 2^+ resonance does not lie in the region of 9 - 10 MeV, it could also reveal the importance of selecting the 'correct' reaction channel in order to observe such a resonance. It is expected that the state will be only weakly populated in most reactions [45], and when this is combined with the large number of states lying at or near to 10 MeV, it may be the case that selection of the reaction channel is a key factor in finding evidence for a resonance. The predictions of various theoretical models, combined with previous experimental work, suggest that further investigation of the energy region around $E_x = 10$ MeV is required, and that attempting to populate the region through a number of different reaction channels is important. Previous work using the ^{12}C(^{12}C,^{12}C[3α])^{12}C reaction [46] strongly populates the Hoyle state and suggests it may be a suitable candidate reaction for finding an associated excitation.

1.4 Experimental aims

As discussed previously, several theoretical models predict the existence of the 2_2^+ excitation of the Hoyle state in ^{12}C, but its existence has yet to be substantively proven experimentally. The work presented in this thesis is a study of the ^{12}C(^{12}C,^{12}C[3α])^{12}C reaction (the inverse of the process by which ^{12}C is formed in stellar nucleosynthesis). Motivated by previous results, the aim of this work was to investigate whether evidence could be found for a 2^+ resonance in ^{12}C in the region of 9.7 MeV. The analysis was carried out using data gathered during an experiment previously performed at the Australian National University in April 2005.

Chapter 2 of this thesis discusses the theoretical aspects of some of the relevant nuclear models and also the techniques employed for the data analysis; Chapter 3 describes the experimental method and also the detection system used; in Chapter 4 the experimental analysis/results are presented; in Chapter 5 analysis of further decay channels, and a higher region in the ^{12}C excitation energy spectrum, is presented, and Chapter 6 provides a summary

of the work as well as an outline of future work in the field.

Chapter 2

Theoretical and Kinematic Details

Chapter 1 gave a brief overview of the history of the field of studies into nuclear clustering, as well as details of the Hoyle-state within ^{12}C and its significant role within stellar nucleosynthesis. Chapter 2 presents an overview of some of the theoretical models developed during the studies of nuclear clustering, and also the specific models especially relevant to the work contained within this thesis. It also describes the kinematics associated with the break-up technique and details about the angular correlations method used in the analysis.

2.1 Models of Nuclear Structure

2.1.1 The Nuclear Shell Model (and the Harmonic Oscillator)

The nuclear shell model, developed in the late 1940's, is perhaps one of the best known of all nuclear models, and although it may fail to predict states known to be heavily clustered in nature (section 1.2.2), is nonetheless a good starting point to describe cluster models. The nuclear shell model is in many ways analogous to the atomic shell model used to describe the way in which electrons are arranged in an atom. Both are based on the Pauli exclusion principle, requiring the filling of shells in order of increasing energy, and it was the experimental observation of these shells in nuclei that was the origin of the model. Figure 2.1 highlights experimental evidence of the same 'magic numbers' as those seen in atomic physics, revealing a sharp increase in both the 2n and 2p separation energies at the numbers associated with

shell closures.

Although similar to the atomic model, a major difference in the nuclear shell model is in the source of the potential in which the constituent particles move. While the potential for atomic electrons arises from the Coulomb field of the nucleus, and can hence be considered an external agent, the potential in which nucleons move is one which they themselves create. Another difference is the large size of nucleons, relative to the nucleus, and requires the need to consider issues such as nucleon-nucleon collisions being frequent compared to electron-electron collisions in the atomic model. The first of these considerations results in the main assumption of the shell model: that each nucleon moves in a potential created by all the other nucleons. By treating each individual nucleon in this manner, the nucleons can be ordered to occupy a series of energy levels, governed by the Pauli exclusion principle. If a collision were then to occur between two nucleons in a low lying energy level, it can be considered unlikely that either would receive sufficient energy to be transferred to the next-lowest empty position.

The selection of a suitable potential is a crucial parameter when constructing energy levels using the nuclear shell model, and one of the simplest available is the harmonic oscillator (i.e. a linear restoring force). Whilst known not to be accurate compared to more complicated potentials (e.g. the Wood-Saxon potential) when modeling higher energy levels, it is nonetheless a good choice for low-lying levels. The use of a potential term alone, however, fails to correctly replicate the observed magic numbers. To complete the model, a final term must be included in the form of a spin-orbit interaction. This results in a splitting of the energy levels, and in turn the well-known magic numbers to appear.

2.1.2 The Deformed Harmonic Oscillator (DHO) Model

Solving the three-dimensional Schrödinger equation for the harmonic oscillator potential results in the well-known energy levels

$$\mathrm{E} = \hbar\omega \left(\mathrm{n} + \frac{3}{2} \right) \ . \tag{2.1}$$

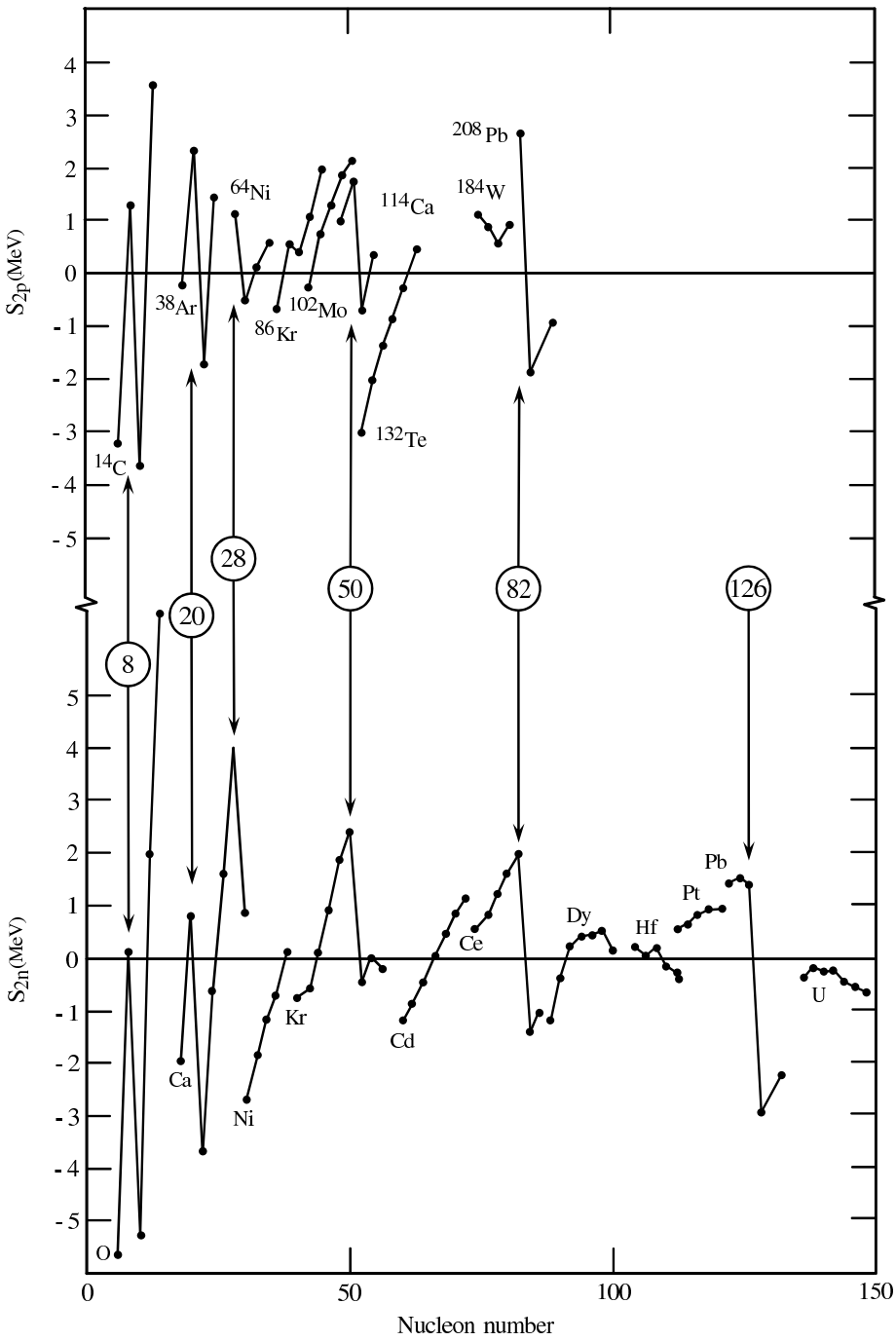

Figure 2.1: Top: two-proton separation energies of sequences of isotones (constant N); the lowest Z member of each band is noted. Bottom: Two-neutron separation energies of sequences of isotopes. The values plotted are the differences between the measured values and the values predicted by the semi-empirical mass formula. Figure from [47]; original data from [48].

If the nucleus/potential is stretched in one direction, e.g. the z-axis, in order to conserve the nuclear volume then it is necessary for the potential in the x- and y- directions to shrink accordingly. This increases the oscillation frequency perpendicular to the extension. This disappearance of the symmetry results in the oscillator frequencies for oscillations both perpendicular ($\perp$) and parallel (z) to the deformations being required to calculate the energy levels:

$$\mathrm{E} = \hbar\omega_{\perp}\mathrm{n}_{\perp} + \hbar\omega_{\mathrm{z}}\mathrm{n}_{\mathrm{z}} + \frac{3}{2}\hbar\omega_0 \ . \tag{2.2}$$

These are constrained by axial symmetry so that $\omega_0 = (2\omega_{\perp} + \omega_{\mathrm{z}})$[1], and the level of deformation can be identified by

$$\varepsilon = \varepsilon_2 = \frac{\omega_{\perp} - \omega_{\mathrm{z}}}{\omega_0} \ . \tag{2.3}$$

The energy levels of the deformed harmonic oscillator are shown in figure 2.2, the important feature being the shell structure which occurs at deformations of $(\omega_{\perp} : \omega_{\mathrm{z}})$ 2 : 1 (super-deformed) and 3 : 1 (hyper-deformed)[2]. When the sequence of spherical degeneracies (2, 6, 12, ...) is inspected then it is apparent that it is repeated twice at a deformation of 2 : 1 (2, 2, 6, 6, 12, 12, ...) and three times at 3 : 1. The idea of interacting potentials suggests that clustering may be an important feature, and the first $N\alpha$-cluster nucleus, ^{8}Be, can be used to investigate this. ^{8}Be is associated with the magic number 4 and, under the assumption that it has a 2α structure, this corresponds to a combination of spherical magic numbers 2 + 2 at a deformation of 2 : 1. Indeed, a super-deformed ground state is in good agreement with the experimental evidence for the structure of ^{8}Be [49, 50]. Many of the cluster configurations which are predicted by the DHO were previously predicted by the Ikeda diagram (figure 1.2). For example, the Ikeda diagram predicted a 3α state in ^{12}C lying close to the ^{8}Be + α break-up threshold (7.367 MeV), which can also be described by the DHO model as a hyper deformed 3α chain configuration. Combining the ideas of Ikeda with

[1]Note that a normalisation constant is required in order that equation 2.2 reduces to equation 2.1 in the limit of a very small deformation.

[2]Such degeneracies actually occur whenever the ratios $\omega_{\mathrm{x}} : \omega_{\mathrm{y}} : \omega_{\mathrm{z}} = a : b : c$ where *a, b* and *c* are integers. For the axially symmetric case of α-chain nuclei, such as the 3α state of ^{12}C in the the Ikeda diagram (figure 1.2), the ratio of $\omega_{\mathrm{x}} : \omega_{\mathrm{y}}$ is 1 : 1.

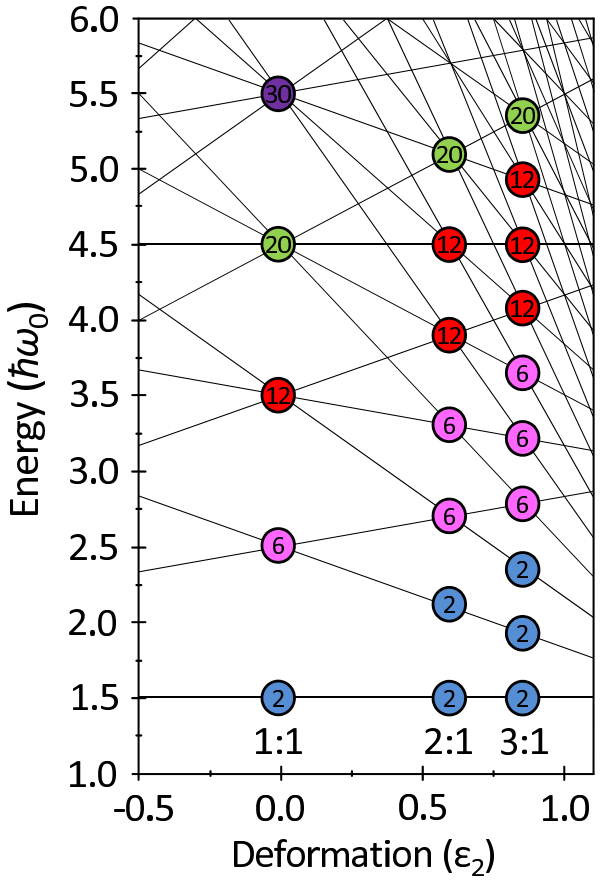

Figure 2.2: The energy level shifts of the deformed harmonic oscillator. At $2:1$ the nucleus is considered to be 'super-deformed', whilst at $3:1$ it is 'hyper-deformed'.

those of the DHO, one would expect to find clusters appearing not only at specific energies, but also specific deformations.

2.1.3 The Bloch-Brink Alpha Cluster Model

Brink's alpha cluster model was developed from earlier cluster models and was heavily influenced by the ideas of Bloch [11]. The principle idea is that pairs of protons and neutrons, coupled to a total angular momentum of zero, form 'quartets'. These quartets can then by modelled within the harmonic oscillator framework using

$$\phi_i(\mathbf{r}) = \sqrt{\frac{1}{\mathrm{b}^3\pi^{3/2}}}\exp\left[\frac{-(\mathbf{r}-\mathbf{R}_i)^2}{2\mathrm{b}^2}\right] , \tag{2.4}$$

in which $\phi_i(\mathbf{r})$ is a Gaussian wavefunction defining the α-particle, and where $\mathbf{R}_i$ is the vector describing the position of the ith α-particle and $\mathrm{b} = (\hbar/\mathrm{m}\omega)^{1/2}$ is a scale parameter determining the size of the α-particles. The $N\alpha$ wave function is created using a Slater determinant:

$$\Phi_\alpha(\mathbf{R}_1, \mathbf{R}_2, ..., \mathbf{R}_N) = K\mathcal{A}\prod_{i=1}^{N}\phi_i(\mathbf{R}_i) , \tag{2.5}$$

where $\mathcal{A}\prod_{i=1}^{N}\phi_i(\mathbf{R}_i)$ is the Slater determinant wave function ($\mathcal{A}$ is an antisymmetrization operator) and K is a normalisation constant. The α – α interactions are determined by an effective nucleon-nucleon interaction and Coulomb interaction and the optimal arrangement of the α-particles is arrived at variationally by optimising the locations and size of the α-particles. This model (sometimes modified to include additional 'cranking' terms) has been applied extensively to light cluster systems [26, 51], some interpretations of which are shown in figure 1.1.

2.1.4 The Antisymmetrized Molecular Dynamics (AMD) Model

Many light nuclei are known to have well-developed cluster structures and thus many theoretical models applied to them assume they possess potentials related to a specific cluster configuration. However, one must take care when doing this as assuming an underlying

cluster structure will undoubtedly give rise to results in which clustering is evident. One of the most significant advantages of the AMD approach is that there are no such assumptions made about cluster structure, consequently it is able to handle both shell-model-like states and also cluster states [18].

The AMD wave function of a nucleus explicitly includes the nucleon wave functions, which are antisymmetrized via a Slater determinant, and can be written

$$\Phi_{\mathrm{AMD}}\left(\mathbf{Z}\right) = \frac{1}{\sqrt{\mathrm{A!}}}\mathcal{A}\{\phi_1, \phi_2, ..., \phi_{\mathrm{A}}\}\ , \tag{2.6}$$

where the ϕ_i are Gaussian wave packets which possess spatial (Φ_{X_i}), spin (χ_i) and isospin (τ_i) information:

$$\phi_i = \Phi_{X_i}\chi_i\tau_i\ \ . \tag{2.7}$$

The wave function is parameterised by a complex set of variables $\mathbf{Z}$ which describe the spin and geometry of the wave function. The energy is calculated variationally using an *effective* nucleon-nucleon interaction and the structure then arises from the details of the interaction under the guidance of the Pauli exclusion principle.

An illustration of the emergence of clusters from the nucleon-nucleon within the framework of AMD is given by figure 2.3 for the beryllium isotopes from ^{6}Be to ^{14}Be. It is noticeable that when the neutron number is equal to the proton number (^{8}Be) then the separation of the proton cores is maximal (the clustering is at its maximum). This model has been applied to several nuclei (see [19]) and in general the model gives good agreement with experimental binding energies, transition rates, radii and moments [11].

2.1.5 The Fermionic Molecular Dynamics (FMD) Model

The FMD model shares many similarities with the AMD approach but includes an additional degree of freedom: a parameter allowing variation in the width of each individual wave packet (with each single-particle state being constructed from the superposition of two wave packets). The parameters of a single-particle FMD state are then arrived at in much the same

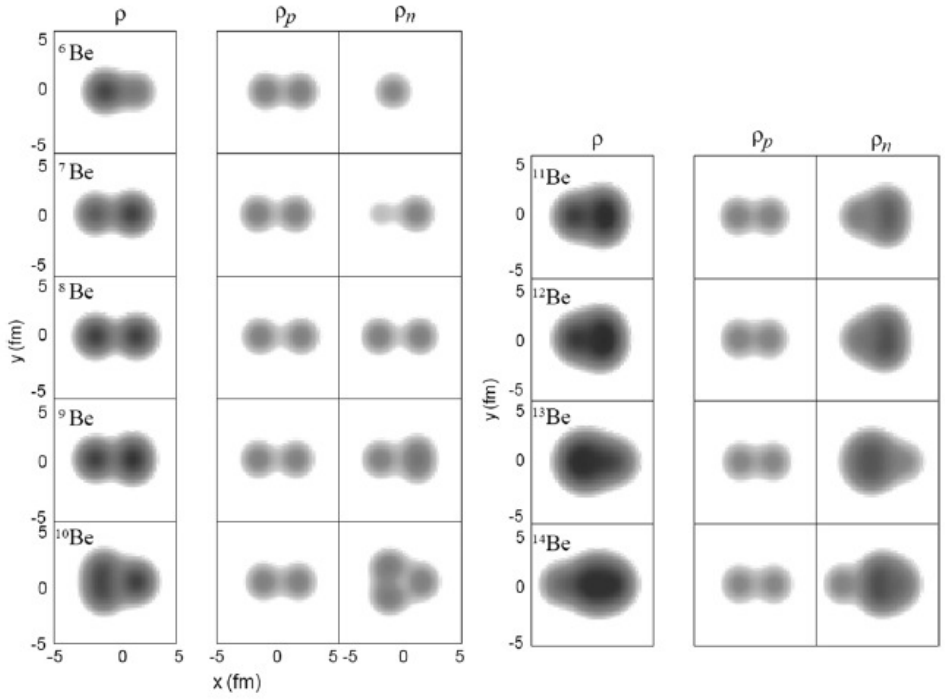

Figure 2.3: The density distributions of $^{6-14}$Be as calculated by the AMD model. From left to right the columns show the total nucleon density (ρ), proton density (ρ_p), and neutron density (ρ_n) (from [11]).

way as with AMD, i.e. by minimizing the intrinsic energy of the system using an effective potential. Unlike AMD, FMD however also includes a tensor force in the interaction used.

FMD calculations are of particular interest as they have been used extensively to model cluster states, and in particular the Hoyle state in ^{12}C. FMD cluster calculations are performed by constructing an α-cluster from the product of four Gaussian single-particle states which combine to a total spin and isospin of zero. Figure 2.4 show the results of FMD calculations performed by Chernykh *et al.* [20] for the Hoyle state in which a 3α structure is predicted to manifest in a ^{8}Be + α arrangement. This suggests care should be taken when considering that the 0_2^+ (and 2_2^+) may exist in a form analogous to a Bose-Einstein condensate (as discussed earlier) and the naive interpretation of a BEC must not be taken too literally (though the overlap of the wavefunctions in the 0_2^+ is nonetheless significant – as described in figure 2.4).

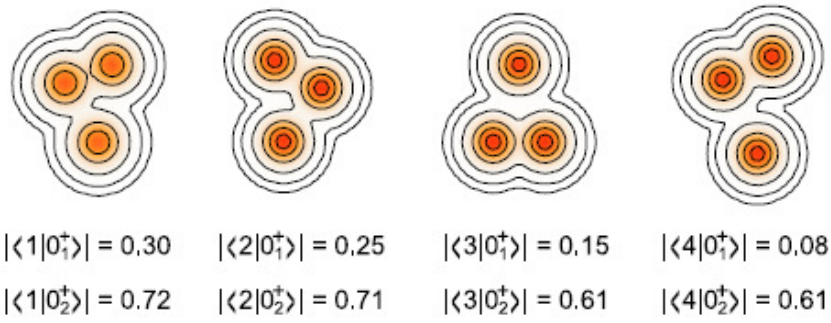

Figure 2.4: The density distributions of the four FMD states which most strongly contribute to the Hoyle state in ^{12}C. The text below indicates the respective amplitudes for the ground state (0_1^+) and the Hoyle state (0_2^+) (note that the FMD states are not orthogonal). (Adapted from [20].)

2.1.6 Summary of Nuclear Models

Cluster structure is a feature of nuclei which is problematic for many nuclear models, and heavily clustered states (such as the Hoyle state in ^{12}C) are often poorly represented, or completely missed by their predictions. Some models developed to represent these states, such as the DHO, are extensions of other well known models (in the case of the DHO, the SHO), extending them to effectively represent states known to have a clustered structure, though when a cluster structure is 'forced' into the model it is perhaps unsurprising that clustered states are an outcome. As interest in cluster structure has grown, so too have efforts in the associated models. Both AMD and FMD are approaches that make no specific allowances for nuclear clustering, yet are able to effectively predict both the existence and characteristics of states such as the Hoyle state.

Nonetheless, although models are becoming more more sophisticated in their approach to clustered states, there is much still to be discovered. Empirical confirmation of the energy of states such as the 2_2^+ resonance in ^{12}C will not only help in the understanding of the structure of the Hoyle state, but also in the development of the various models used to predict clustered states.

2.2 Kinematics and Break-up Reactions

2.2.1 Reconstructing the ^{12}C break-up nucleus

The experiment described within this thesis involves the study of a sequential break-up reaction: a beam particle, 'A', is incident on a target nucleus, 'B'. The two particles react in some manner and then produce two reaction products, A* and B*.

$$\mathrm{B}\,(\mathrm{A}, \mathrm{A}^*)\,\mathrm{B}^* \,. \tag{2.8}$$

If either of the reaction products is produced in a state with an excitation energy greater than the particle decay threshold for break-up ($\mathrm{E_{th}}$), then these will decay into further fragments in preference to γ-decay [52]. The threshold for the decay of ^{12}C into ^{8}Be and an α-particle lies slightly below the 0_2^+ (7.654 MeV) Hoyle state at 7.367 MeV. In the case of inelastic break-up reactions, A* has energy above the decay threshold and will thus decay into two daughter nuclei $\mathrm{C_1}$ and $\mathrm{C_2}$:

$$\mathrm{B}\,(\mathrm{A}, \mathrm{A}^* \rightarrow \mathrm{C_1} + \mathrm{C_2})\,\mathrm{B}^* \,. \tag{2.9}$$

In the ^{12}C(^{12}C,^{12}C*)^{12}C(g.s.) reaction, the ^{12}C* will decay into a ^{8}Be and an α-particle. The ^{8}Be can be formed in a number of excited states, but even the ground state is unbound by 92 keV against decay into 2α-particles. Any ^{12}C* which has an energy greater than $\mathrm{E_{th}}$ will therefore be detected as a 3α-particle jet.

Such a reaction is subject to a number of conservation laws and an important one involved in the current analysis is the Q-value of the reaction. This is defined as the difference of the initial rest mass energy minus the final rest mass energy:

$$\mathrm{Q} = (\mathrm{m_{initial}} - \mathrm{m_{final}})\,\mathrm{c}^2 \,. \tag{2.10}$$

However, in the case of the ^{12}C(^{12}C,^{12}C*)^{12}C(g.s.) reaction only the final state particles can be detected. Typically for the analysis used within this thesis a ^{12}C nucleus and 3α-particles

are the final-state particles and it is necessary to reconstruct the $^{12}C^*$ nucleus by kinematic considerations.

The energy of the $^{12}C^*$ nucleus can be calculated by first considering its momentum, $\mathbf{P}$, which can be calculated from the 3 detected α-particles using:

$$P^2 = \left(\sum_{i=1}^{3} \mathbf{P}_{\alpha_i x}\right)^2 + \left(\sum_{i=1}^{3} \mathbf{P}_{\alpha_i y}\right)^2 + \left(\sum_{i=1}^{3} \mathbf{P}_{\alpha_i z}\right)^2 , \tag{2.11}$$

where $\mathbf{P}_{\alpha_i}$ in the x-, y- and z-directions are the α-particle momentum components. The excitation energy of the parent $^{12}C^*$ nucleus is calculated using:

$$E_{ex} = \sum_{i=1}^{3} E_{\alpha_i} - \frac{P^2}{2M_C} + E_{th} , \tag{2.12}$$

where E_{ex} is the excitation energy of the $^{12}C^*$ nucleus, E_{th} is the break-up threshold energy, E_{α_i} are the energies of the 3α-particles, and M_C is the mass of the ^{12}C.

The above properties result in a detection system that was required to be able to detect the position, energy, and momentum of each hit. For the analysis contained within this thesis, this was achieved by using a system which could detect both the energy and position of a hit, and was also capable of separating events depending on the mass of the particle detected (see section 4.1.1); the momentum of each detected particle was then calculated using the measured energy, mass and emission angle.

2.2.2 Reconstructing the ^{12}C recoil nucleus

Upon detecting the three final-state α-particles, it is also possible to reconstruct the properties of the undetected ^{12}C nucleus by considering conservation of momentum. In directions perpendicular to the beam (x- and y- directions) the total momentum of the system must be zero both before and after the reaction:

$$P_{x,y} = \sum_{i=1}^{3} (P_{\alpha_i})_{x,y} + (P_{recoil})_{x,y} = 0 , \tag{2.13}$$

and thus

$$\left(\mathrm{P_{recoil}}\right)_{\mathrm{x,y}} = -\sum_{i=1}^{3}\left(\mathrm{P}_{\alpha_i}\right)_{\mathrm{x,y}} \ . \tag{2.14}$$

The beam energy, and hence its momentum, is known (and is entirely in the z-direction) and so the missing z-momentum can also be calculated:

$$\mathrm{P_z} = \sum_{i=1}^{3}\left(\mathrm{P}_{\alpha_i}\right)_{\mathrm{z}} + \left(\mathrm{P_{recoil}}\right)_{\mathrm{z}} = \mathrm{P_{beam}} \ , \tag{2.15}$$

and thus

$$\left(\mathrm{P_{recoil}}\right)_{\mathrm{z}} = \mathrm{P_{beam}} - \sum_{i=1}^{3}\left(\mathrm{P}_{\alpha_i}\right)_{\mathrm{z}} \ . \tag{2.16}$$

Knowledge of the recoil momentum allows the kinetic energy of the recoil particle to be calculated:

$$\mathrm{E_{recoil}} = \frac{\left(\mathrm{P_{recoil}}\right)^2}{2\mathrm{M_C}} \ , \tag{2.17}$$

where $\mathrm{P_{recoil}}^2$ is the sum of the squares of the x, y and z momentum components from equations 2.14 and 2.16.

2.3 Angular Correlations

Angular correlation calculations are a powerful tool for determining information on the spin of systems which decay into two fragments. The technique is based on the determination of the angles from two different stages of the reaction process (see figure 2.5). It is a requirement of the technique that all particles except for the ^{12}C* (B*) are formed in a spin zero state. The angle θ^* describes the centre-of-mass emission angle of the excited ^{12}C nucleus, measured with respect to the beam axis. The second angle, ψ, corresponds to the emission angle of the first α-particle in the centre-of-mass frame of the ^{12}C nucleus, again measured with respect to the beam axis. As all of the initial and final-state particles are spin zero, then for a scattering angle $\theta^* = 0$ the ^{12}C excited state is constrained to be populated in the $m = 0$ magnetic substate. The subsequent α-particle emission thus follows that of a squared

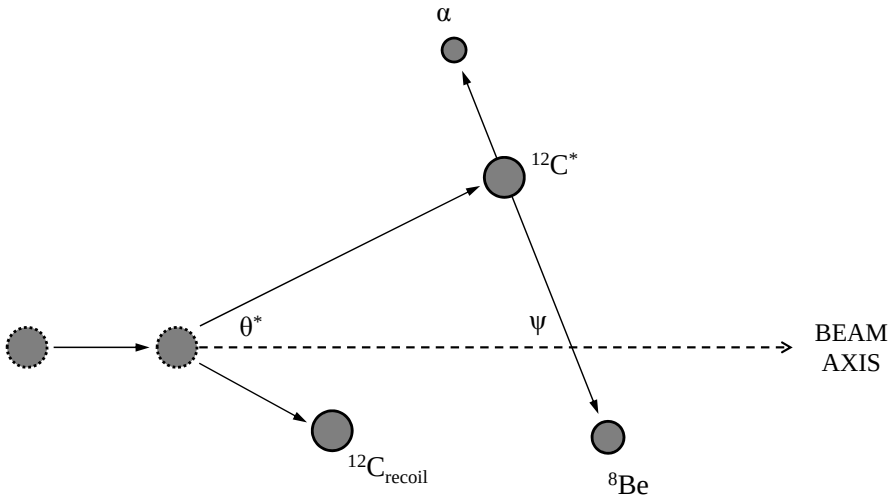

Figure 2.5: The definition of the correlation angles θ^* and ψ used in the present analysis (from [53]).

Legendre polynomial of order J (the spin of the state in ^{12}C):

$$\mathrm{W}(\psi)\Big|_{\theta^*\approx 0} \propto \left|\mathrm{P}_{J_\mathrm{B}}(\cos\psi)\right|^2 \ . \tag{2.18}$$

Away from $\theta^* = 0$ other m-substates may contribute which gives rise to a phase shift in the Legendre polynomial,

$$\mathrm{W}(\psi)\Big|_{\theta^*} \propto \left|\mathrm{P}_{J_\mathrm{B}}(\cos(\psi + \Delta\psi))\right|^2 \ , \tag{2.19}$$

where

$$\Delta\psi = \Delta\theta^* \frac{l_i - J}{J} \ . \tag{2.20}$$

Here l_i is the entrance channel grazing angular momentum [54]. This results in a ridge structure in the $\theta^* - \psi$ plane. Thus, the angular correlation spectrum is characterized by the spin of the state both in terms of the frequency of the oscillations as a function of ψ and also the gradient of the loci in the $\theta^* - \psi$ plane [53].

A brief discussion of the derivation of the angular correlations measurement technique is given in appendix A; a more detailed discussion of the technique can be found in [53].

2.3.1 Initial calculations of θ^* and ψ

As discussed previously, the analysis contained within this thesis involves that of ^{12}C via a break-up reaction in which the three final-state α-particles are detected. However, the angular correlation technique described in section 2.3 requires calculations involving the break-up of the $^{12}C^*$ nucleus into $^8\mathrm{Be} + \alpha$. For this reason, prior to calculating θ^* and ψ it is necessary to reconstruct the ^{8}Be nucleus; the technique used to do this is discussed in section 4.1.4. It is also necessary to determine the momenta of the ^{8}Be and α-particle, and the technique used to do this is discussed in section 3.1.5. Initial calculations of θ^* and ψ were performed under the assumption that they occurred in the x$-$z plane. The calculations of θ^* and ψ are detailed in figure 2.6.

The angle θ^* can be calculated from

$$\theta^* = \tan^{-1}\left(\frac{\mathrm{p_{C_x}}}{\mathrm{p_{C_{z_{cm}}}}}\right) , \tag{2.21}$$

where $\mathrm{p_{C_x}}$ is the x-momentum of the ^{12}C, and $\mathrm{p_{C_{z_{cm}}}}$ is the z-momentum of the ^{12}C in the centre-of-mass frame; $\mathrm{p_{C_{z_{cm}}}}$ is calculated from $\mathrm{p_{C_z}}$ using:

$$\begin{aligned} \mathrm{p_{C_{z_{cm}}}} &= \frac{\mathrm{m_C}\sqrt{2\mathrm{m_C}\mathrm{E_{beam}}}}{2\mathrm{m_C}} - \mathrm{p_{C_z}} , \\ &= \frac{\sqrt{2\mathrm{m_C}\mathrm{E_{beam}}}}{2} - \mathrm{p_{C_z}} , \end{aligned} \tag{2.22}$$

where $\mathrm{m_C}$ is the mass of ^{12}C, and $\mathrm{E_{beam}}$ is beam energy (101.5 MeV).

To calculate ψ, it is first necessary to find the relative x- and z-components of the velocities of the ^{8}Be and α-particle:

$$\mathrm{v_{rel_x}} = \frac{\mathrm{p_{\alpha_x}}}{\mathrm{m_\alpha}} - \frac{\mathrm{p_{Be_x}}}{\mathrm{m_{Be}}} , \tag{2.23}$$

$$\mathrm{v_{rel_z}} = \frac{\mathrm{p_{\alpha_z}}}{\mathrm{m_\alpha}} - \frac{\mathrm{p_{Be_z}}}{\mathrm{m_{Be}}} . \tag{2.24}$$

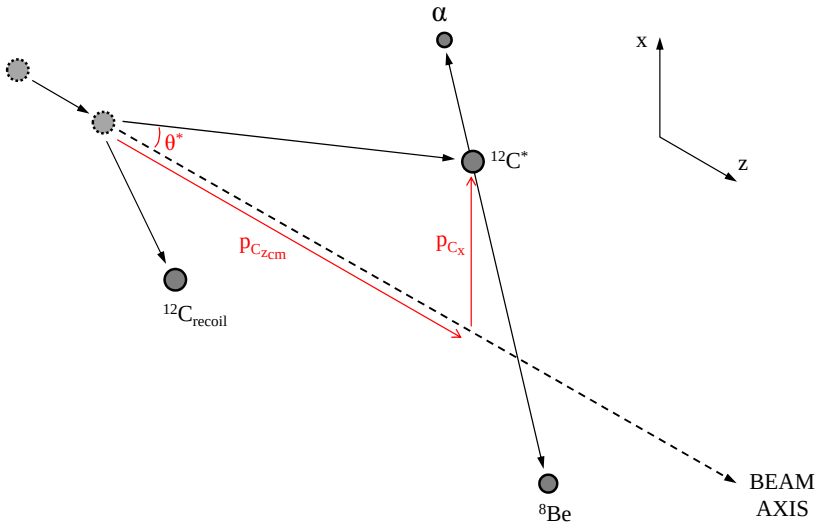

(a) Quantities required to calculate θ^*.

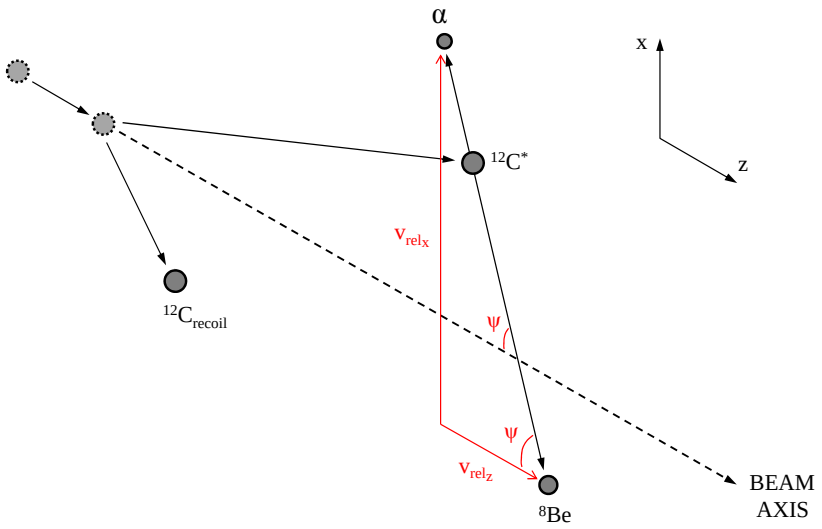

(b) Quantities required to calculate ψ.

Figure 2.6: Details of θ^* and ψ when calculated in the x − z plane.

The angle ψ is then given by

$$\psi = \tan^{-1}\left(\frac{\mathrm{v_{rel_x}}}{\mathrm{v_{rel_z}}}\right) . \tag{2.25}$$

It is worth noting that the choice of whether ψ is calculated with respect to the α-particle or the ^{8}Be nucleus is an arbitrary one as this will only affect the direction of the ridges.

2.3.2 Calculating θ^* and ψ in the (^{12}C*) breakup plane

A significant improvement in the angular correlations calculations can be achieved by rotating the plane in which θ^* and ψ are calculated. The calculations discussed in section 2.3.1 are based on the assumption that the reaction occurs in the $\mathrm{x}-\mathrm{z}$ plane, and while this is a good approximation, performing the calculations in the breakup plane of the ^{12}C* will result in enhanced clarity of the spin-dependent ridge structure of the $\theta^* - \psi$ plane.

To calculate θ^* in the breakup plane the x-momentum, $\mathrm{p_{C_x}}$, used in equation 2.21 must be substituted for the correct $\mathrm{x}-\mathrm{y}$ momentum dependant on the breakup plane. This is done by considering both the x- and y-momenta of the ^{12}C nucleus and then scaling and rotating $\mathrm{p_{C_x}}$ (the intermediate angles used for the rotations are shown in figure 2.7). The magnitude of $\mathrm{p_{C_{xy}}}$ is given by:

$$\mathrm{p_{C_{xy}}} = \frac{\mathrm{p_{C_x}}}{|\mathrm{p_{C_x}}|}\sqrt{\mathrm{p_{C_x}}^2 + \mathrm{p_{C_y}}^2} , \tag{2.26}$$

where $\mathrm{p_{C_y}}$ is calculated in the same way as $\mathrm{p_{C_x}}$ and $\mathrm{p_{C_z}}$ in equations 2.23 and 2.24. At this stage $\mathrm{p_{C_{xy}}}$ is in the same direction as $\mathrm{p_{C_x}}$, and so the angle of rotation into the breakup plane must still be calculated. This is done via two intermediary angles, τ_{r_1} and τ_{r_2}:

$$\tau_{\mathrm{r}_1} = \sin^{-1}\left(\frac{\mathrm{p_{C_y}}}{\mathrm{p_{C_{xy}}}}\right) , \tag{2.27}$$

and

$$\tau_{\mathrm{r}_2} = \tan^{-1}\left(\frac{\mathrm{v_{rel_y}}}{\mathrm{v_{rel_x}}}\right) . \tag{2.28}$$

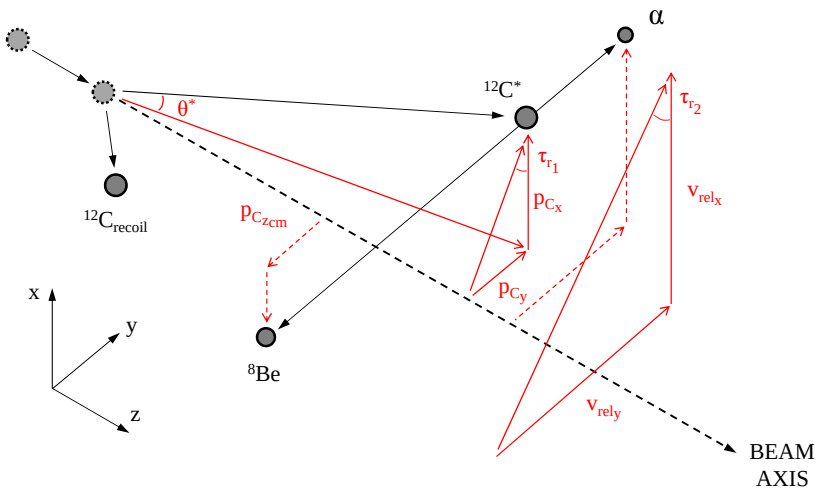

(a) Quantities required to calculate θ^* after rotating into the $^{12}C^*$ breakup plane.

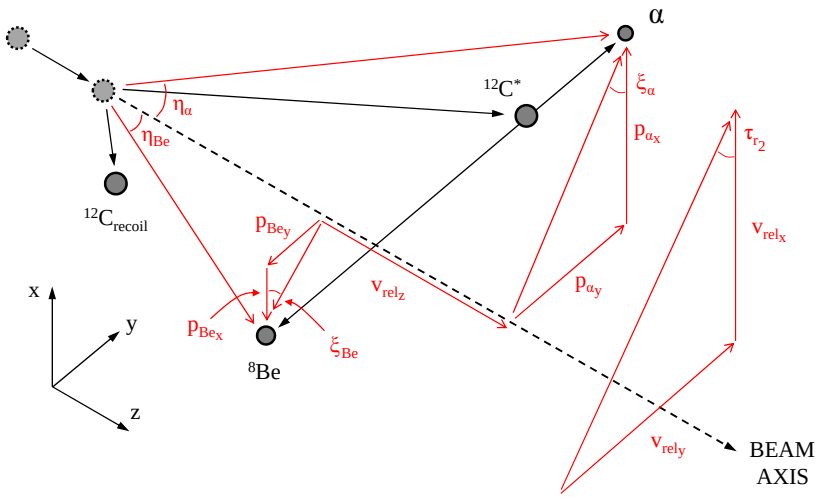

(b) Quantities required to calculate ψ after rotating into the $^{12}C^*$ breakup plane.

Figure 2.7: Details of the intermediate angles used to calculate θ^* and ψ after rotating into the $^{12}C^*$ breakup plane.

x- and y-momenta		Offset to $\xi_\alpha/\xi_{\mathrm{Be}}$ (°)
$\mathrm{p}_{\alpha_\mathrm{x}}$ / $\mathrm{p}_{\mathrm{Be}_\mathrm{x}}$	$\mathrm{p}_{\alpha_\mathrm{y}}/\mathrm{p}_{\mathrm{Be}_\mathrm{y}}$	
> 0	> 0	0
≤ 0	> 0	+ 90
≤ 0	≤ 0	+ 90
> 0	≤ 0	+ 180

Table 2.1: Offset parameters used in calculating angular correlations in the breakup plane.

The angle θ^* can then be calculated:

$$\theta^* = \tan^{-1}\left(\frac{\mathrm{p}_{\mathrm{C}_{\mathrm{xy}}}}{\mathrm{p}_{\mathrm{C}_{z_{cm}}}}\right)\cos\left(\tau_{\mathrm{r}_2} - \tau_{\mathrm{r}_1}\right) , \tag{2.29}$$

where τ_{r_1} is the scattering angle of the ^{12}C* in the x $-$ y plane and τ_{r_2} is the relative angle between α-particle and ^{8}Be (again in the x $-$ y plane); $\tau_{\mathrm{r}_2} - \tau_{\mathrm{r}_1}$ is the difference between these angles and the cosine of $\tau_{\mathrm{r}_2} - \tau_{\mathrm{r}_1}$ is its projection into the ^{12}C$^*-^{12}$C scattering plane. The angle ψ must also be rotated and scaled via a series of intermediary angles. The x- and y-angles associated with the momenta of the ^{8}Be and α-particle are combined using

$$\eta_\alpha = \cos^{-1}\left(\cos\left(\phi_y\right)\cos\left(\phi_x\right)\right) , \tag{2.30}$$

and

$$\eta_{\mathrm{Be}} = \cos^{-1}\left(\frac{\mathrm{p}_{\mathrm{Be}_\mathrm{z}}}{\mathrm{p}_{\mathrm{Be}}}\right) . \tag{2.31}$$

The angle ξ, the x $-$ y angle, is also used:

$$\xi_\alpha = \tan^{-1}\left(\frac{\mathrm{p}_{\alpha_\mathrm{y}}}{\mathrm{p}_{\alpha_\mathrm{x}}}\right) , \tag{2.32}$$

$$\xi_{\mathrm{Be}} = \tan^{-1}\left(\frac{\mathrm{p}_{\mathrm{Be}_\mathrm{y}}}{\mathrm{p}_{\mathrm{Be}_\mathrm{x}}}\right) , \tag{2.33}$$

which are corrected by a phase offset depending on the signs of $\mathrm{p}_{\alpha_\mathrm{x}}$, $\mathrm{p}_{\alpha_\mathrm{y}}$, $\mathrm{p}_{\mathrm{Be}_\mathrm{x}}$ and $\mathrm{p}_{\mathrm{Be}_\mathrm{y}}$. The offsets are shown in table 2.1. It is also necessary to correct by the relative angle between

the ^{8}Be and α-particle:

$$\xi'_{\alpha} = \xi_{\alpha} - \tau_{r_2} , \tag{2.34}$$

$$\xi'_{\mathrm{Be}} = \xi_{\mathrm{Be}} - \tau_{r_2} . \tag{2.35}$$

This allows ξ'_{α} and ξ'_{Be} to be used to calculate rotation angles for p_{α} and p_{Be}, and in turn these are used to calculate corrected values of v_{rel_x} and v_{rel_z}. The corrected momenta are

$$p_{\alpha_x} = p_{\alpha} \sin(\omega_{\alpha_x}) \cos(\omega_{\alpha_y}) , \tag{2.36}$$

$$p_{\alpha_y} = p_{\alpha} \sin(\omega_{\alpha_y}) , \tag{2.37}$$

where p_{α} is the total momentum of the α-particle, and ω_{α_x} and ω_{α_y} are

$$\omega_{\alpha_x} = \sin^{-1}(\sin(\xi'_{\alpha}) \sin(\eta_{\alpha})) , \tag{2.38}$$

$$\omega_{\alpha_y} = \tan^{-1}\left(\frac{\cos(\xi'_{\alpha}) \sin(\eta_{\alpha})}{\cos(\eta_{\alpha})}\right) ; \tag{2.39}$$

$p_{\mathrm{Be_x}}$ and $p_{\mathrm{Be_y}}$ (and $\omega_{\mathrm{Be_x}}$ and $\omega_{\mathrm{Be_y}}$) are calculated in the same way. Using these new values for the x- and z-momenta of the α-particle and ^{8}Be, the relative velocities can once again be calculated using equations 2.23 and 2.24, and in turn ψ using equation 2.25.

It is worth noting that, after completing the rotation into the breakup plane, the relative angle between the α-particle and ^{8}Be, ϕ, is 180°.

Chapter 3

Experimental Techniques

This chapter is divided into three main sections. The first of these describes the experimental details, such as information on the accelerator, detectors and triggering system. The second section is a short presentation of the calibration procedures for both energy and position calibrations. The final section gives a brief overview of some of the analysis tools used during the present analysis.

3.1 Experimental Details

The experiment was conducted using the 14UD tandem Van der Graaff Pelletron accelerator facility at the Australian National University (ANU), Canberra, in April 2005. A schematic of the facility is shown in figure 3.1. The experiment was run over 5 days of beamtime using a 50 μgcm^{-2} ^{12}C foil target. The beam energy was 101.5 MeV and the beam current was typically 10 enA; the charge state of the beam was 6^{+}.

3.1.1 The tandem Van der Graaff accelerator (and LINAC)

The ^{12}C beam was produced using the 14UD Pelletron accelerator at the ANU, the basic operation of which is as follows. A negative beam of carbon was produced at the sputtering ion source and accelerated to an energy of $\sim$150 keV, before being deflected by 90° and injected into a beamline at the top of the accelerator. From there it was attracted by potential created by the large positive voltage of the 14UD terminal, which causes the beam

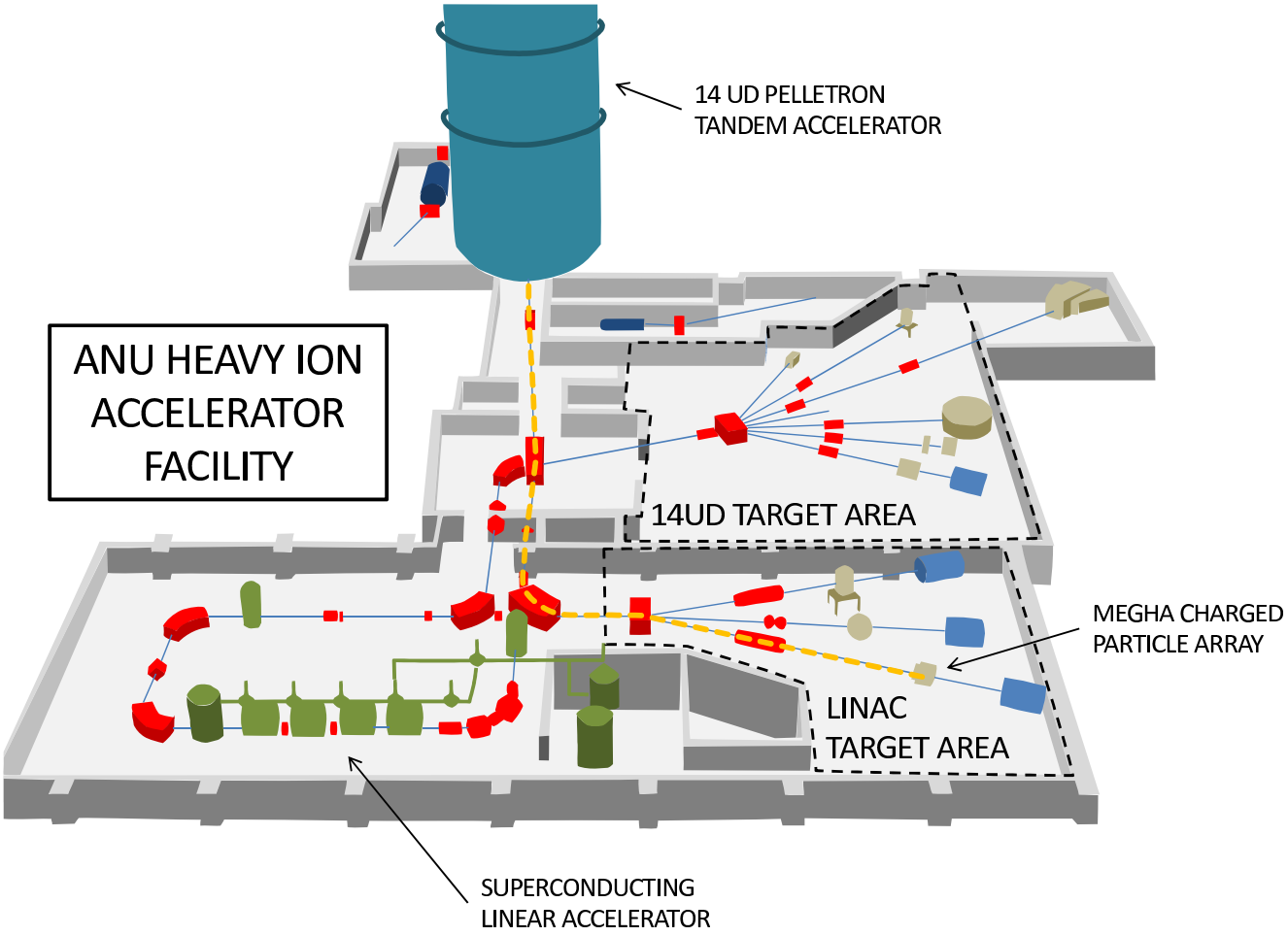

Figure 3.1: Schematic of the 14UD tandem Van der Graaff accelerator setup at ANU. The dashed line indicates the beam path for the current measurement. Adapted from [55].

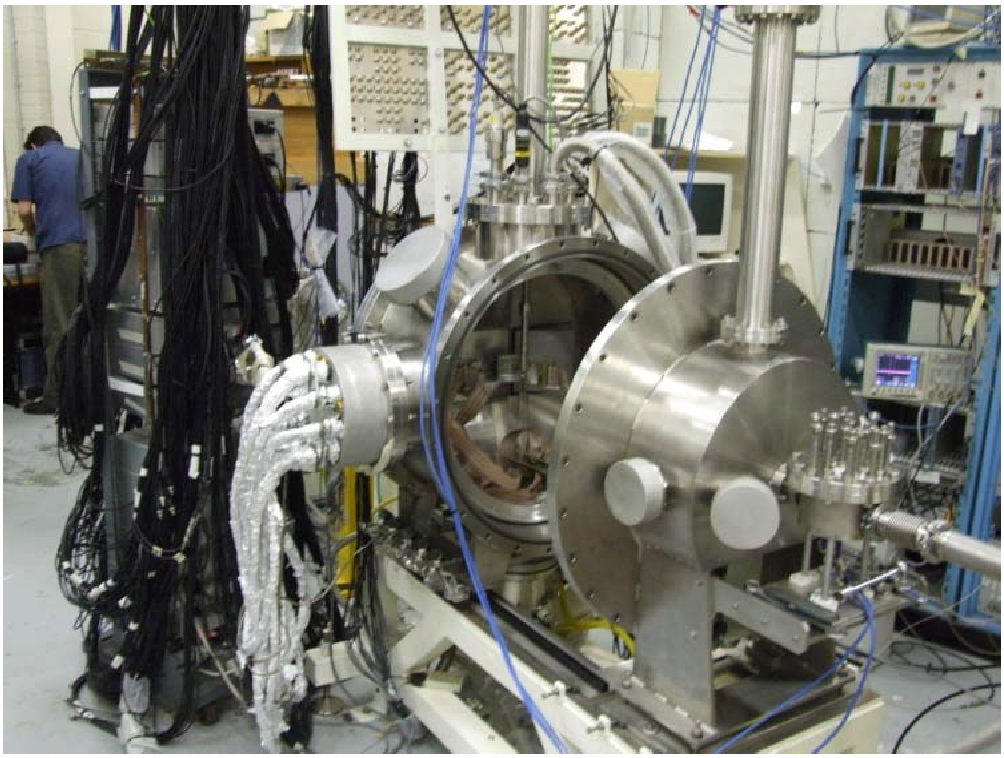

Figure 3.2: Photograph of the (open) MEGHA chamber. The beam enters the chamber from the bottom right of the picture.

to be accelerated. Upon reaching the terminal, it passed through a thin carbon foil which stripped electrons from the ions and hence reversed the beam's polarity. The beam was then repelled from the terminal and underwent a second stage of acceleration as it continued down the accelerator. At the bottom of the accelerator the beam was once again deflected through an angle of 90° before being steered, using a number of magnets and steering apparatus, into either the target chamber or into a super-conducting linear accelerator (LINAC).

The 14UD operates at up to 15.5 MV, which for ^{12}C using a (fully-stripped) 6^+ charge state defines a maximum beam energy of ∼108.5 MeV. Should a further boost in energy be required the ANU facility also includes a LINAC within the beamline. This is constructed of a series of nine split loop resonators, each allowing approximately a 2 MeV boost. Since the required beam energy of 101.5 MeV was within the capabilities of the 14UD accelerator then use of the LINAC was not necessary and the beam was steered directly into the MEGHA (Multi-Element Gas Hybrid Array) chamber (figure 3.2).

The pressure of the vacuum in the MEGHA chamber was typically $\sim 10^{-5}$ Torr and the

beam spot size of the system was $\sim\varnothing 2$ mm.

3.1.2 Detector setup

In the study of the ^{12}C(^{12}C,^{12}C[3α])^{12}C reaction three α-particles were detected in coincidence. This was done in an array of four detector telescopes (two primary and two secondary), arranged to provide an angular coverage in the range $\theta^* \approx 5^\circ - 30^\circ$ in the laboratory frame; this suitably covered the range of excitation energies being investigated and allowed for complete coverage of the azimuthal range. A schematic of the array is shown in figure 3.3. The primary detector telescopes consisted of three elements (from front to back):

- a (50 × 50) mm^2, 70 μm thick, double-sided strip detector (DSSD);
- a (50 × 50) mm^2, 500 μm thick, resistive strip detector (RS);
- a (50 × 50) mm^2, 10 mm thick, caesium-iodide (CsI) scintillator.

The DSSDs were divided into two sets of 16 independent 3 mm wide strips wide strips, the 16 strips on the front face having a horizontal orientation and the the 16 strips on the back face a vertical orientation. This results in a total of 256 (3 × 3) mm^2 'pixels' which can be used for determining positions of incident particles. The RS detectors were separated into 16 position-sensitive strips, which provided position information with a (FWHM) resolution of $\sim$0.3 mm in-plane (discussed further in section 3.1.4) and $\pm$1.5 mm out-of-plane. Due to the superior resolution, for the analysis contained within this thesis all position measurements were determined using the RS detectors. The energy resolution was $\sim$150 keV (FWHM) for the silicon detectors and $\sim$1.5% (FWHM) for the CsI scintillators[1]. The two secondary telescopes consisted of:

- a (50 × 50) mm^2, 70 μm thick, Si quad detector (Quad);
- a (50 × 50) mm^2, 500 μm thick, resistive strip detector (RS);

[1]The CsI detectors were not used at any stage to measure energy, but rather as a gate to separate events in which a particle has 'punched through' both of the Si detectors from those in which all the energy of all detected particles is fully deposited in the Si detectors.

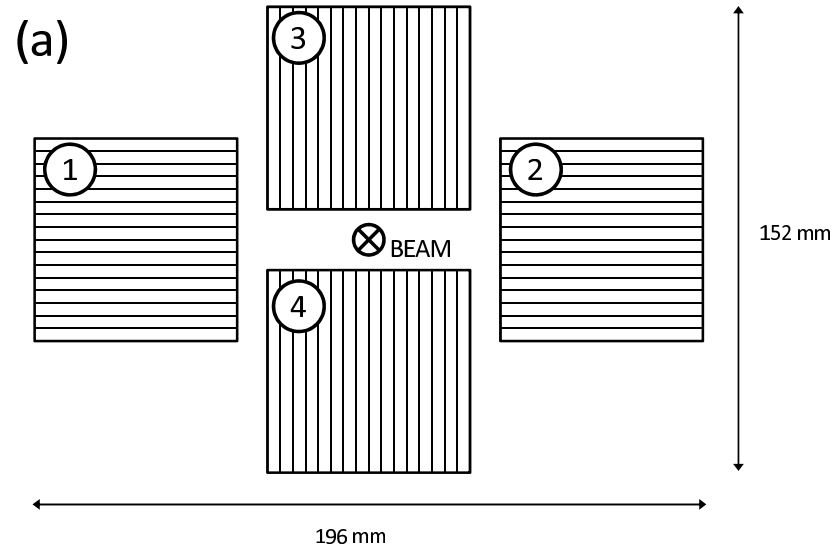

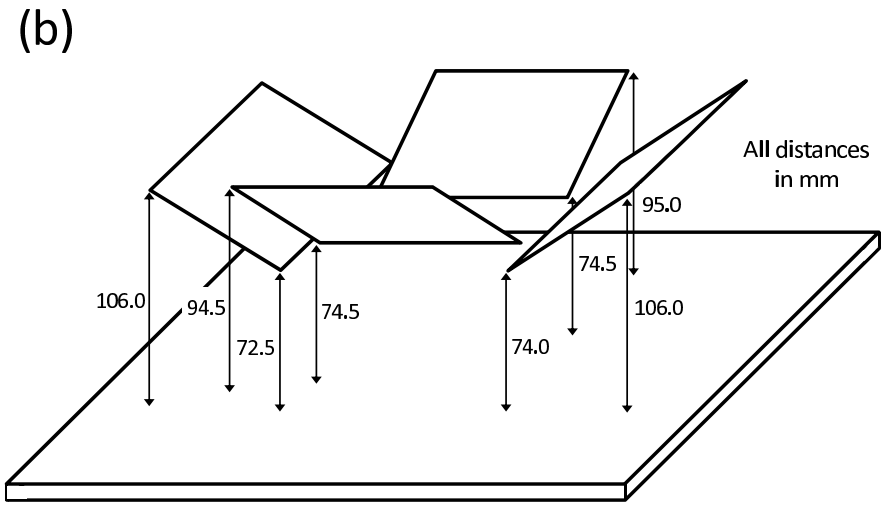

Figure 3.3: Schematic description of the detector setup. In (a), telescopes 3 and 4 are the primary telescopes and consist (from front to back) of a (50×50) mm^2, 70 μm thick, double-sided Si strip detector, a (50×50) mm^2, 500 μm thick, position sensitive Si resistive strip detector and a 10 mm thick CsI scintillator. Telescopes 1 and 2 consisted were identical to telescopes 3 and 4, except that a (50×50) mm^2, 70 μm thick, Si quad detector replaced the double sided strip detectors at the front of the telescopes. In (b), the distances shown are from the front of the array base plate to the front side of the detector faces when in place on the mounts.

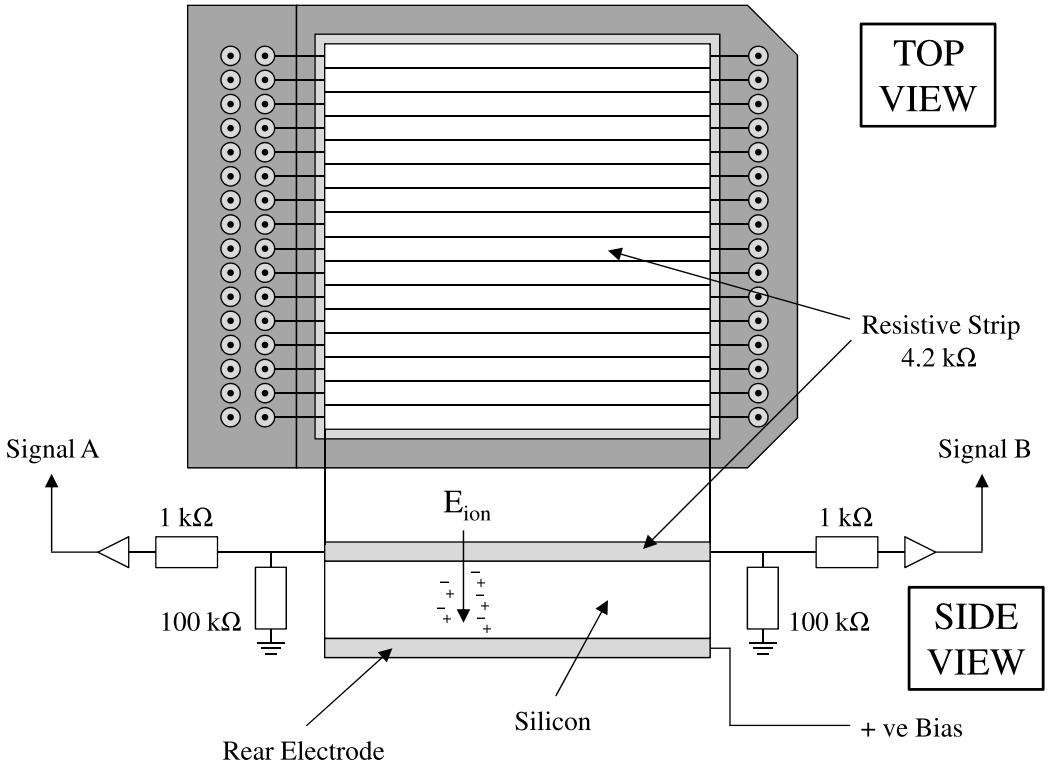

Figure 3.4: Schematic diagram of a resistive strip (RS) silicon detector. By collecting a signal at both ends of a strip an accurate measurement ($\Delta x \simeq \pm 0.3$ mm) of the position of a hit can be deduced, as well as its energy.

- a (50 × 50) mm^2, 10 mm thick, caesium-iodide (CsI) scintillator.

The Quad detectors were separated into four (25 × 25) mm^2 segments (quadrants).

The resistive strip (RS) silicon detectors

Figure 3.4 shows the schematic layout of an RS detector, the primary detector type of all four telescopes. The RS detector is a semiconductor detector constructed from a p-n junction. This is created by using ion-implantation to convert a thin layer of n-type silicon into p-type material, by using an accelerator to implant acceptor ions (boron), and then evaporating thin electrical contacts onto the front and rear of the detector. The RS detectors make use of a contact at each end of the front face of a strip, allowing an accurate measurement of the position of a hit to be determined (see section 3.1.4). The use of a (1 kΩ) termination resistor at each end ensures that, for events at or near the end of a strip, some charge will

be collected at both contacts.

By applying a reverse bias[2] (i.e. a positive voltage to the n side of the junction), the detector is enhanced in two important ways. Firstly, the depletion region is extended to almost the entire thickness of the detector, which increases the volume in which a charged particle can be detected. The second purpose of the reverse bias is to reduce the time taken for the holes/electrons to travel through the detector and be collected at the corresponding contact. With the reverse bias applied, the detector effectively behaves like a diode, allowing the free-flow of current in one direction, while presenting a large resistance in the other. If the reverse bias is made too large then a breakdown in the diode will occur, causing the reverse current to abruptly increase. This is often destructive in nature and so care must be taken to select a bias voltage which is as large as possible within the safe limits of the detector.

The double-sided silicon strip detectors (DSSD)

The DSSD detectors (used in two of the four telescopes) work in a manner almost identical to the RS detectors. Instead of the strips running in only a single direction however, the detectors are manufactured such that 16 strips run across both the front and rear of the detector, in perpendicular directions on each face. A charged particle incident on the detector will then trigger a single strip on each face, allowing its position to be determined by the strips' overlap. Care must be take in the case of multiple hits in a detector. If, for example, two particles are incident on a DSSD, this will result in four crossing points of front/back strips (as shown in figure 3.5). In order to select the correct position, the events on both faces are ordered in terms of energy. This allows the signals to be correctly matched and prevents incorrect positional measurements.

As the energy of a particle can be determined from the signal on either the front face or the back face of a detector then an average of the two signals was used; this should improve the resolution by a factor of $\sqrt{2}$.

[2]For the analysis contained within this thesis, a typical reverse bias voltage is ∼100 V.

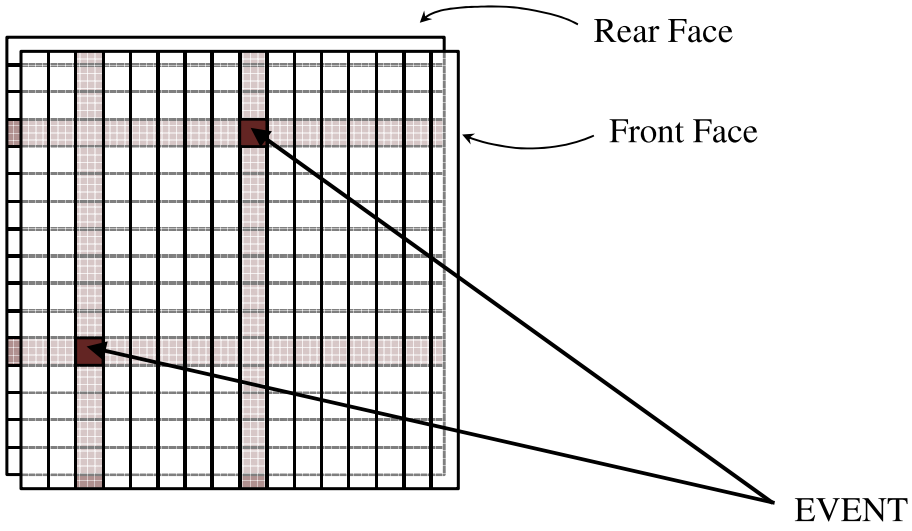

Figure 3.5: Schematic diagram showing how hit position is determined using a double-sided silicon strip detector (DSSD). Two particles are shown incident on a DSSD; the position of a hit is determined by the overlap of the triggered strips on the front and back face. In the case of more than one particle being deposited this results in the possibility of incorrectly pairing the front and back strips for each particle. This is overcome by ordering the hits on each face by the energy they deposit.

The silicon quad detectors (Quad)

The Quad detectors (used in two of the four telescopes) work in a similar manner to both the RS and DSSD detectors. Unlike the previous silicon detector types however, the faces of the Quads are divided into four smaller squares, each capable of generating a signal upon detecting a charged particle. Although this results in a poor positional resolution (relative to the RS detectors also present in a telescope), the primary disadvantage was the detectors' inability to resolve the energies of two particles incident on the same quadrant. The Quads were thus replaced in the analysis code at an early stage by an algorithm that used the energy detected in the RS detectors to calculate the energy loss of a particle as it travelled through the Quad detectors[3].

3.1.3 Electronics and the Data Acquisition System (DAQ)

Across the four telescopes the data acquisition (DAQ) system consisted of 204 channels: 32 for each of 4 RS and 2 DSSD detectors, 4 for each of the 2 Quad detectors, and 1 further channel for each of the CsI scintillators. The process of data acquisition can be separated into 4 phases:

- Preamplification
- Signal amplification and analogue processing
- Digital conversion and processing
- Data broadcast and storage

As discussed previously, the RS and DSSD detectors differ in the number of signals generated per strip, but each signal generated by all types of detector is handled in the same way by the DAQ. Signals generated by a hit on a strip are initially pre-amplified, and then passed to the main amplifiers. From the amplifiers two signals are generated, a fast output (which, depending on the detector, can be passed to the trigger system) and a slow output (which is broadcast for digital processing). A schematic description is shown in figure 3.6.

[3] At a later stage in the analysis, the DSSDs were also replaced with the same algorithm.

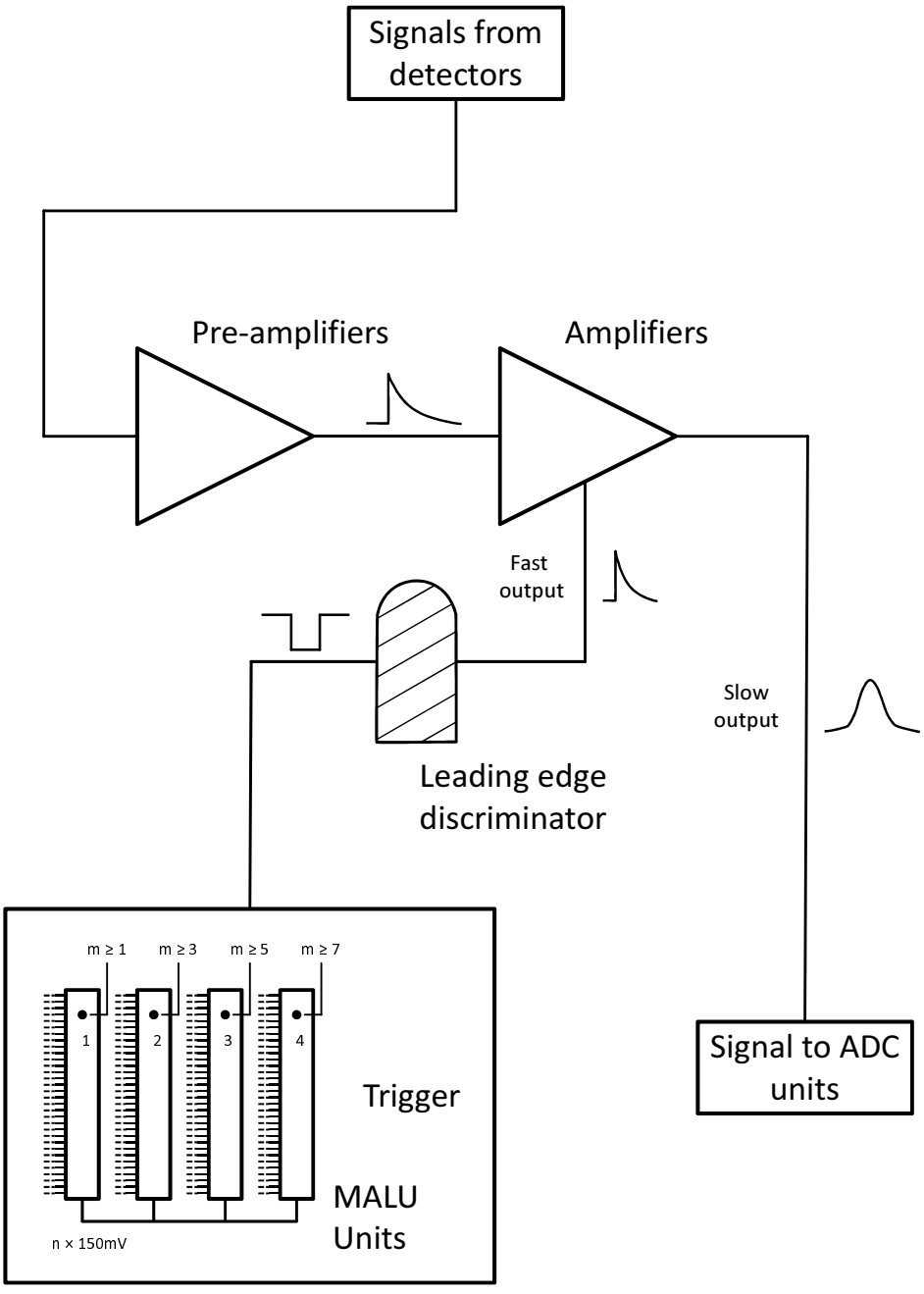

Figure 3.6: Schematic description of the electronics setup. The four majority amplified logic (MALU) units are daisy-chained together such that the signals generated are summed together. The individual triggers in each can then be separately used to trigger on events in which either 1, 2, 3 or 4 particles are detected.

The Event Trigger

The trigger system within the experimental setup described is based on the four RS detectors. For each strip-end "fired", a signal is passed to a leading-edge discriminator. The discriminator (one is used for each channel) is adjusted to trigger when a suitably large signal is received from the detector, allowing a balance between reducing noise and acquiring suitable statistics to be achieved. From the amplifier a 'fast' signal is sent to one of four Majority amplified logic units (MALUs), each having 32 inputs, one for each strip-end of an associated RS detector. For each input it receives, a MALU generates a standard 150 mV output (e.g. if three strip ends in an RS detector fire, its associated MALU will receive 3 inputs and generate a 450 mV pulse). By 'daisy-chaining' the four MALUs and summing the output of all four together the total number of strip-ends fired per event can be counted. Within each MALU is a discriminator and each can be independently set to require a total pulse of a different size for an event to be considered as an interesting event. If an event is considered to be interesting, the DAQ will instruct the 'slow' outputs from the amplifiers to be digitally processed. In the experimental setup described within this thesis, the four different triggers were set at levels to trigger for multiplicities of m $\geq$ 1, m $\geq$ 3, m $\geq$ 5 and m $\geq$ 7 (corresponding to single, double triple and quadruple hits respectively).

In addition to the described electronics, a pre-scaler was used to scale down the number of events recorded for certain multiplicities. For singles (n = 1) the number of *recorded* : *triggered* events was 1 : 100, for doubles and triples (n = 2 and n = 3) it was 1 : 20 [4], and for quadruples (n = 4) it was 1 : 1.

The digital processing involved broadcast of the data to a remote terminal, where it was written in 32 kB blocks to DLT tape for sorting and analysis. The data was recorded in 'run' files $\sim$2 GB in size; a single run typically contains $\sim$100,000 events of interest (triples) for the analysis contained herein. At a later stage this was processed into 16 kB blocks for compatibility reasons.

[4]For the current analysis it would be preferable for a scale-down factor of 1 : 1 for n = 3 but, as the primary channel of interest when the experiment was performed was n = 4, a scale down factor of 1 : 20 was implemented for triples.

3.1.4 Determining hit position on a detector

As discussed previously, all positional information of a hit was calculated using the RS-detectors contained within the telescopes; this involved two different approaches for the x- and y-coordinates of a hit depending on whether the coordinate is parallel or perpendicular to the strip direction. The hit position perpendicular to the strip direction was determined simply by which strip was triggered, and has a resolution of ± 1.5 mm (the strip width). The hit position parallel to the strip direction can be calculated using resistive charge division methods: if both ends of a strip are triggered two energy-signals are recorded, E_1 and E_2, and the position of the hit (away from the halfway point), pos$'$, is given by

$$\mathrm{pos}' = \frac{E_1 - E_2}{E_1 + E_2} \quad . \tag{3.1}$$

However, due to the presence of the offset resistors in the RS-detectors, pos$'$ must be corrected to give the actual position of a hit, pos:

$$\mathrm{pos} = \frac{\mathrm{pos}' - \mathrm{pos}_1}{\mathrm{pos}_2 - \mathrm{pos1}} \times \textit{strip length} \quad , \tag{3.2}$$

where the *strip length* is 50 mm, and pos_1 and pos_2 are the ends of the initial position spectra; the resolution is $\sim$0.3 mm. The method is discussed further in [56].

3.1.5 Converting to an angular hit position and momentum

Upon determining the position at which a particle hits a detector telescope, it is necessary to convert this into a hit position on the complete detector array. This was done by converting the x- and y-coordinates of a hit on a detector to angular measurements relative to the beam axis, ϕ_x and ϕ_y (the beam axis being along the z-axis).

By converting the energy of a hit into momentum:

$$\mathrm{p_{tot}} = \sqrt{2\mathrm{mE}} \, , \tag{3.3}$$

(where m is the mass of the detected particle) the two angular measurements can be used to calculate the separate x-, y- and z-components:

$$p_x = p_{tot} \sin\phi_x \cos\phi_y \ , \tag{3.4}$$

$$p_y = p_{tot} \sin\phi_y \ , \tag{3.5}$$

$$p_z = p_{tot} \cos\phi_x \cos\phi_y \ . \tag{3.6}$$

The x-direction is taken as to be along the RS strips of telescopes 3 and 4, and the y-direction is along the RS strips in 1 and 2. A more complete discussion of the calculations involved to obtain ϕ_x and ϕ_y is given in appendix B.

3.2 Calibrations

3.2.1 Energy calibrations

Measurement of a sequential break-up reaction, such as that discussed within this thesis, requires extensive calibrations both during and after the experiment. Variations in the detector response, detector linearity and gain all have to be accounted for in terms of the calibrations of detector position and energy. The calibration was conducted in three phases:

- checking the apparatus was operational;
- preamplifier gain and offset calibrations - online calibration;
- offline calibration.

Offline calibration of the detectors and amplifiers was performed using a combination of three techniques: a 3-line α-source (^{239}Pu, ^{239}Am and ^{239}Cm), linear regression performed on a series of 'matchsticks' pulses generated by a pulser unit, and 45 MeV ^{12}C ions elastically scattered from a ^{197}Au target[5].

[5]An more extensive discussion of the 'flash gold' and 'matchsticks' calibration techniques can be found in [56].

Alpha calibrations

A triple-peak α-particle source was used to generate three peaks in each detector of known energies and spacings[6] (figure 3.7 shows some examples of α-calibration data). These were used to check amplifier gains and offsets before the experiment was run. The α-peak calibrations were used to convert energy from channels to MeV.

Matchsticks calibrations

The 'matchsticks' calibrations were carried out at a number of times throughout the experiment and were used to check the linearity and variation in the gains of the amplifiers. The calibrations involve triggering the system with a precision pulser unit, which sends a series of increasing incremented voltages in the form of pulses, starting at zero amplitude. A record of the matchsticks was taken for each preamplifier and a check for regular spacing of the resulting peaks performed. Examples of matchsticks calibrations are shown in figure 3.8.

Flash gold calibrations

The flash gold calibrations involve the elastic scattering of ^{12}C nuclei[7] from a much heavier target (^{197}Au), and offer a second method of calibrating a gain correction to the energy of detected particles. They were used in addition to the gain corrections obtained from the α-calibrations discussed earlier, as well as for positional calibrations. It is necessary to apply the offsets from the α-calibrations prior to calculating correctional terms using the technique discussed below.

Two separate events of known energy are incident on the extreme ends of a strip (shown in figure 3.9). The charges liberated by each ion are amplified and then recorded as particular ADC values. As each hit causes a different charge pulse at each strip-end then, since the signals from the two sources are summed, the following equations are obtained:

$$ch_1 = Q_H g_1 + Q_L g_2 \tag{3.7}$$

[6]The source contained three α-emitters: ^{239}Pu (5.157 MeV), ^{241}Am (5.486 MeV) and ^{244}Cm (5.805 MeV).
[7]The calibrations carried out for the experiment discussed in this thesis used 25.5 MeV ^{12}C nuclei.

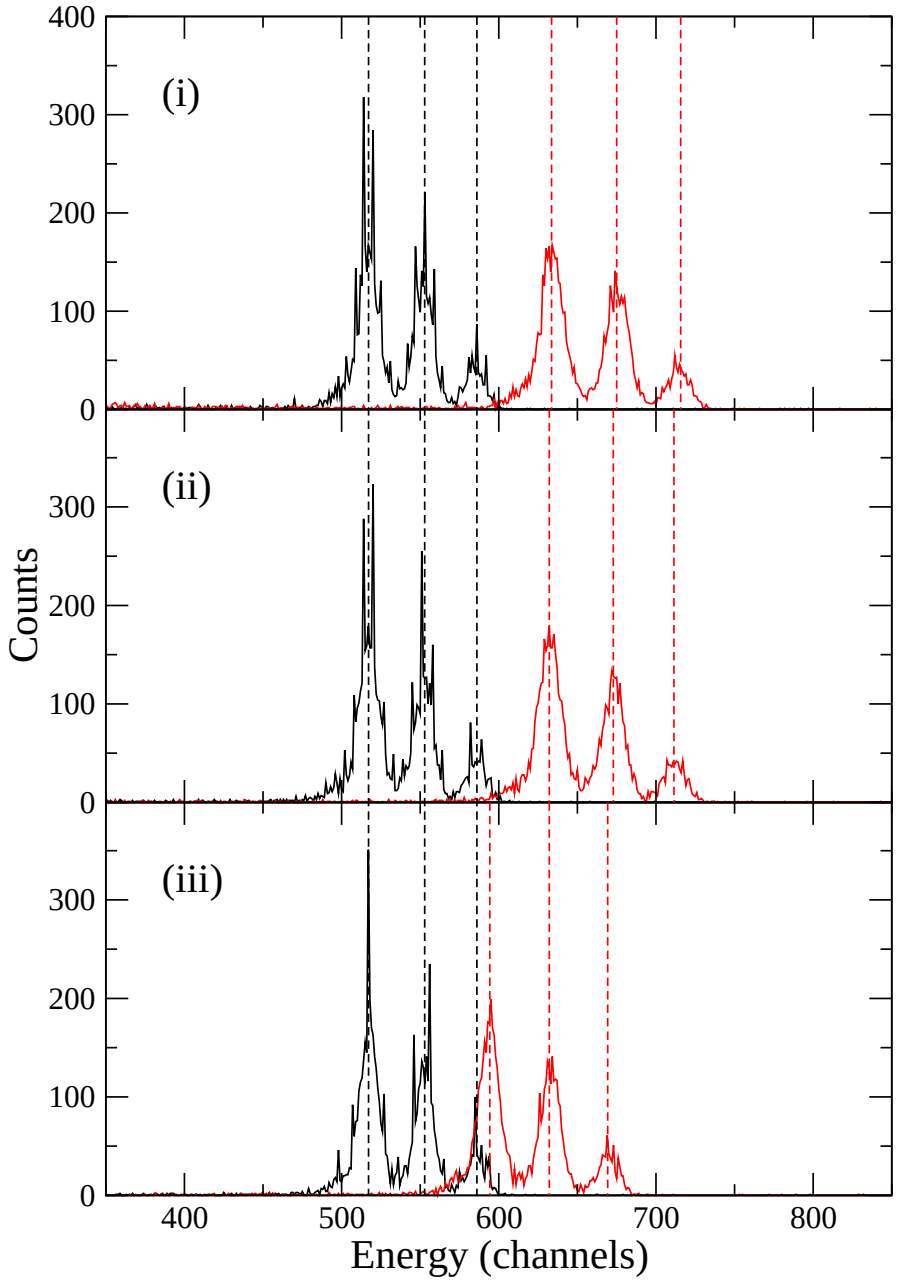

Figure 3.7: Three peak α-particle calibration data for three randomly selected detector strips. The red and black data sets are pre- and post-calibration respectively.

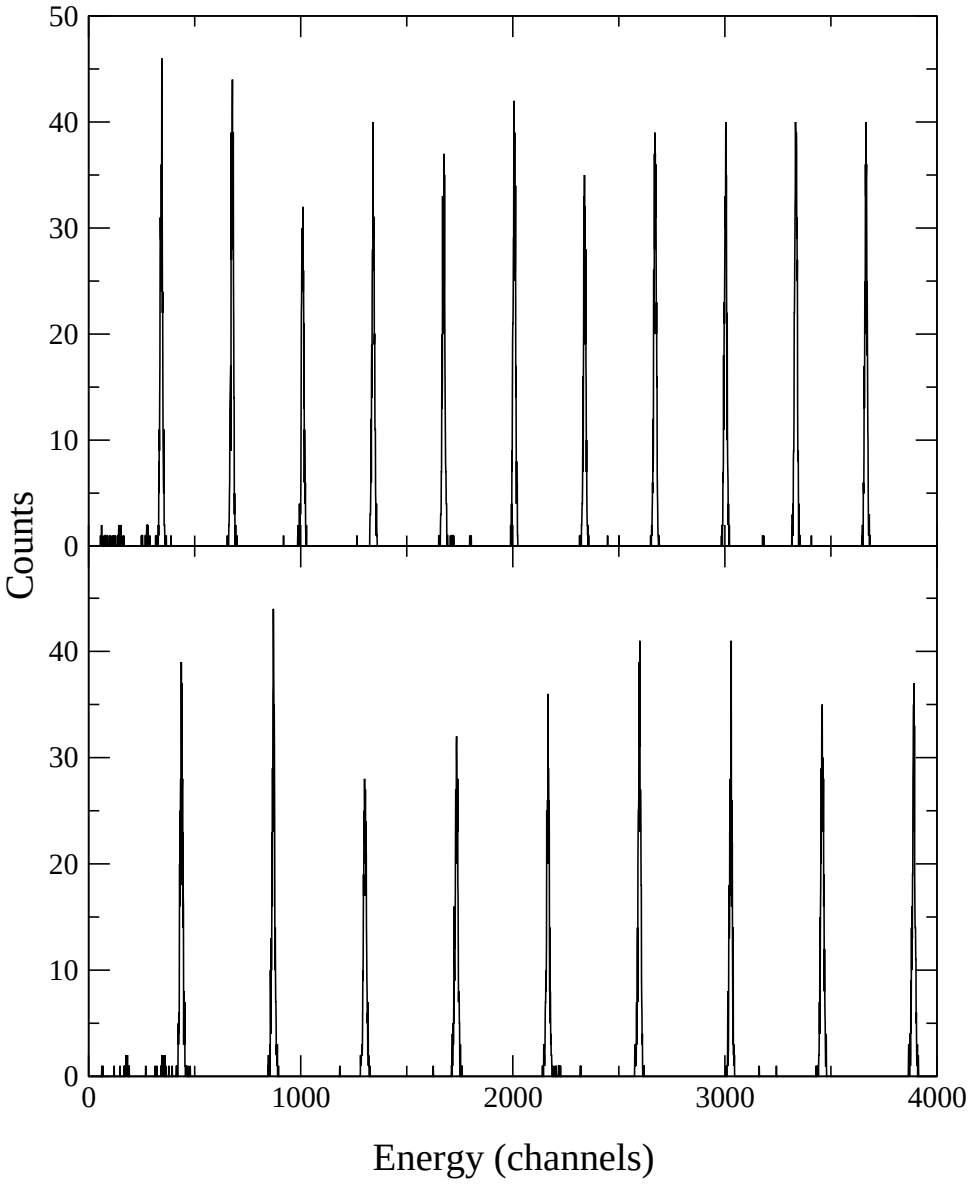

Figure 3.8: Matchsticks calibration data used to check linearity of the electronics for two randomly selected channels.

$$ch_2 = Q^{'}_H g_1 + Q^{'}_L g_2 \tag{3.8}$$

where $Q_H, Q_L, Q^{'}_H$, and $Q^{'}_L$ are the charges liberated from the each strip-end, g_1 and g_2 are the electronic gains which convert from charge into channel number and ch_1 and ch_2 are the channel numbers recorded for the particular event. The energy of the events is related to the charge liberated by:

$$E_1 = (Q_H + Q_L)Nw \tag{3.9}$$

$$E_2 = (Q^{'}_H + Q^{'}_L)Nw \tag{3.10}$$

where N is the number of electron-hole pairs produced by the incident ion and w is the average energy required to produce one electron-hole pair.

The ratios Q_H/Q_L and $Q^{'}_H/Q^{'}_L$ can also be obtained by considering that

$$Q_H = Q\left(\frac{R_s + R}{R_s + 2R}\right) \tag{3.11}$$

$$Q_L = Q\left(\frac{R}{R_s + 2R}\right) \tag{3.12}$$

$$Q^{'}_H = Q^{'}\left(\frac{R}{R_s + 2R}\right) \tag{3.13}$$

$$Q^{'}_L = Q^{'}\left(\frac{R_s + R}{R_s + 2R}\right) \tag{3.14}$$

which gives

$$\frac{Q_H}{Q_L} = \frac{R_s + R}{R} \tag{3.15}$$

$$\frac{Q^{'}_H}{Q^{'}_L} = \frac{R}{R_s + R} \tag{3.16}$$

where R_s is the resistance of a strip (4.2kΩ) and R is the resistance of the termination resistor (1kΩ).

Rearranging 3.7 and 3.8 gives

$$\frac{ch_1}{Q_L} = \left(\frac{Q_H}{Q_L}\right) g_1 + g_2 \tag{3.17}$$

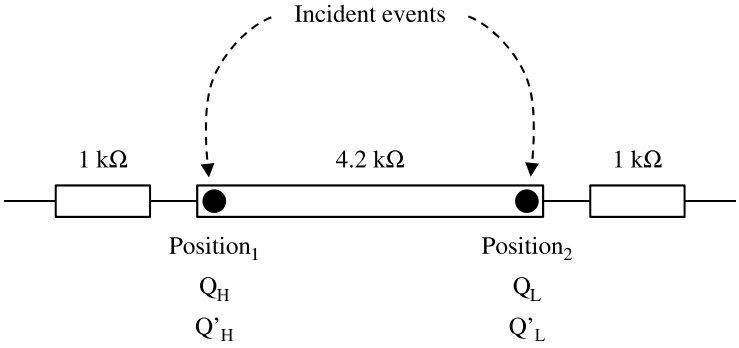

(a) Events incident at each strip-end and the charges.

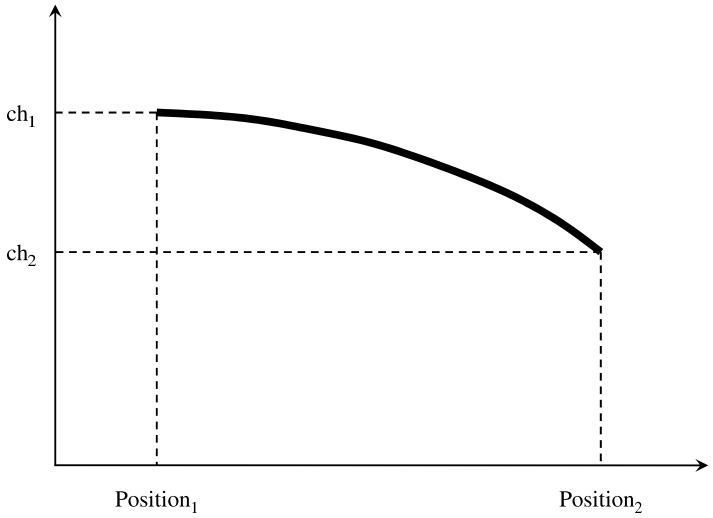

(b) Where the events lie on a plot of energy against position prior to the gains being applied to correct the energy offset.

Figure 3.9: A schematic of the parameters necessary for the calibration of the resistive strip detectors. Over the angular coverage of the detector, when calibrated the data will appear (approximately) as a horizontal bar in (b).

$$\frac{ch_2}{Q_L^{'}} = \left(\frac{Q_H^{'}}{Q_L^{'}}\right) g_1 + g_2 \tag{3.18}$$

and substituting 3.15 and 3.16 into 3.17 and 3.18 produces

$$\frac{ch_1}{Q_L} = \left(\frac{R_s + R}{R}\right) g_1 + g_2 \tag{3.19}$$

$$\frac{ch_2}{Q_L^{'}} = \left(\frac{R}{R_s + R}\right) g_1 + g_2 \tag{3.20}$$

From 3.9 to 3.16 it can then be shown that

$$Q_L = \left(\frac{R}{R_s + R}\right) Q_H = \left(\frac{R}{R_s + R}\right) \left(\frac{E_1}{Nw} - Q_L\right)$$

$$Q_L = \frac{RE_1}{Nw(R_s + R)} - \frac{Q_L R}{R_s + R} = \frac{RE_1}{Nw(R_s + R)} - \frac{R^2 E_1}{Nw(R_s + R)(R_s + 2R)}$$

therefore

$$Q_L = \frac{RE_1}{Nw(R_s + 2R)} \tag{3.21}$$

and similarly

$$Q_L^{'} = \frac{(R_s + R)E_2}{Nw(R_s + 2R)} \tag{3.22}$$

Subtracting 3.18 from 3.17 gives

$$\frac{ch_1}{Q_L} - \frac{ch_2}{Q_L^{'}} = \frac{Q_H g_1}{Q_L} - \frac{Q_H^{'} g_1}{Q_L^{'}} \tag{3.23}$$

and substituting from 3.12, 3.14, 3.15 and 3.16 gives

$$\frac{ch_1 Nw(R_s + 2R)}{RE_1} - \frac{ch_2 Nw(R_s + 2R)}{(R_s + R)E_2} = \frac{Q_H g_1 (R_s + R)}{RQ_H} - \frac{Q_H^{'} g_1 R}{Q_H^{'}(R_s + R)}$$

which simplifies to

$$\frac{ch_1 Nw}{RE_1} - \frac{ch_2 Nw}{(R_s + R)E_2} = \frac{g_1 R_s}{R(R_s + R)}$$

Rearranging for g_1 gives

$$g_1 = \frac{Nw}{R_s}\left(\frac{ch_1(R_s+R)}{E_1} - \frac{ch_2R}{E_2}\right) \tag{3.24}$$

and following a similar procedure

$$g_2 = \frac{Nw}{R_s}\left(\frac{ch_2(R_s+R)}{E_2} - \frac{ch_1R}{E_1}\right) \tag{3.25}$$

Referring back to 3.7 and 3.8 it is apparent that g_1 and g_2 convert to channel number; to convert from channel number it is necessary to divide by g_1 or g_2.

Examples of a typical strip both before and after calibration are shown in figure 3.10.

3.2.2 Position calibration

Positional calibrations of both the RS and DSSD detectors were performed using the flash gold data. Using the charge division method described in section 3.1.4, it is possible to determine how far along the strip a hit occurs. All strips were then normalized to be the same length and adjusted so as they were correctly lined up (i.e. the zero point distance of all strips were aligned). As all strips are 50 mm long (see figure 3.10), the relative position of a hit along a strip was then converted into a distance along the strip, and in turn to an angle relative to the entire detector array.

3.3 Analysis tools

3.3.1 SunSort

Having passed through the data acquisition system, data was packed into 32 kB blocks and written to tape. SunSort is the main analysing tool used by the Charissa collaboration and is used for both online and offline analysis. It is based around a user defined sort code, which for the analysis contained within this thesis was written in the Fortran77 language (though SunSort allows a choice between Fortran77 and C++). SunSort reads information about each event such as number of detector hits (determined by the discriminators), which strips

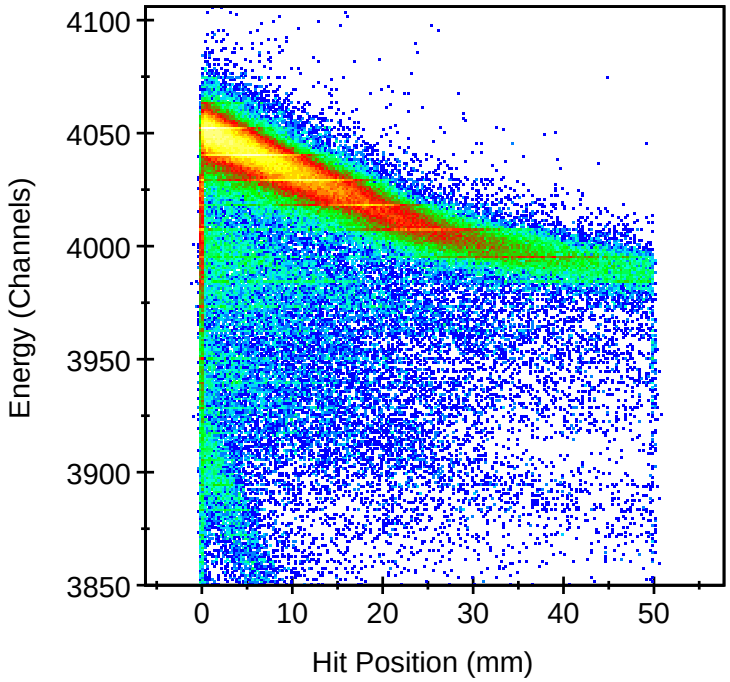

(a) Energy against position (pre-calibration).

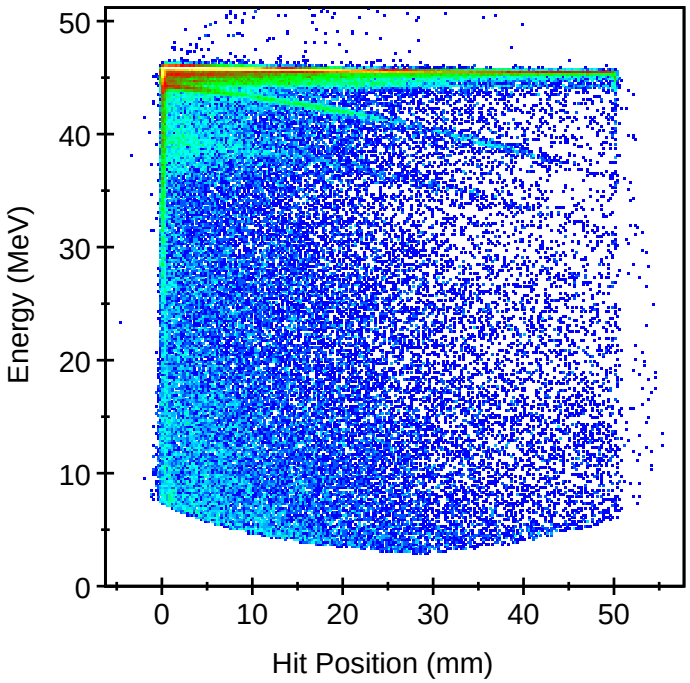

(b) Energy against position (post-calibration).

Figure 3.10: Energy versus position plots for a typical strip, both before and after energy gain calibration, shown for elastic scattering of (∼45 MeV) ^{12}C nuclei from a ^{197}Au target. Note that the length of the strip has already been calibrated in both (a) and (b) (see section 3.2.2).

have been triggered, particle energy, etc., and as such allows the events to be sorted. The user defined sort code then allows particle identification, reconstruction, etc., to take place for analysis. SunSort has been further documented in [57, 58].

3.3.2 Data Event Manipulation

SunSort allows the user to manipulate the experimental parameters on an event-by-event basis. For the analysis carried out within this thesis, four final-state particles were required, the recoil ^{12}C nucleus and 3α-particles. However, though four final-state particles were required for analysis, only three were required to be detected, as the fourth was reconstructed from momentum considerations. Monte Carlo simulations performed using the Resolution8 code (see section 3.3.3) suggest an increase in statistics of $\sim$70% if events in which three final-state particles are detected and thus the analysis performed within this thesis is based upon events in which only the 3α-particles are detected.

3.3.3 Monte Carlo Simulations - Resolution8

To aid with predictions of behaviour of the detection system a number of Monte Carlo simulations were performed. These were done using the Resolution8 (Res8) code developed by the Charissa collaboration. The code allowed the reaction to be simulated and the position/orientation of the detectors to be varied, as well as a number of further variables (e.g. detector efficiencies, detection energy thresholds, beam divergence etc.). The simulations were performed in a way such that they can be loaded into and analysed using the SunSort data analysis code in a similar way to the experimental data.

Details of simulations carried out to aid the analysis process are discussed, along with their relevance to the the experimental results, in chapter 4.

Modifications to Resolution8

During the analysis, two changes were made to to the Res8 code in order to better match the Monte Carlo simulations to the experimental data. These modifications are both briefly discussed here.

Including a Lorentzian line-shape

The Res8 code includes no intrinsic information about the line-shape of a simulated state, but allows detector resolution, beam straggling etc. to determine experimental widths and shapes. As a major part of the analysis process involved looking for minor variations in state line-shapes it was important to model the shape of the experimental results as accurately as possible. To better model a realistic line-shape, the Monte Carlo simulations were constrained to follow a Lorentzian distribution:

$$f\left(E_x\right) = \frac{\frac{1}{4}\Gamma^2}{\left(E_x - E_0\right)^2 + \frac{1}{4}\Gamma^2} \,, \tag{3.26}$$

where Γ is the width of the state being simulated and E_0 is the centroid of the state being simulated; both are constant for a given simulation but are varied over the different simulations performed (discussed further in chapter 4).

Including spin information

One of the main purposes of the Monte Carlo simulations involved simulating the angular correlation measurements described in chapter 2.3. In order to do this it was necessary to modify the Res8 code to include spin information.

As discussed in section 2.3, θ^*, ψ, J and l_i are linked by

$$\frac{\mathrm{d}\theta^*}{\mathrm{d}\psi} = \frac{J}{l_i - J} \,,$$

which dictates that the θ^* dependence of the ridges generated by the angular correlations will follow

$$\mathrm{P}_J = \mathrm{P}_J \left[\cos\left(\psi + \frac{J - l_i}{J}\theta^*\right)\right]^2 \,. \tag{3.27}$$

The spin of a state can be suitably simulated for angular correlations by generating the relevant Legendre polynomial and then constraining the simulations to follow this structure in the $\theta^* - \psi$ plane. For a $J^\pi = 3^-$ state, for example, this would involve constraining the

simulations to follow the dependence

$$\mathrm{P}_3\left(\theta^*,\psi\right)=\frac{1}{2}\left[5\cos^3\left(\psi+\frac{3-l_i}{3}\theta^*\right)-3\cos\left(\psi+\frac{3-l_i}{3}\theta^*\right)\right] \tag{3.28}$$

in the $\theta^*-\psi$ plane. While θ^* and ψ vary for each event, the grazing-angular-momentum, l_i is determined by the experimental parameters (beam and target species, beam energy etc.) and must be calculated from these. For the experiment described within this thesis

$$\begin{aligned} l_i &= \mathrm{r}\times\mathrm{p} \\ &= \mathrm{r}\sqrt{2\mu\mathrm{E}_{\mathrm{beam}_{\mathrm{CM}}}} \qquad (3.29) \\ &= \mathrm{r}_0\left(\mathrm{A_b}^{1/3}+\mathrm{A_t}^{1/3}\right)\sqrt{2\frac{\mathrm{A_bA_t}}{\mathrm{A_b}+\mathrm{A_t}}\mathrm{E_{beam}}\frac{\mathrm{A_t}}{\mathrm{A_b}+\mathrm{A_t}}} \\ &= \mathrm{r}_0\left(\mathrm{A_b}^{1/3}+\mathrm{A_t}^{1/3}\right)\frac{\mathrm{A_t}}{\mathrm{A_b}+\mathrm{A_t}}\sqrt{2\mathrm{A_bE_{beam}}}\,, \qquad (3.30) \end{aligned}$$

where in equation 3.29, μ is the reduced mass and $\mathrm{E}_{\mathrm{beam}_{\mathrm{CM}}}$ is the centre-of-mass energy. In equation 3.30, $\mathrm{A_b}$ and $\mathrm{A_t}$ are the beam and target atomic numbers respectively (both 12), and $\mathrm{E_{beam}}$ is the beam energy (101.5 MeV). Using a value of 1.3 fm for r_0, $l_i \simeq 22.5\hbar$.

There exists an exception when simulating a $J=0$ state as the ridges lie only in the θ^*-direction, and will follow a Legendre polynomial of order l_i. For the analysis contained herein, a 22^{nd}-order Legendre polynomial was used in simulating the θ^* dependence of the angular distribution of a $J=0$ state, whilst the ψ dependence was assumed to be isotropic.

Chapter 4

Results and Analysis

In this chapter, results are presented for the ^{12}C(^{12}C,^{12}C[3α])^{12}C experiment described previously. The analysis discusses methods used to identify and reconstruct the reaction particles, as well as techniques used to suppress background data. Results of Monte Carlo simulations performed to support the understanding of the experimental data are also presented. Finally, limits regarding the possible strength of a $J^{\pi} = 2^{+}$ resonance in the 9.7 MeV region are presented, along with details of the associated calculations.

4.1 Preliminary analysis

4.1.1 Particle identification and reconstruction

As discussed previously, the analysis contained within this thesis consists of events in which three final-state particles are detected, and more specifically those in which 3α-particles were detected. The initial stage in the analysis therefore involves filtering out events in which three particles were detected and in turn events in which all of these were α-particles. In order to achieve this for each detector telescope, the energy loss in the thin DSSD/Quad detector was plotted against the energy deposited in the thicker RS detector. This two-dimensional plot is known as a ΔE $-$ E, or PI (particle identification), plot. An example is shown in figure 4.1a.

The different types of detected particles separate into different loci which are dependent

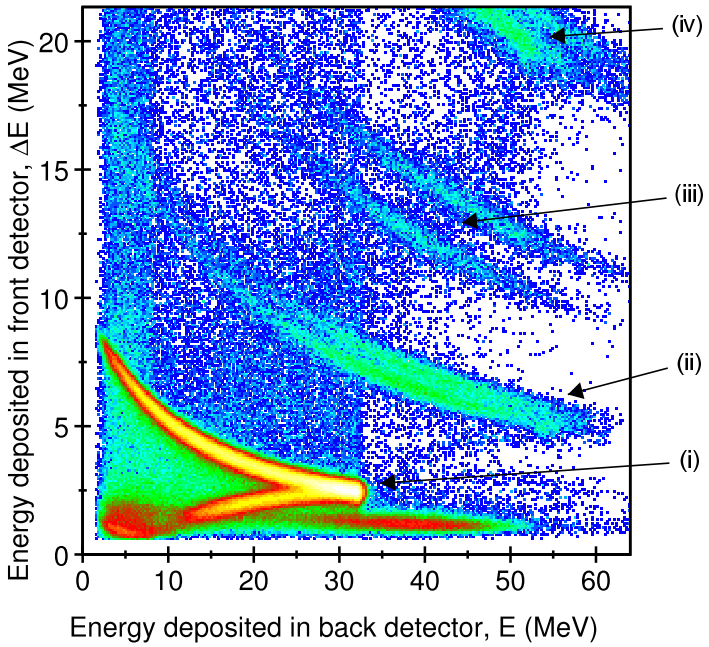

(a) $\Delta E - E$ at an early stage of the analysis code.

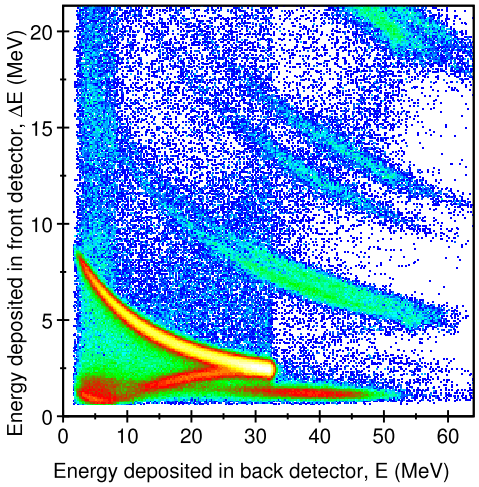

(b) $\Delta E - E$ with α-particles detected in the CsI removed.

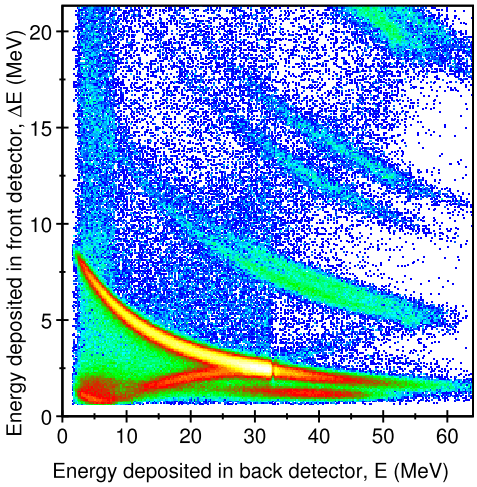

(c) $\Delta E - E$ with α-particle energies corrected for those that are detected in the CsI.

Figure 4.1: Typical $\Delta E - E$ plots for particle identification (a) at an early stage in the analysis code, (b) with punch-through events detected in the CsI removed, and (c) with the energies of 'punch-through' α-particles corrected; different loci correspond to particles of different mass. The loci labelled (i)-(iv) in (a) are associated with (i) α-particles, and isotopes of (ii) lithium, (iii) beryllium, and (iv) boron nuclei. Note that while not all of the punch-through events are corrected/removed in (b) and (c), those which are not are later removed using a software gate placed on the $\Delta E - E$ spectra. The energy required for an α-particle to punch-through a 500 μm silicon detector is $\sim$32.1 MeV.

on their mass and charge. The loci can be understood by Bethe's equation which describes the rate of energy loss as a charged particle travels through an ionisable medium [59, 60]. In the case of non-relativistic charged particles it can be approximated to

$$\frac{\mathrm{dE}}{\mathrm{dx}} \propto \frac{\mathrm{mZ}^2}{\mathrm{E}} \ , \tag{4.1}$$

where dE/dx is the energy loss per unit distance, and m, Z, and E are the mass, charge and energy of the detected particle respectively. For a given thickness of absorber

$$\mathrm{dE} \propto \frac{\mathrm{mZ}^2}{\mathrm{E}} \ , \tag{4.2}$$

and for a given energy

$$\mathrm{dE} \propto \mathrm{mZ}^2 \ . \tag{4.3}$$

Thus each individual locus corresponds to ions with both a common mass and a common charge. This allowed events in which only 3α-particles were detected to be separated by placing a software window around the locus corresponding to α-particles.

4.1.2 Reconstructing energy loss in secondary detectors

Due to the nature of the reaction channel investigated it is known that more than one α-particle will be incident on a given detector-telescope for each event (discussed in section 4.2). For a telescope in which this is the case, it is important to be able to resolve the separate particles. Though this is not normally problematic, for two types of event additional calculations must be performed before proceeding with the analysis.

'Punch-through' events

For a particle to be identified it is required that a particle passes through the telescope at least as far as the RS-detector in the middle of the telescope. If all detected particles are stopped by the RS-detectors then all the kinetic energy is measured and the event can be processed, but if one or more particles pass through to the CsI scintillator then, due to the

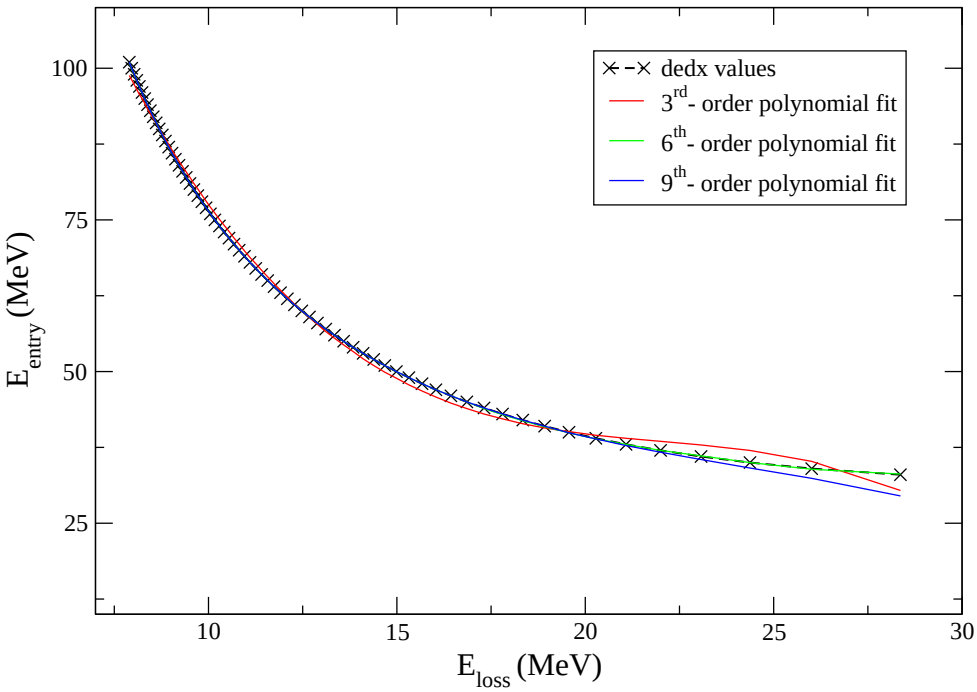

Figure 4.2: Energy losses for an α-particle traveling through a 500 μm silicon detector. By considering the energy deposited in an RS detector by a α-particle that punches through into the CsI crystal, it is possible to calculate the energy of the α-particle as it entered the RS detector. Polynomial regression fits of orders 2-10 were performed (three examples are shown); a sixth-order fit was used for the algorithm in the analysis code.

CsI scintillator not being energy calibrated, the energy deposited in the CsI crystal must be calculated and added back. Using the method described in section 4.1.1 then by considering the energy loss of a particle within a particular ionisable medium (*of a known thickness*), it is possible to calculate the energy that the particle possessed upon entering the medium. The 'dedx' code (previously written within the Charissa collaboration) was used to calculate the missing energy for a range of possible 'entrance energies'. A polynomial regression was used to create a short algorithm for which the detected RS energy can then be used to correct for the missing energy deposited in the CsI detector (shown in figure 4.2).

For events in which two particles are detected within an RS-detector and for which the CsI is also triggered it is often difficult to ascertain whether one or both particles have punched-through the silicon into the CsI. For this reason the technique was only used when a single particle was detected in a telescope and punches through. In the case that two

particles are detected in a telescope, *and* a signal was registered in the CsI detector in the same telescope, the event was discarded.

A $\Delta E - E$ plot after punch-through α-particles detected in the CsI have been removed is shown in figure 4.1b; figure 4.1c shows the same plot but includes the α-particles detected in the CsI with their energy corrected. Although the method does not remedy all punch-through events, any remaining (uncorrected) events are removed by the software gate placed over the α-particle locus.

Dual Quad hit events

For events in which two particles are detected within an RS-detector, but only one in a Quad detector, it is likely that both particles hit the same quadrant of the front detector. In order to use these events it is necessary to reconstruct the energy which each particle deposited in the front detector. This can be done using a method analogous to that used to calculate the energy deposited in a CsI above, though this time by considering the energy of a particle as it leaves an ionisable medium (of a known thickness) and calculating its energy upon entering the medium. Similarly to the energy deposited in the CsI crystals, the dedx code was used to calculate the energy loss of an α-particle through a silicon detector, and a polynomial regression fit applied to create a function to correct the energy of a particle detected in the RS detectors.

4.1.3 The E_{tot} spectrum

Following the reconstruction of the (undetected) ^{12}C recoil nucleus (section 2.2.2), the total energy of all the particles from an event, E_{tot}, can be calculated. An E_{tot} spectrum is shown in figure 4.3 and shows a series of peaks, each corresponding to a particular reaction channel. The highest energy peak occurs at ~ -7.5 MeV lower than the beam energy (101.5 MeV), which is consistent with the Q-value of α-break-up of ^{12}C (-7.272 MeV). The remaining peaks correspond to the ^{12}C recoil nucleus being formed in an excited state and losing energy (e.g. via γ-decay). The peak at $\sim$90 MeV is consistent with the recoil nucleus being emitted in its first excited state at 4.4 MeV, which is the second member of a rotational

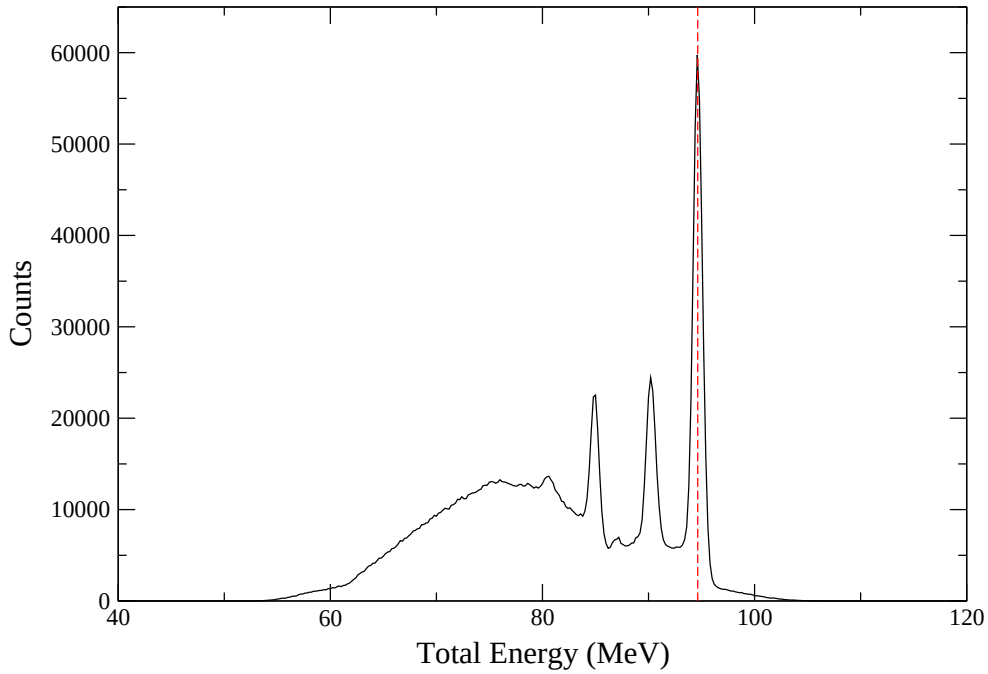

Figure 4.3: Total energy spectrum. The marked peak corresponds to events in which the recoil nucleus was formed in its ground state. The strong peaks at lower energy correspond to the 4.4 and 9.6 MeV excitations of the recoil nucleus.

band built on the ground state configuration. The peak at ∼84 MeV corresponds to the recoil nucleus being emitted in the 9.64 MeV 3^- state.

By gating on the highest energy peak only events in which the recoil nucleus is formed in its (0^+) ground state are selected; this is a requirement of the angular correlation method used later in the analysis. Background events that extend to E_{tot} values greater than the beam energy are believed to most likely arise from pile-up events in which the detected particles are produced from different beam−target interactions. The continuum at lower energies corresponds to events where one of the the detected α-particles came from the break-up of the the ^{12}C recoil.

4.1.4 ^{8}Be break-up Q-value

As discussed previously, the break-up of ^{12}C into 3α-particles occurs sequentially in two steps:

$$^{12}\mathrm{C} \longrightarrow {}^{8}\mathrm{Be} + \alpha \ , \qquad {}^{8}\mathrm{Be} \longrightarrow \alpha + \alpha \ ,$$

where the lifetime of the ^{8}Be nucleus is sufficiently short so as not to affect the overall kinematics i.e. it decays whilst still within the target. The present analysis selected events in which the decay occurs through the ^{8}Be ground state. To select events in which this was the case, the ^{8}Be nucleus was reconstructed and the decay energy calculated in an analogous way to that discussed for the break-up of ^{12}C in section 2.2. The momentum of the ^{8}Be nucleus was calculated by summing the individual momenta of two of the detected α-particles, and repeated for all 2α-particle pairs. In turn, the decay energy of each 2α-pair was calculated using

$$\mathrm{E_{decay}} = \sum_{i=1}^{2} \mathrm{E}_{\alpha_i} - \frac{\mathrm{P_{Be}}^{2}}{2\mathrm{M_{Be}}} \ , \tag{4.4}$$

where E_{α_i} are the energies of two of the two α-particles, $\mathrm{P_{Be}}$ is the momentum of the ^{8}Be nucleus, and $\mathrm{M_{Be}}$ is the mass of the ^{8}Be nucleus. Using cyclic permutations, it is possible to check the Q-value for the break-up of all possible 2α-pairs (see figure 4.4), and filter the events to include only those which match the known value for decay via the ^{8}Be ground state (0.092 MeV above the break-up threshold).

4.2 Main analysis

Initial ^{12}C excitation energy spectrum

Having determined that 3α-particles and ^{12}C have been detected and also that 2α-particles derive from an $^{8}\mathrm{Be}_{\mathrm{g.s.}}$ decay, it is possible to construct an excitation energy ($\mathrm{E_{ex}}$) spectrum

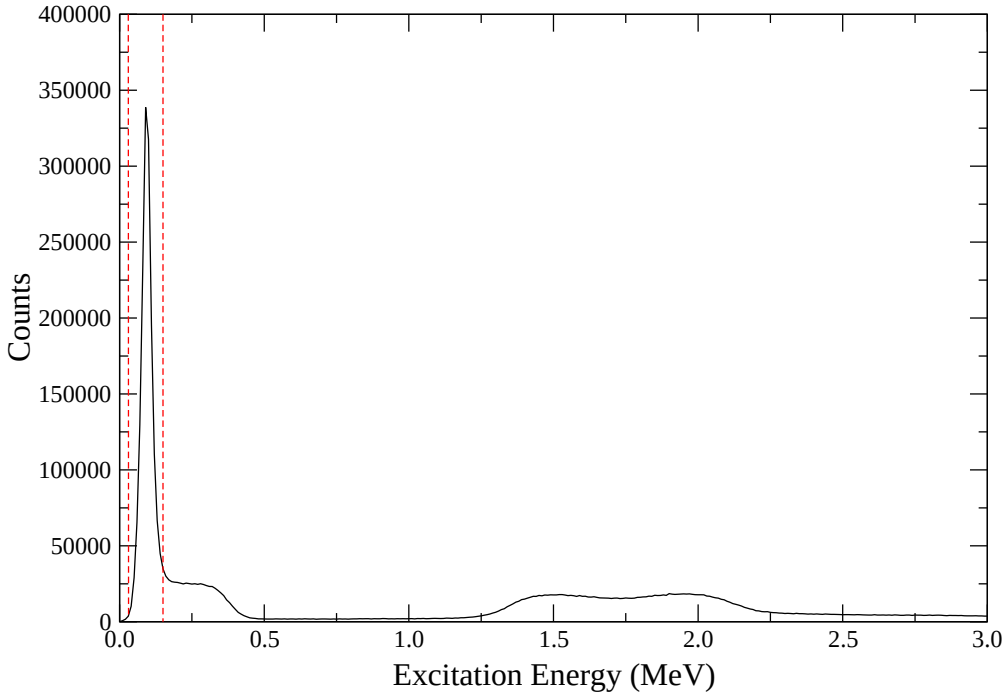

Figure 4.4: Decay energy spectrum for the break-up of ^{8}Be into 2α-particles. The region marked by the dashed lines corresponds to the gate used to select a reaction channel for decays through the $^8\mathrm{Be}_{\mathrm{g.s.}}$. The ground state peak does not appear at zero due to the fact that the decay threshold for ^{8}Be into 2α-particles is 92 keV below the ground state energy. The width of the ground state peak is 39 keV FWHM (notably larger than the the state's known width of 5.5 eV). The double-peak structure is an artifact, arising from incorrect $\alpha - \alpha$ pairing in the construction of the ^{8}Be.

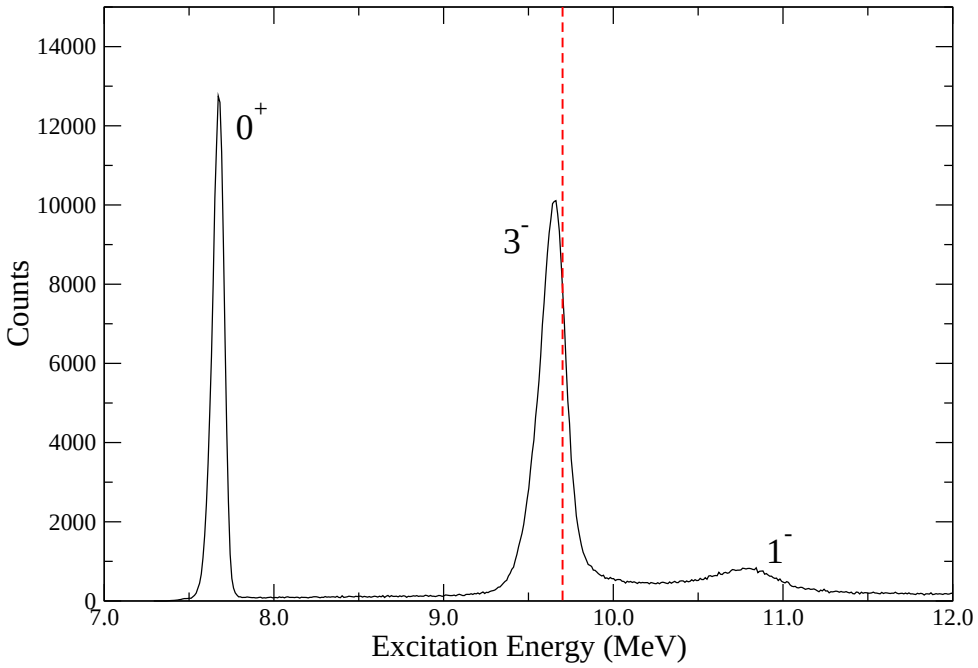

Figure 4.5: Excitation energy spectrum for the break-up of ^{12}C into 3α-particles. The dashed line corresponds to the energy at which the 2^+ excitation was found in [44]. The spins and parities of the known states are labelled.

for the ^{12}C nucleus that decayed, whereby E_{ex} is calculated as discussed in section 2.2:

$$E_{ex} = \sum_{i=1}^{3} E_{\alpha_i} - \frac{P^2}{2M_C} + E_{th} \ , \tag{4.5}$$

where $E_{th} = 7.272$ MeV. Figure 4.5 shows the energy spectrum of the break-up of ^{12}C; a number of known energy levels are labelled (0^+ Hoyle state at 7.654 MeV, 3^- state at 9.641 MeV, 1^- state at 10.84 MeV), along with the location at which Itoh *et al.* claim to have previously found evidence of a 2^+ resonance. The widths of the peaks are dominated by the experimental resolution, which is 90 keV (FWHM) for the 7.65 MeV peak and 175 keV (FWHM) for the 9.64 MeV peak[1]. As can be seen from the figure, in order to investigate the possible existence of a 2^+ resonance in the region of the dashed line it is necessary to

[1]In addition to the detector resolutions, the resolution of the peaks is dependant on the relative angle between the initial scattering particles. This effect is centered around the breakup threshold such that the width of a peak close to the threshold (a small relative scattering angle) will have a considerably improved resolution compared to a state far from the threshold. This effect is discussed in greater detail in [61], which also includes a more rigorous mathematical analysis.

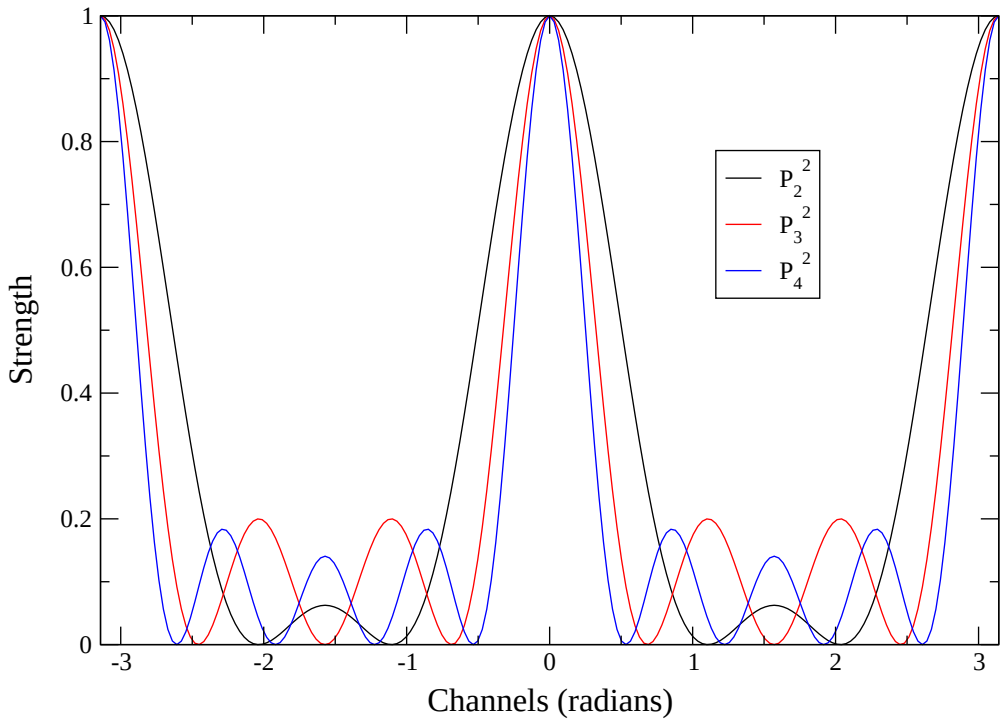

Figure 4.6: Example of the squares of 2^{nd}, 3^{rd} and 4^{th} order legendre polynomials. It can be seen that the minima of $P_2{}^2$ are out of phase with those of $P_3{}^2$. It is using this principle that the angular correlations technique can be used to suppress a $J^\pi = 3^-$ state whilst leaving a 2^+ state unaffected.

suppress the 3^- peak dominant in this part of the spectrum.

4.2.1 Angular correlations

One of the primary analysis techniques employed within this thesis is the use of angular correlation measurements. By plotting θ^* and ψ (angles from two different stages of the break-up process and discussed in section 2.3), against one another it is possible to develop a 2-dimensional plot which reveals information regarding the spin of a state. Due to the 'ridge' structure of these plots, and more specifically the requirement that (when projected at the correct angle – calculated using equation 2.20, and discussed in section 2.3), the ridges follow associated Legendre polynomials, there will be locations at which $J^\pi = 2^+$ and 3^- states' minima and maxima will coincide, and also where they will be out of phase (figure 4.6). The figure also highlights that the technique would be effective for resolving e.g. a $J^\pi = 4^+$ state from a dominant 3^- state, but would not be able to separate a 2^+ state

from a 4^+.

Figure 4.7 shows the initial angular correlation calculations as described in section 2.3.1, in which θ^* and ψ are calculated in the x−z plane. Though it is possible to see some evidence of a ridge structure in the 'eye' of figures 4.7a and 4.7b, it is not a clear structure; there is no structure visible in 4.7c. Another aspect shown by figure 4.7 is the result separating events with different 'hit configurations' from one another. Figures 4.7b and 4.7c show the different angular correlations obtained for '2 : 1' and '3 : 0' patterns (i.e. figure 4.7b shows events with 2 hits in one telescope and 1 in another, figure 4.7c shows events in which 3α particles are all detected in the same telescope)[2]. The excitation energy spectra of the ^{12}C nucleus associated with each part of figure 4.7 were re-plotted (figure 4.8), the effect of separating the 2 : 1 and 3 : 0 coincidences becomming immediately apparent: the 3 : 0 events being associated with the lower region of the ^{12}C excitation energy spectrum, and the 2 : 1 events with the higher region. From this it is also apparent that majority of the data from the region of interest (∼9.7 MeV) is made of 2 : 1 events. However, at this stage it is not possible to discard the 3 : 0 events as there are, nonetheless, still a significant number of points within the 9.64 MeV, 3^-, peak (figure 4.8c).

The angular correlations were re-calculated after performing a rotation into the reaction plane (discussed in section 2.3.2, shown in figure 4.9) and, once again, there is a clear difference in the correlations associated with 3 : 0 and 2 : 1 events. The ridge structure discussed in chapter 2.3 become much clearer in figure 4.9a, and following the separation into different hit configurations it is apparent that while this structure is present in the 2 : 1 events (figure 4.9b), it does not appear in the 3 : 0 events (figure 4.9c). The lack of ridge structure in the 3 : 0 angular correlations suggests that the method is unsuitable to try and suppress the 3^- structure for these events[3]. At this stage it is also possible to re-plot the excitation energy spectrum for ^{8}Be for 2 : 1 events only. This is shown in figure 4.10.

[2]The final possible hit configuration (each α-particle being deposited into a separate telescope) is not included due to the statistics being considerably lower than both 2 : 1 & 3 : 0. This is believed to be due to the low probability of the 2α-particles resulting from the break-up of ^{8}Be having sufficient positional separation to be deposited in different telescopes.

[3]At this stage the 3 : 0 coincidences were removed from the analysis process, significantly speeding up the time required to sort the remaining data.

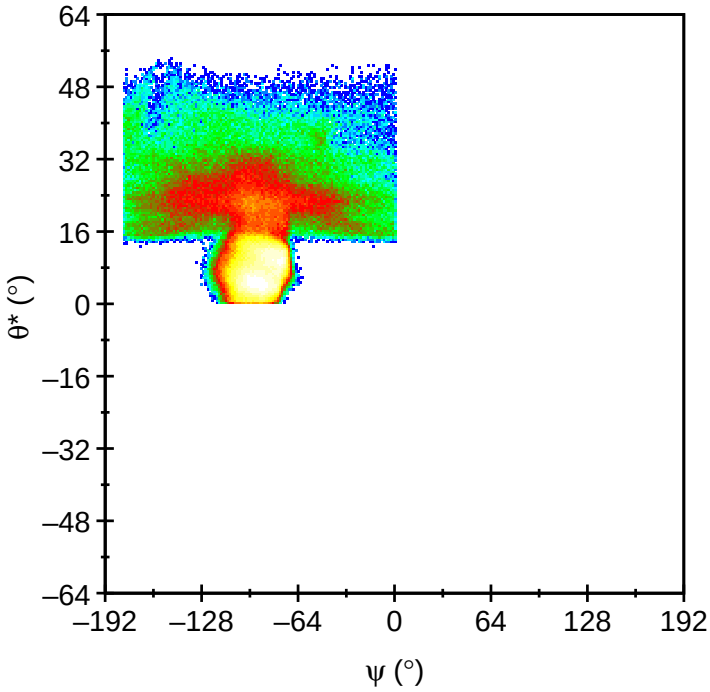

(a) Angular correlations for the complete data set.

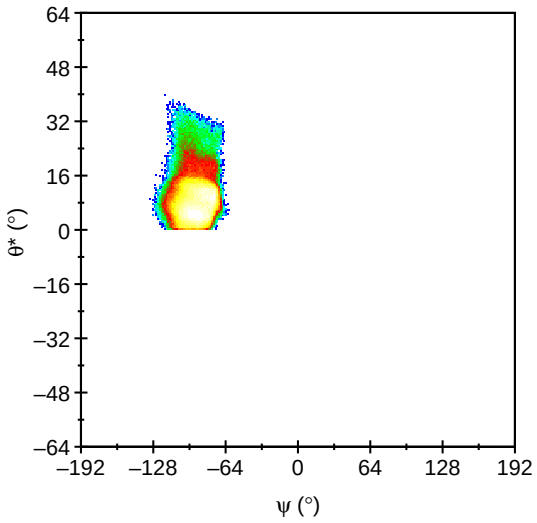

(b) 2 : 1 coincidences only.

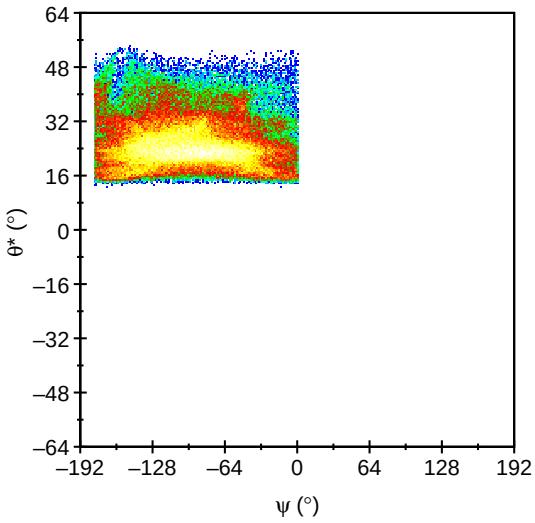

(c) 3 : 0 coincidences only.

Figure 4.7: Angular correlations for (a) all events, (b) 2 : 1 coincidences, (c) 3 : 0 coincidences. Separating the different hit configurations reveals that the ridge structure seen in (a) is as a result of the 2 : 1 coincidences. The lack of structure in (c) is due to the dominance of the 0^+ state in this spectrum (this is highlighted by the excitation energy spectrum for this data shown in figure 4.8c).

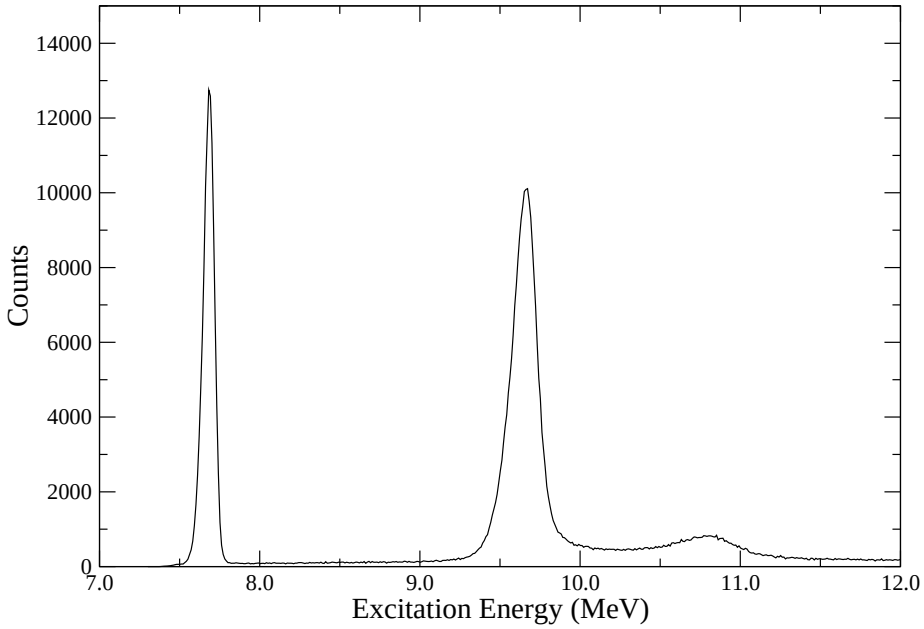

(a) Excitation energy spectrum for the complete data set.

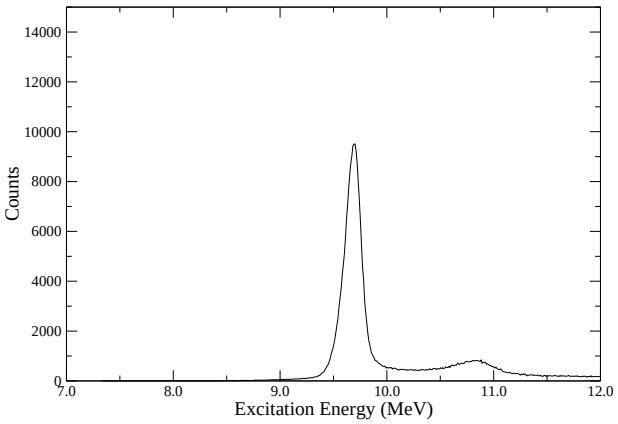

(b) 2 : 1 coincidences only.

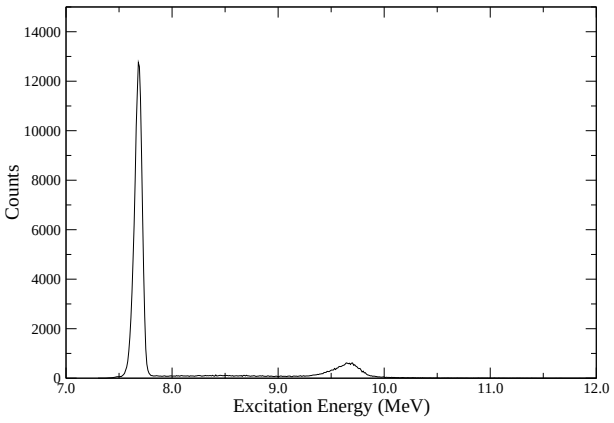

(c) 3 : 0 coincidences only.

Figure 4.8: Excitation energy spectra for the break-up of ^{12}C for (a) all events, (b) 2 : 1 coincidences, (c) 3 : 0 coincidences. The separation of different hit configurations shows a clear link between hit configuration and possible excitation energy.

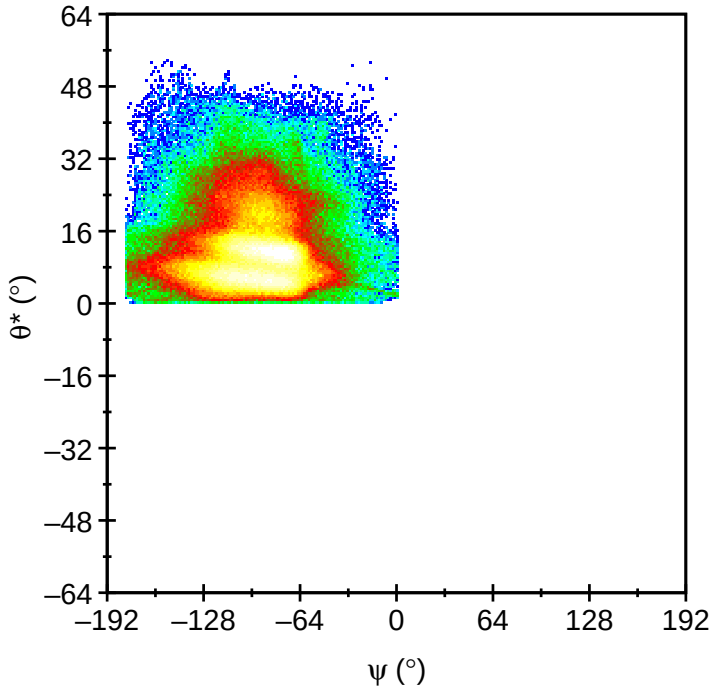

(a) Angular correlations for the complete data set (as calculated in the reaction plane).

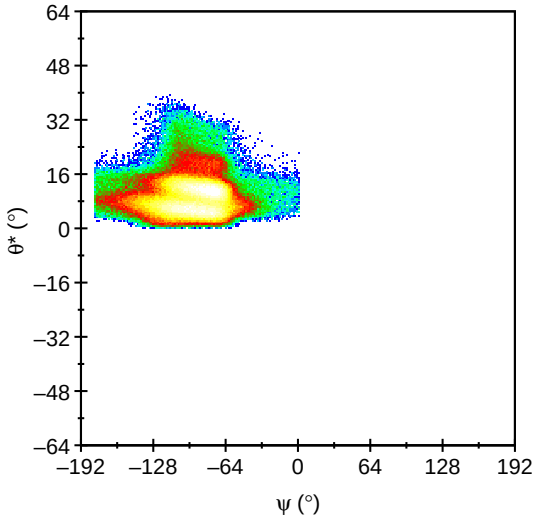

(b) 2 : 1 coincidences only.

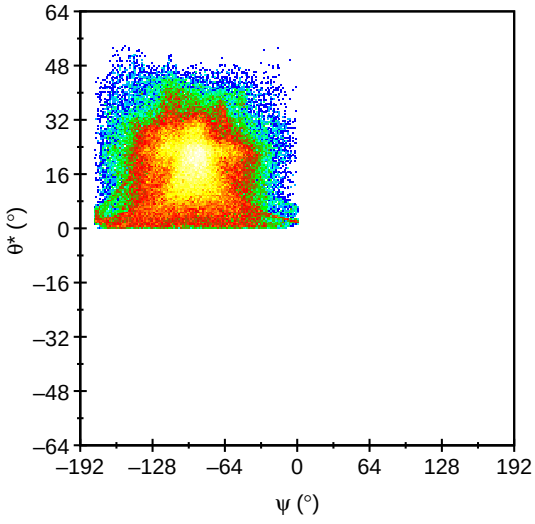

(c) 3 : 0 coincidences only.

Figure 4.9: Angular correlations for (a) all events, (b) 2 : 1 coincidences, (c) 3 : 0 coincidences (as calculated in the reaction plane). The ridge structure seen in figure 4.7 is now more clearly seen, and is once again a result of the 2 : 1 coincidences.

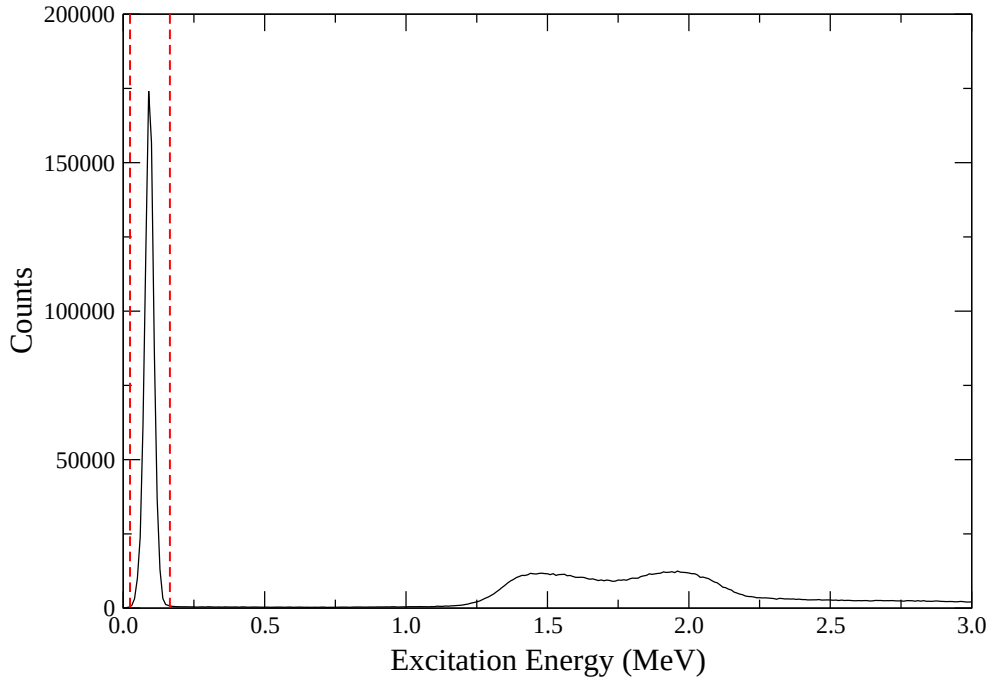

Figure 4.10: Excitation energy spectrum for the break-up of ^{8}Be into 2α-particles following the removal of 3 : 0 coincidences. The high energy shoulder seen on the g.s. peak in figure 4.4 has disappeared, suggesting that incorrect pairings in 3 : 0 events were responsible for this artifact.

From the disappearance of the high energy shoulder seen on the ground state peak in the earlier ^{8}Be excitation energy spectrum, it is possible to determine that this artifact arises from incorrect $\alpha - \alpha$ pairings in the 3 : 0 events.

After determining that the 2 : 1 events were those of most interest the angular correlations were recalculated, this time gating on the 3^- peak in the ^{12}C excitation energy spectrum; the results are shown in figure 4.11. Removing data other than that in the 3^- region further clarifies the ridge structure seen previously. As a check of the spin of the state, the ridges in figure 4.11b can be projected at an angle determined by

$$\frac{\mathrm{d}\theta^*}{\mathrm{d}\psi} = \frac{J}{l_g - J} \,. \tag{4.6}$$

For a grazing angular momentum (l_g) of 22.5$\hbar$ (see section 3.3.3), this corresponds to a projection angle of $\sim$171°; the projected data, along with a 3$^{\mathrm{rd}}$-order Legendre polynomial, are shown in figure 4.12.

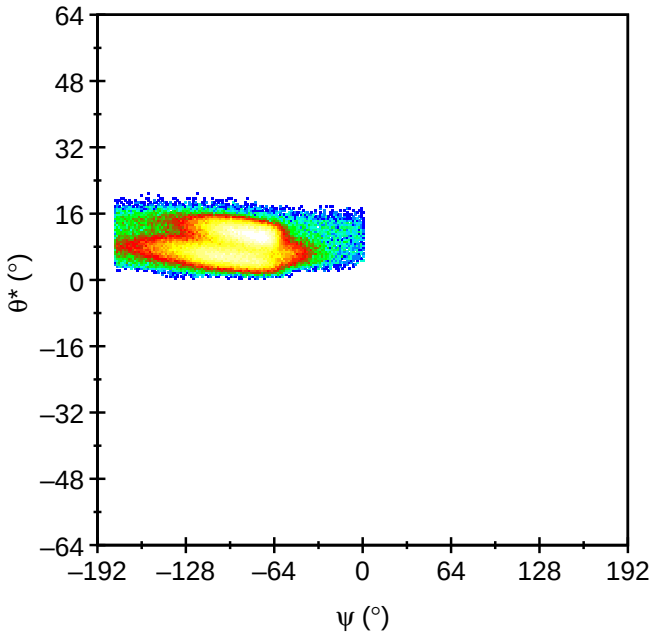

(a) Angular correlations plot for the 3^- region using 2 : 1 coincidences only.

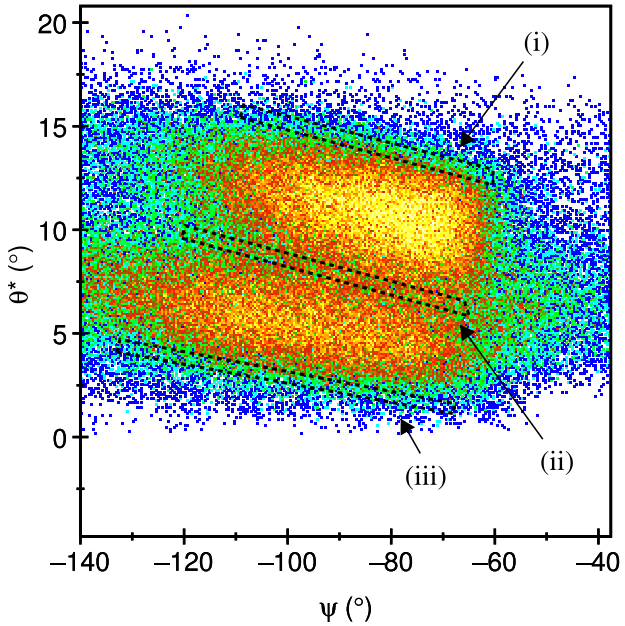

(b) Angular correlations plot for the 3^- region using 2 : 1 coincidences only, magnifying the region of interest. The dashed windows indicate software gates used to select regions over which a 3^- state will be minimal.

Figure 4.11: Angular correlations plots for the 3^- region using 2 : 1 coincidences only (calculated in the reaction plane). The Legendre 'ridge structure' is clearly visible.

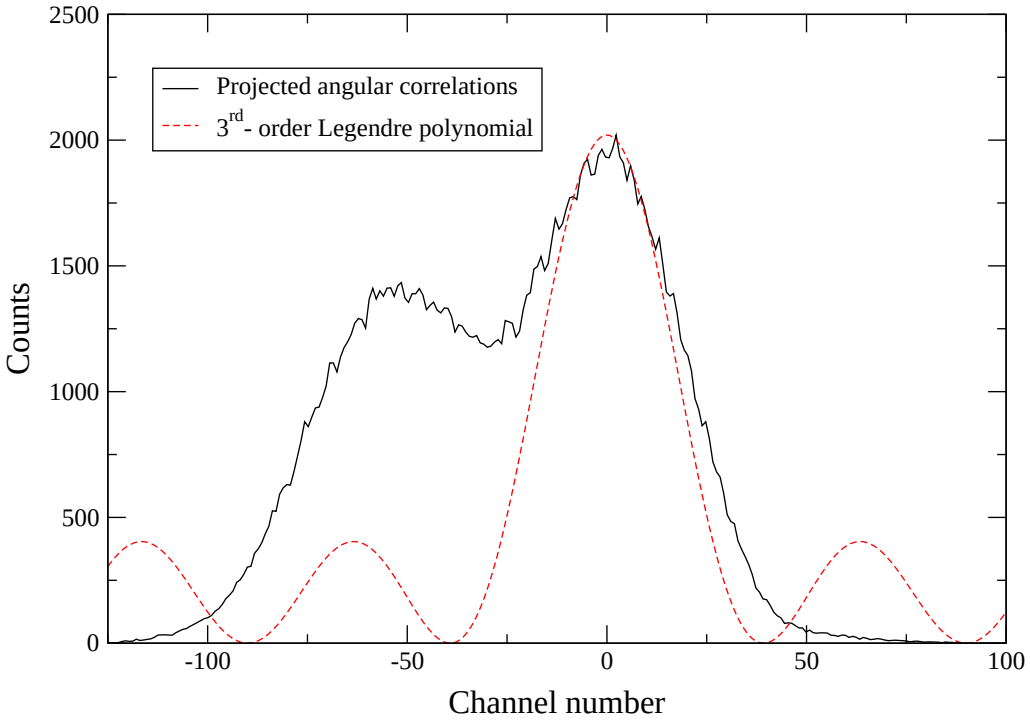

Figure 4.12: Angular correlations projection for the 3^- peak matched against a 3^{rd}-order Legendre polynomial (2 : 1 coincidences only). The data shows a good match to the Legendre polynomial, though an insufficient number of ridges means it is not possible to match to several maxima. (Channel number is an arbitrary unit.)

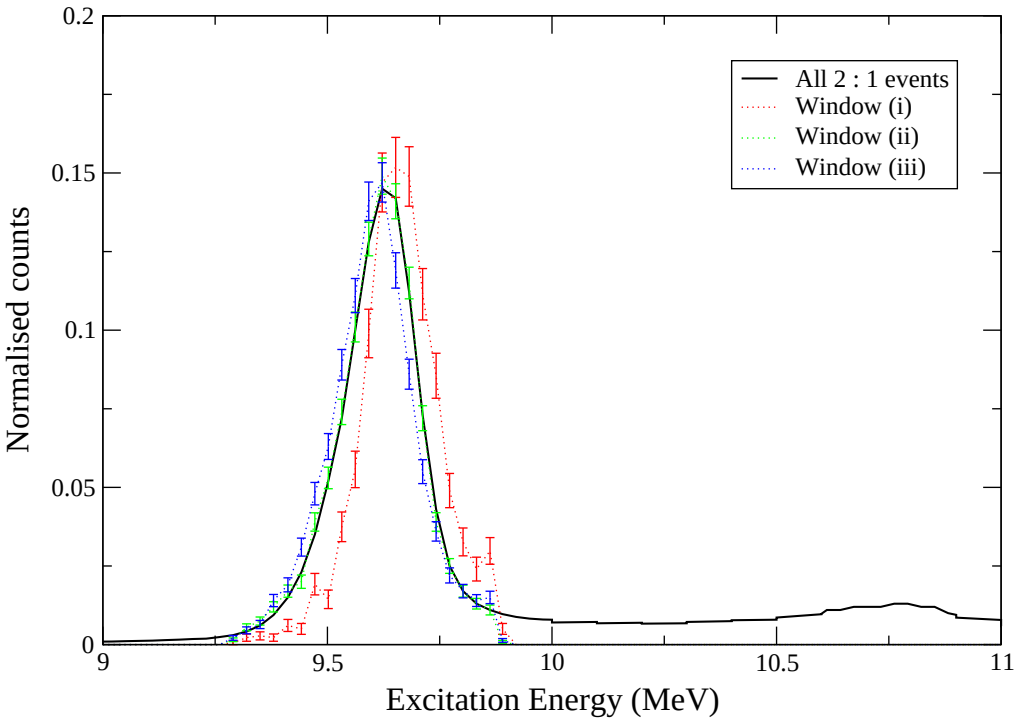

Figure 4.13: ^{12}C excitation energy spectra associated with the software gates as shown in figure 4.11b; also shown is the excitation energy spectrum for all 2 : 1 events. All the spectra have been normalised to the area of the peak in the 3^- region.

Following the construction of the angular correlations for the 3^- peak, it is possible to place software gates in the regions at which a 3^- state will be minimal. Figure 4.11b shows three regions for which ^{12}C excitation energy spectra were constructed (shown in figure 4.13) and compared to the spectrum for all 2 : 1 events. If there were immediate evidence of a 2^+ state in the region of ∼9.7 MeV, it would be expected that the 3^- peak would be suppressed, and to a greater extent on the left-side than the right-side. Instead, it is apparent that over the three software windows, the entire 3^- peak shifts, increasing in energy as θ^* increases. In order to try and understand the origin of this shift, several more windows were constructed at various other locations on the $\theta^* - \psi$ spectrum, and excitation energy spectra created for each of these. It was discovered that these peak-shift effects were seen whenever windows were placed at the limits of the angular coverage of the detectors, indicating a non physical origin of the effect.

Physical parameter	Value
Reaction	^{12}C(^{12}C,^{12}C*)^{12}C
Reaction Q-value	0 MeV
Break-up$_1$ reaction	$^{12}\mathrm{C}^{*} \longrightarrow {}^{8}\mathrm{Be}_{\mathrm{g.s.}} + \alpha$
Break-up$_1$ Q-value	-7.3666 MeV
Break-up$_2$ reaction	$^{8}\mathrm{Be}_{\mathrm{g.s.}} \longrightarrow \alpha + \alpha$
Break-up$_2$ Q-value	0.092 MeV
Excitation energy	$9.64 - 9.70$ MeV
State width	$0.034 - 0.6$ MeV
Beam energy	101.5 MeV
Target thickness	50 μg/cm^2
Target density	2.25 g/cc
Beam energy spread from detector	0.0004
In-plane beam divergence	0.4°
Out-of-plane beam divergence	0.4°

Table 4.1: Parameters used in the Monte-Carlo simulations of ^{12}C(^{12}C,^{12}C[3α])^{12}C.

4.3 Introducing Res8 Monte Carlo simulations

To better understand the effects seen in figure 4.13, the Res8 code was used to perform Monte Carlo simulations to investigate whether simulations of a $J = 3$ and also a $J = 2$ state could recreate the spectra seen in the experimental data. The parameters used for the simulations are shown in table 4.1. An angular correlation analysis was performed on both simulations (figure 4.14) in exactly the same manner as for the experimental data and, as seen in figure 4.14a, the $J = 3$ simulation reproduces rather well the angular correlations seen for the experimental data, although additional features are also present in the experimental data. It is also apparent that the minima/maxima of the $J = 2$ and $J = 3$ simulations are out of phase as would be expected. The same software windows were placed on the $J = 3$ simulations (figure 4.14a) as previously used with the experimental data (figure 4.11b) and a similar spectrum generated to figure 4.13, in which the ^{12}C excitation energy spectra for each window are compared to that for the complete data set; this is shown in figure 4.15. Unlike for the experimental data, spectra produced from the simulations (from windows placed near the extremities of the telescopes' angular coverage) did not result in peak shifts in the ^{12}C excitation energy spectrum. It is thought that the cause of the peak-shift seen in

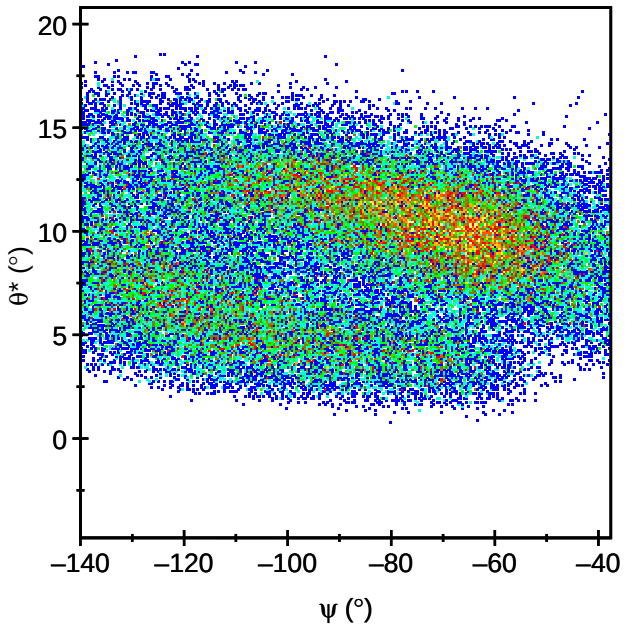

(a) Angular correlations for a Monte Carlo generated 3^- state using 2 : 1 coincidences.

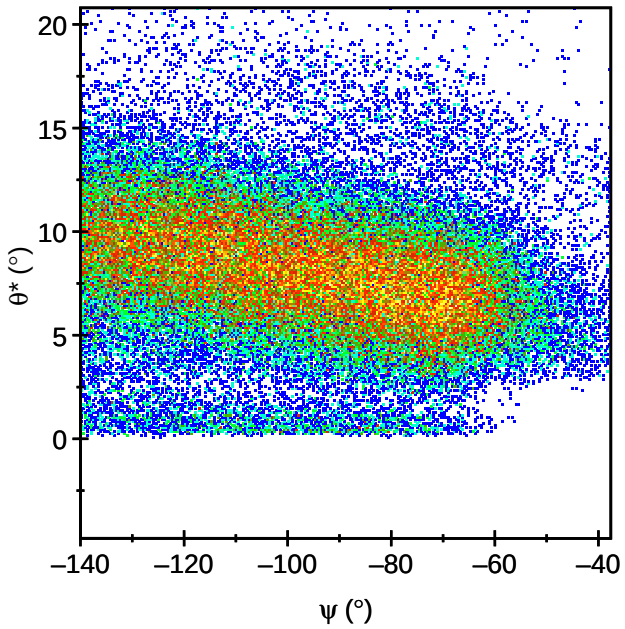

(b) Angular correlations for a Monte Carlo generated 2^+ state using 2 : 1 coincidences.

Figure 4.14: Angular correlations plots for the Monte Carlo simulations of (a) a $J = 3$ state, and (b) a $J = 2$ state, using 2 : 1 coincidences only (calculated in the reaction plane). The simulations in (a) show a good match to figure 4.11b, though there appears to be further structure in the experimental data compared to the $J = 3$ simulation. It is unclear whether this is possible to explain by combining the $J = 3$ simulation with the $J = 2$ simulation or whether this additional structure arises from elsewhere.

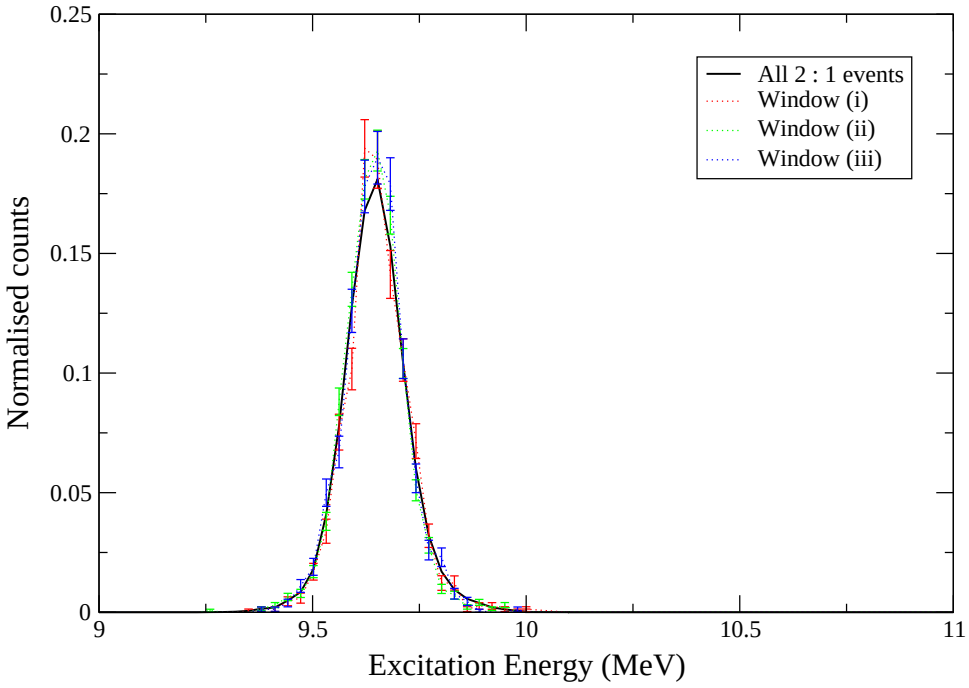

Figure 4.15: ^{12}C excitation energy spectra associated with Monte Carlo simulations of a $J = 3$ state using the same windows as in figure 4.11b; also shown is the excitation energy spectrum for all $2:1$ events simulated. All the spectra have been normalised to their area.

the experimental data is therefore not due to the underlying physics of the reaction process, but rather is an artifact of the detector alignment. Though attempts to investigate the exact nature, and also the cause, of this shift effect did not result in a good understanding, it is nonetheless an important result, as it is known that further investigation into the 2^+ excitation should not include data collected at the limits of the detectors' angular coverage.

4.3.1 Using Res8 simulations to develop experimental analysis techniques

Although the simulations discussed previously reveal an effect in the experimental analysis, the cause of which is unknown, the Res8 simulations can further be used to try and predict where in the $\theta^* - \psi$ plane *is* a good location to effectively minimise the contribution of the 9.64 MeV, 3^-, state. In order to ascertain the best way to identify the possible existence of a 2^+ state in the experimental data, the simulations were used to try and predict where

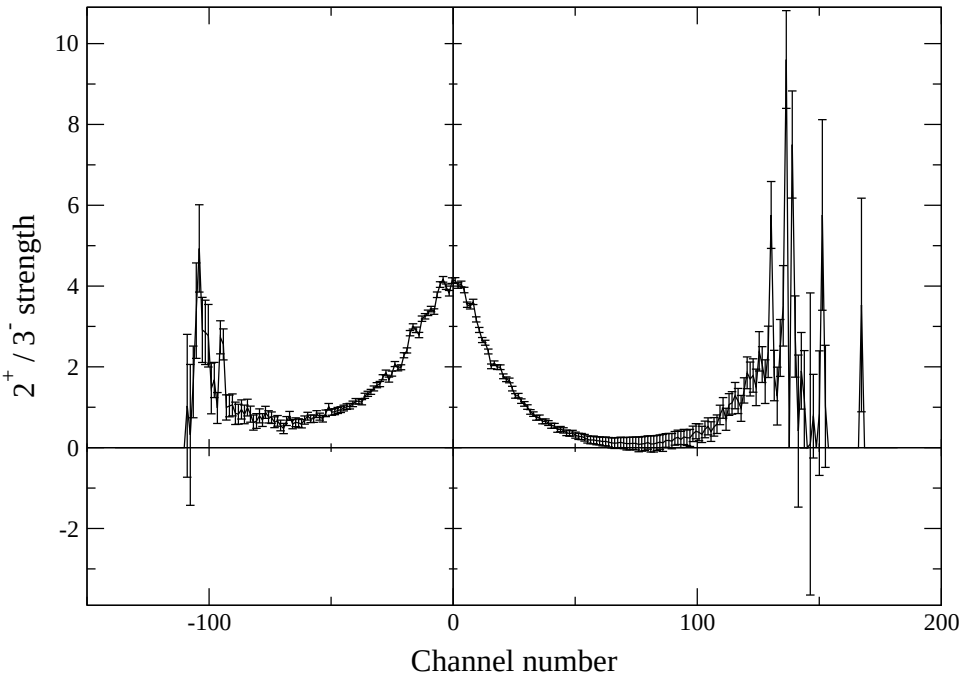

Figure 4.16: Relative strengths of $J = 2$ and $J = 3$ Monte Carlo simulation angular correlations when projected at ∼174.5°. Both the strength and channel numbers are in arbitrary units.

(in the angular correlations spectrum) a 2^+ state would be strongest when compared to a 3^- state. The angular correlations of both simulations were projected at the angle at which the ridges associated with a 2^+ state would be expected to lie (calculated to be ∼174.5°). The projections were then divided by one another, resulting in a prediction of the relative strength of a $2^+/3^-$ across the range of the angular correlations (figure 4.16). As may be expected from the previous plots, (relative to a $J = 3$ state) a $J = 2$ state would be expected to be most noticeable in the minima of the ridges of a 3^- state's angular correlations. Three such minima exist in the coverage of the detector telescopes, but two of these (windows (i) and (iii) of figure 4.11b) lie at, or near to, the limit of the angular coverage. In addition to the 'peak-shift' problem discussed previously, this also results in both these regions suffering from poor statistics – as indicated by the large errors in figure 4.16.

Following the predictions of where a 2^+ state would be most readily identifiable using angular correlations, a similar process was applied to the experimental data. As it is not possible to simply divide a 2^+ contribution by a 3^- contribution an analogous method was

used: the angular correlations spectrum was divided into 20 windows like those shown in figure 4.11b. Each window was of equal width and each was drawn at the angle at which a 2^+ state would be expected to lie. A ^{12}C excitation energy spectrum was then constructed for each of these windows and the strength of a possible 2^+ contribution extracted for each, with a plot of 2^+ strength against window number plot being analogous to the $2^+/3^-$ against channel number plot constructed for the simulations.

In order to arbitrarily ascertain the strength of 2^+ contribution for each window, a fitting routine was developed using the MathCad software package. The excitation spectrum of each window was normalised to, and then subtracted from, an excitation spectrum constructed for the complete $(2:1)$ data set[4]. A fitting routine was then applied to the remainder which was optimised using a variable in the form of a 2^+ contribution in the window's spectrum. The fitting routine was constructed from the difference of two Gaussians:

$$f(E_x) = \frac{\exp\left[-\left(\frac{E_x-c_1}{\sqrt{2}\sigma_1}\right)^2\right] + \alpha\exp\left[-\left(\frac{E_x-c_2}{\sqrt{2}\sigma_2}\right)^2\right]}{\sqrt{2\pi}\left(\sigma_1+\alpha\sigma_2\right)} - \frac{\exp\left[-\left(\frac{E_x-c_1}{\sqrt{2}\sigma_1}\right)^2\right] + \beta\exp\left[-\left(\frac{E_x-c_2}{\sqrt{2}\sigma_2}\right)^2\right]}{\sqrt{2\pi}\left(\sigma_1+\beta\sigma_2\right)}\,, \tag{4.7}$$

where E_x is the excitation energy, c_1 and c_2 are the centroids of the 3^- and 2^+ states (9.64 MeV and 9.7 MeV[5] respectively), σ_1 and σ_2 are the widths of the 3^- and 2^+ states (150 keV[6] (FWHM) and 600 keV[7] (FWHM)), and α and β are the strengths of the 2^+ state across the spectrum as a whole and for an individual window, respectively. It should be noted that the width parameters σ_1 and σ_2 described within the Gaussians are related to state width (Γ) by the relationship

$$\Gamma = 2.35 \times \sigma\ . \tag{4.8}$$

[4]The normalisation was carried out using the area of the 3^- peak. The area was calculated using the Birmingham University Fast Fit (BUFFIT) routine included in the SunSort package.

[5]The centroid position of the 2^+ is taken from [44].

[6]Limited by the experimental resolution.

[7]Based on results from iThemba [45].

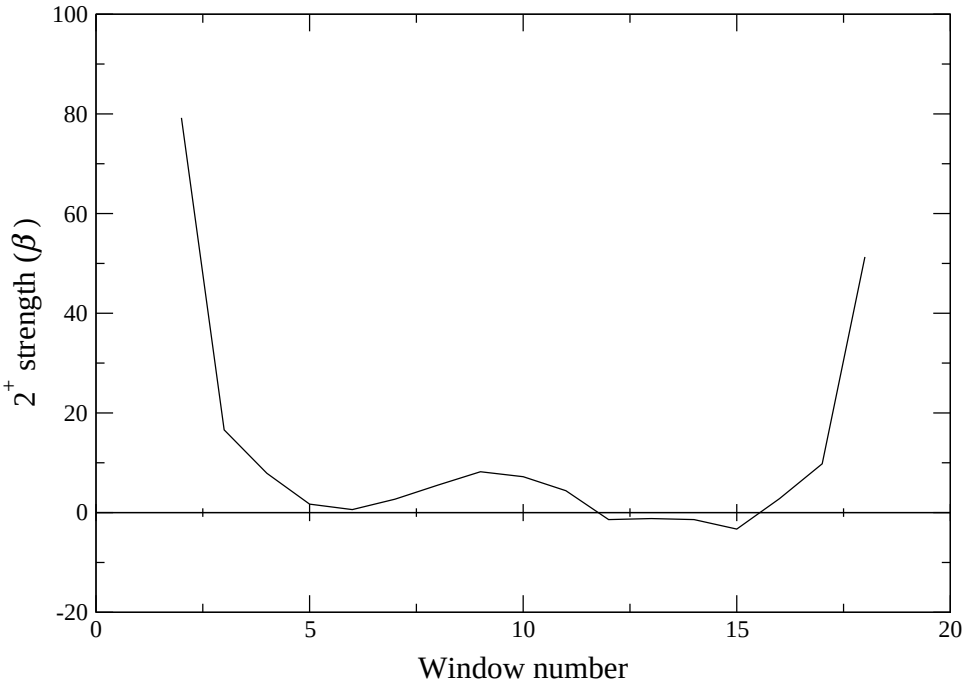

Figure 4.17: Relative strength of $J = 2$ state (centroid position 9.7 MeV) across the angular correlations spectrum (window number increases with θ^*). Inclusion of errors in the spectrum is not trivial, being dependent on both the statistics associated with each window and also the manner in which the fitting routine deals with its variable/input parameters. A variation to the input parameters results in the overall magnitude of every point on the spectrum changing by a constant amount in β, and thus a consistent variation to each window does not affect the characteristic two-minima 'W' shape. Windows 1, 19 and 20 have been omitted from the plot as poor statistics result in values of β several orders of magnitude larger than those from windows $2 - 18$. The 2^+ strength is in arbitrary units.

The value of α is unknown and was estimated to be a few percent (relative to the contribution of the 3^- state); β was varied by the fitting routine for each window to optimise the fit to the data. The strengths calculated by the routine for each window were then plotted against the window number in order to replicate figure 4.16 for the experimental data (figure 4.17). The general trend shown in the experimental is the same as that seen in the Res8 simulations, though with a more pronounced 2^+ contribution at high/low θ^* relative to in the central θ^* region.

Examples of the excitation energy spectra for various windows are shown in figure 4.18. While it is clear, even without employing a fitting routine, that there is a 'remainder' structure in the spectrum for window 18, it is not certain whether this structure is due to an

unknown state underlying the 3^- peak or an artificial effect similar to the peak shifts seen previously, and this must be further investigated before any further analysis can be performed.

4.3.2 Further checks into peak shifts in the experimental data

The peak shift seen in the experimental data is absent from the analysis of the Monte Carlo calculations. This suggests that it does not occur as a result of the underlying physics of the reaction process and it is important to investigate the effect further. If the peak shift is an effect that occurs only at the limits of the angular coverage of the detectors, it can be remedied by discarding outlying points. However, if the peak shift is continuous throughout the data and occurs at all values of θ^* then this must be investigated, and if possible remedied, before further analysis can continue.

A check was performed which again compared the difference between a region at which the 3^- is thought to be dominant, but this time against a data set comprising all the data except that at the extremities of the $\theta^* - \psi$ plot[8]. This analysis was performed twice, separately comparing the ^{12}C excitation energy spectrum for the complete data set to that for each of the 3^- maxima ridges (again normalising both spectra by the integrated number of counts in the 3^- peak); the software windows used are shown in figure 4.19. By subtracting a spectrum expected to be dominated by the 3^- peak from the complete data set, any underlying structure will be revealed. If the peak-shift is θ^*-dependent, the results of comparing windows (i) & (iii) and (ii) & (iii) should result in differing structures, whereas if it is an effect occurrent only at the angular limits then the spectra should have a consistent structure; the results of the comparisons are shown in figure 4.20. The similar structure of both figure 4.20a and 4.20b suggests that the peak shift seen previously is not consistent across the spectrum and may indeed be an effect seen only at the limits of the angular coverage.

A second check is for any discrepancy in azimuthal symmetry in the experimental data. Using only two telescopes (3 and 4) the events were filtered further, and the previous analysis

[8]Due to the effect of peak shifts seen at the limit of angular coverage then the outermost data points were discarded. Any peak shift seen in the remaining data cannot therefore be explained as effects arising from data points at the detector limits.

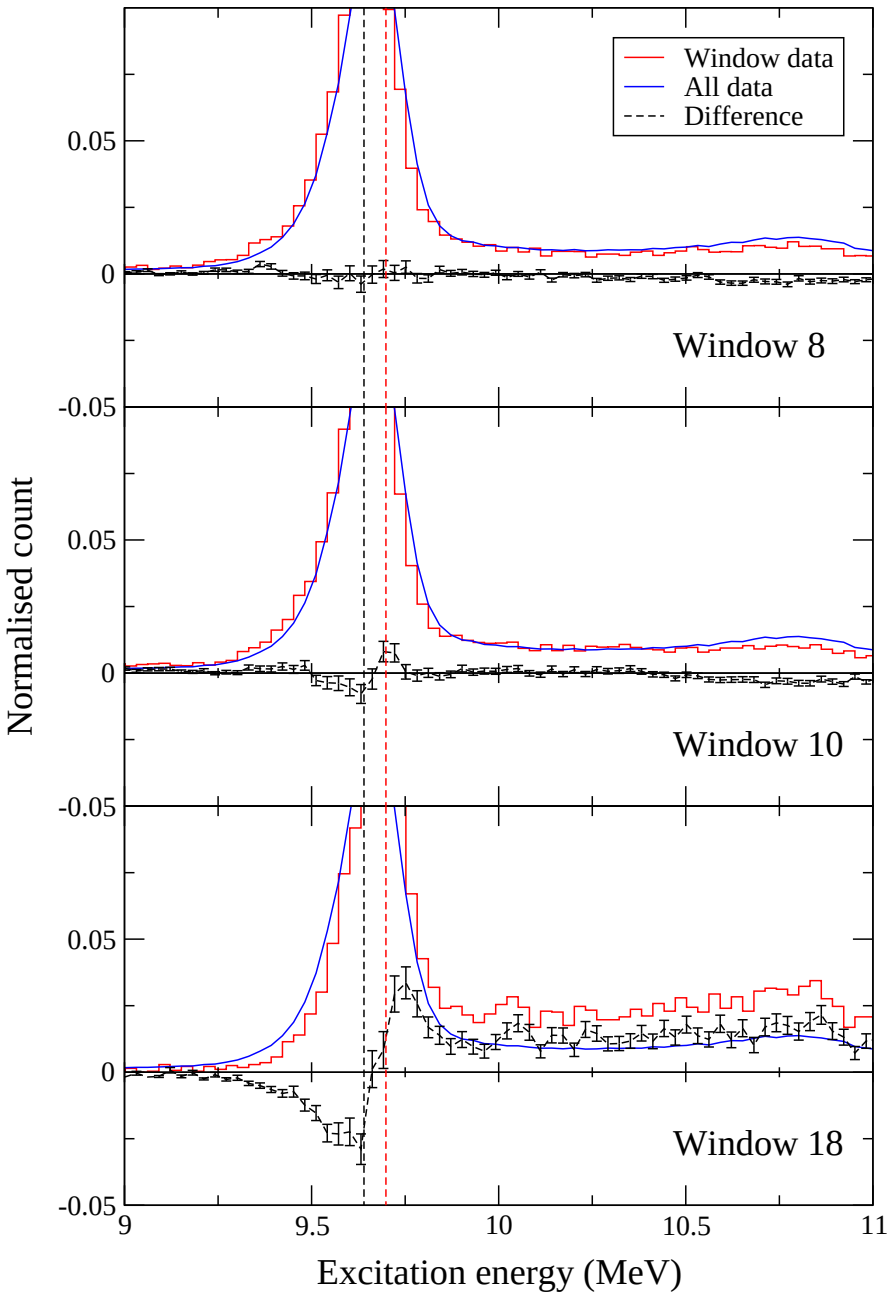

Figure 4.18: Excitation energy spectra for three different windows associated with figure 4.17. Window 8 is from a region in which the 3^- state is expected to be dominant, window 10 is from the central 'valley' between the two 3^- ridges, and window 18 is from a region at the edge of the detectors' angular coverage (again at which the contribution of a 3^- state is expected to be minimal). The black and red vertical dashed lines correspond to the centroid positions of the 3^- state and Itoh's reported 2^+ state [44] (9.64 MeV and 9.7 MeV respectively). All spectra are normalised by dividing each channel by the integrated number of counts in the 3^- peak.

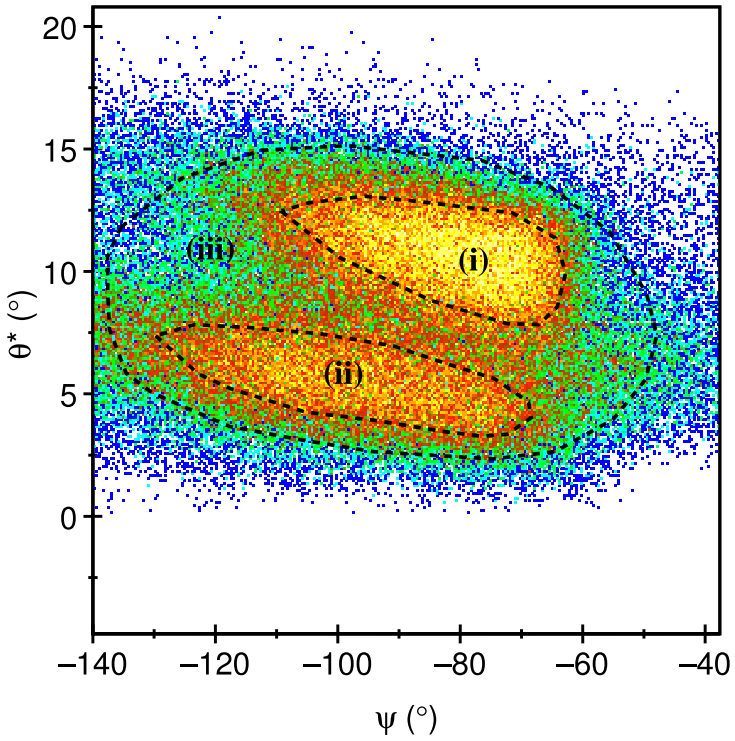

Figure 4.19: Positions of software windows used to check for consistency in the difference between ^{12}C excitation energy spectra for two different dominant 3^- regions and the entire dataset. Windows (i) & (ii) are placed over regions expected to be dominated by the 9.64 MeV 3^- state; window (iii) selects the entire data set (discarding potentially problematic points at the angular limits of the detectors) for comparison with windows (i) & (ii).

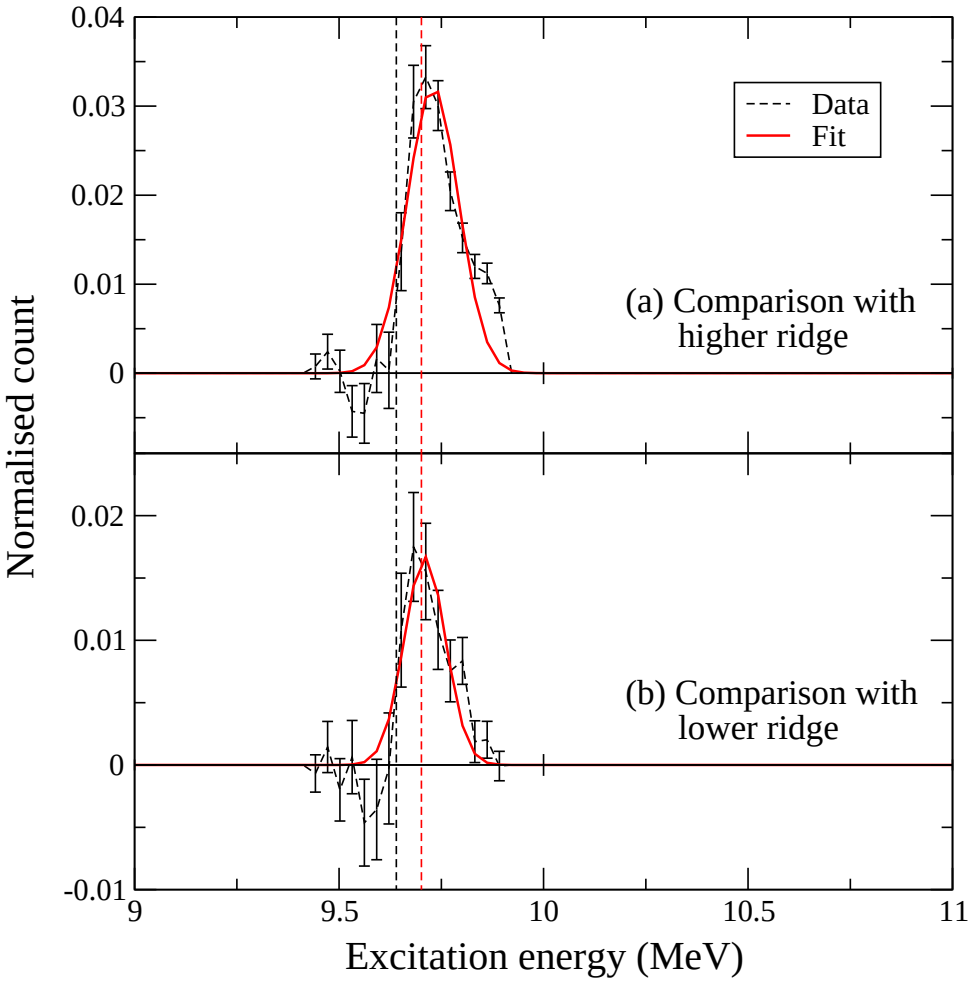

Figure 4.20: Differences in ^{12}C excitation energy spectra for complete data set compared to (a) high and (b) low 3^- maxima ridges. Though the apex of the peaks shifts slightly (by 1 channel), there is no immediate suggestion of a peak shift. The black and red dotted lines mark 9.64 MeV and 9.70 MeV respectively.

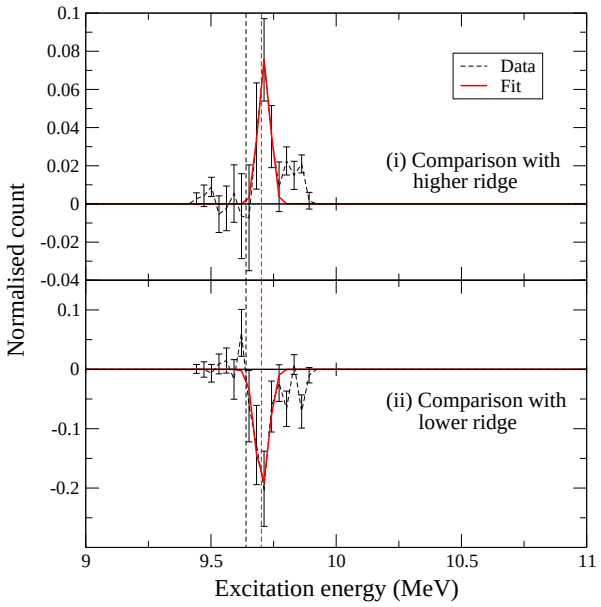

(a) 1 : 2 coincidences.

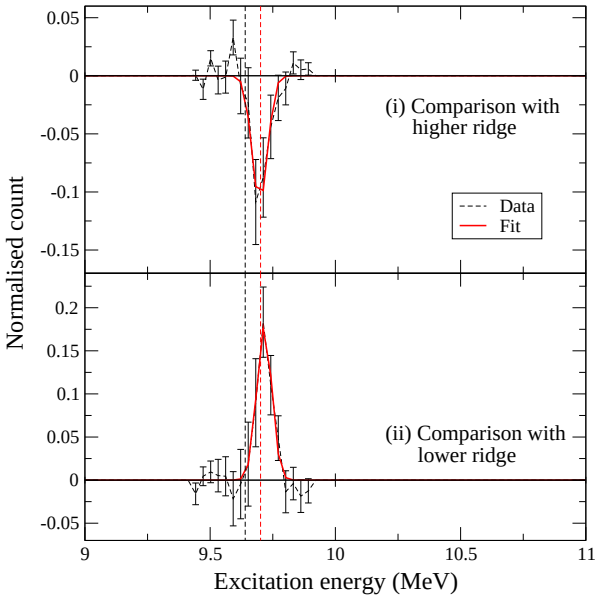

(b) 2 : 1 coincidences.

Figure 4.21: Differences in ^{12}C excitation energy spectra after separating (a) 1 : 2 from (b) 2 : 1 events. The spectra show the difference between the complete data set and (i) high and (ii) low 3^- maxima ridges.

repeated separately for events in which two α-particles were deposited in telescope 3, to those when two α-particles were deposited in telescope 4 (i.e. 1 : 2 and 2 : 1 hit pattern events). The results are shown in figure 4.21. The appearance of 'negative' peaks in two spectra, as well as a lack of azimuthal symmetry (that the negative peak appears when compared to the lower ridge for 1 : 2 coincidences, but when compared to the higher ridge for 2 : 1 coincidences) suggest that there are indeed effects occurring in the central $\theta^* - \psi$ region that are related to some property of the detector or beam alignment.

Following the inconsistencies found in figure 4.21, the previous analysis of comparing the difference in the excitation energy spectra for a region of 3^- minimum compared to the whole data set for the 3^- peak (comparing the spectrum of window (ii) in figure 4.11b to that of window (iii) in figure 4.19) was repeated, this time separating 1 : 2 and 2 : 1 events. The result of these comparisons can be seen in figure 4.22. The lack of symmetry between the two spectra reinforces the suspicion that there is a problem in the analysis process and

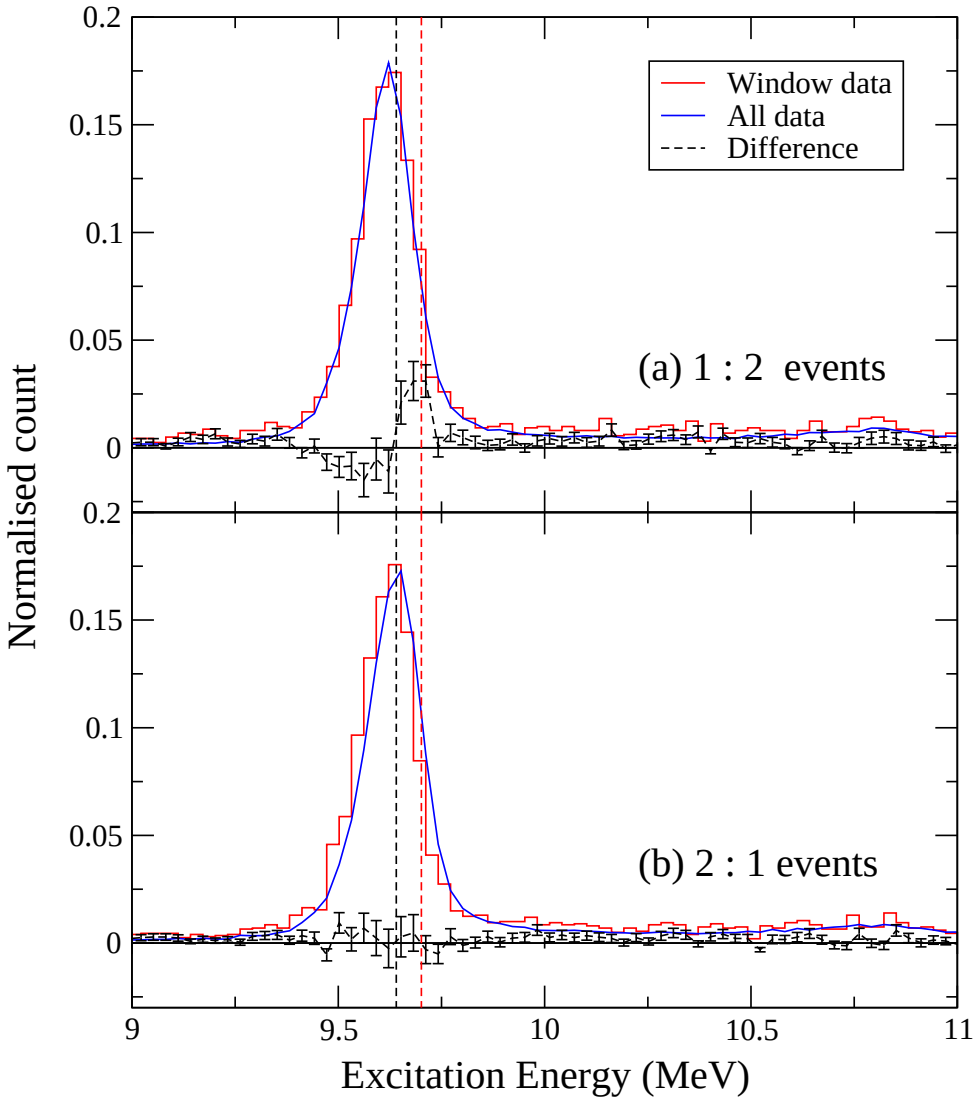

Figure 4.22: Differences in ^{12}C excitation energy spectra between regions of minimum and maximum 3^- contribution for (a) 1 : 2 events, and (b) 2 : 1 events. The vertical dashed lines correspond to excitation energies of 9.64 MeV (black) and 9.7 MeV (red). The remainder seen in (a), which is absent in (b), suggests an azimuthal asymmetry in the results.

the discrepancy is not a 'real' signature of a 2^+ state.

4.4 Investigations into positional offsets using Monte Carlo simulations

Observations made during the set-up of the experiment indicated of a possible offset in the position of a detector telescope[9]. To investigate the consequences of an offset in the position of a detector, and whether it may explain any of the effects seen in the above analysis, further Res8 Monte Carlo simulations were performed.

4.4.1 Linear shift offsets

The first offsets to be investigated were the possible effects of a positional offset in the detector telescopes. Initial simulations involved simple investigations involving shifting a detector telescope by a small amount in a direction parallel to the (RS) detector strips[10].

In order to investigate the plausibility of such an offset explaining the differences in figures 4.22a and 4.22b it is important that any effects seen in the simulations do not display an azimuthal symmetry. The method used to perform the Monte Carlo simulations resulted in the hits always being 2 : 1 coincidences; to test the azimuthal symmetry, simulations were performed in which the shift was introduced into the telescope in which only a single α-particle was detected (singles telescope), and separately simulations were also performed in which the shift was introduced to the telescope in which the two ^{8}Be α-particles were detected (doubles telescope). Figure 4.23 shows the 3^- and 2^+ Monte Carlo simulated ridges once again, but with the software window overlaid; the results of the shifts on the excitation energy spectra are shown in figure 4.24. Though the introduction of a parallel shift clearly affects the shape and position of the 3^- peak, and there is a difference in the effect on 1 : 2 to 2 : 1 events, it is similar in both windows[11].

[9] Telescope no. 4, a DSSD, RS, CsI telescope

[10] Although the offsets could be applied to the simulations directly, due to the time taken to run the Res8 code, they were instead introduced into the analysis sort code. This was done by introducing an error into the momentum of a 'detected' simulation hits for a given telescope equivalent to the telescope's position being shifted.

[11] Though the amplitude of the window peak increases with the shift, while it decreases for the 'all' data,

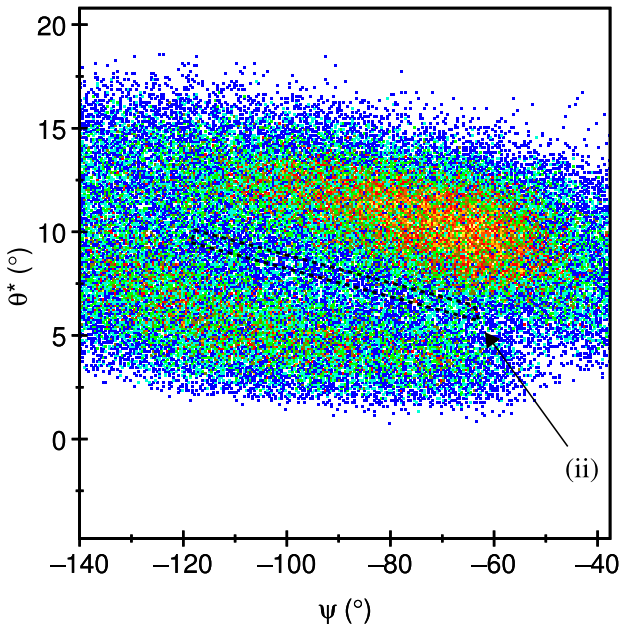

(a) Angular correlations for a Monte Carlo generated 3^- state using 2 : 1 coincidences.

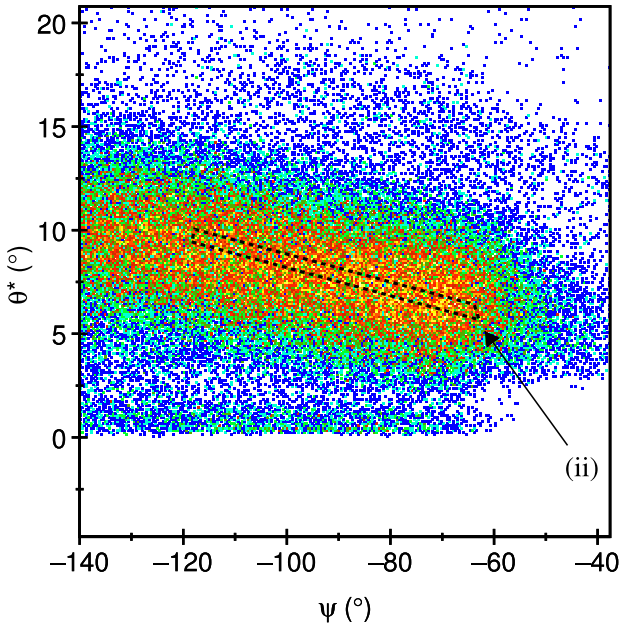

(b) Angular correlations for a Monte Carlo generated 2^+ state using 2 : 1 coincidences.

Figure 4.23: Angular correlations plots for the Monte Carlo simulations of (a) a $J^\pi = 3^-$ state, and (b) a $J^\pi = 2^+$ state, using 2 : 1 coincidences only (calculated in the reaction plane). The software window (window (ii)) used to to gate on the 3^- minimum is overlaid on both spectra, and is shown to also coincide with a maximum region of the 2^+ simulation.

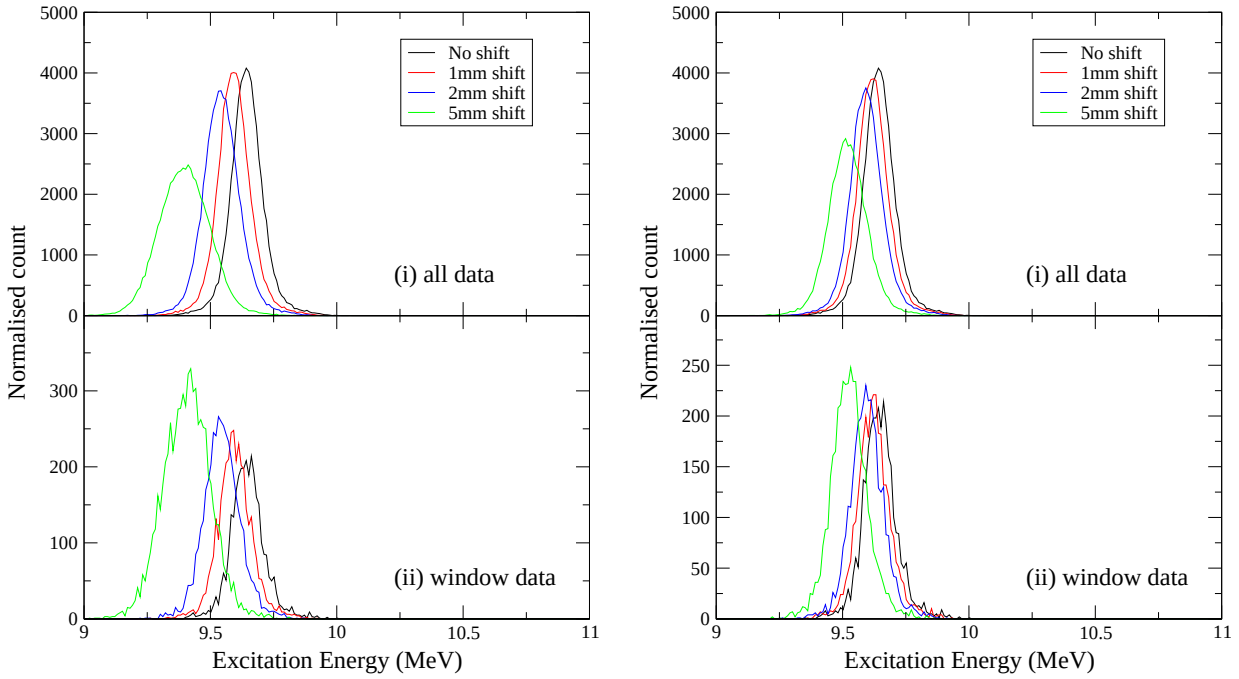

(a) Shift applied to the singles telescope.

(b) Shift applied to the doubles telescope.

Figure 4.24: Effect of introducing a linear shift to the position of a detector telescope in a direction parallel to the (RS detector) strips. All shifts involve moving the telescopes outwards from the beam-spot. The effect of introducing a shift is shown separately for moving (a) the singles telescope, and (b) the doubles telescope. The simulations suggest that the introduction of a detector shift will affect the shape and position of the 3^- peak, though the result is the same for both windows.

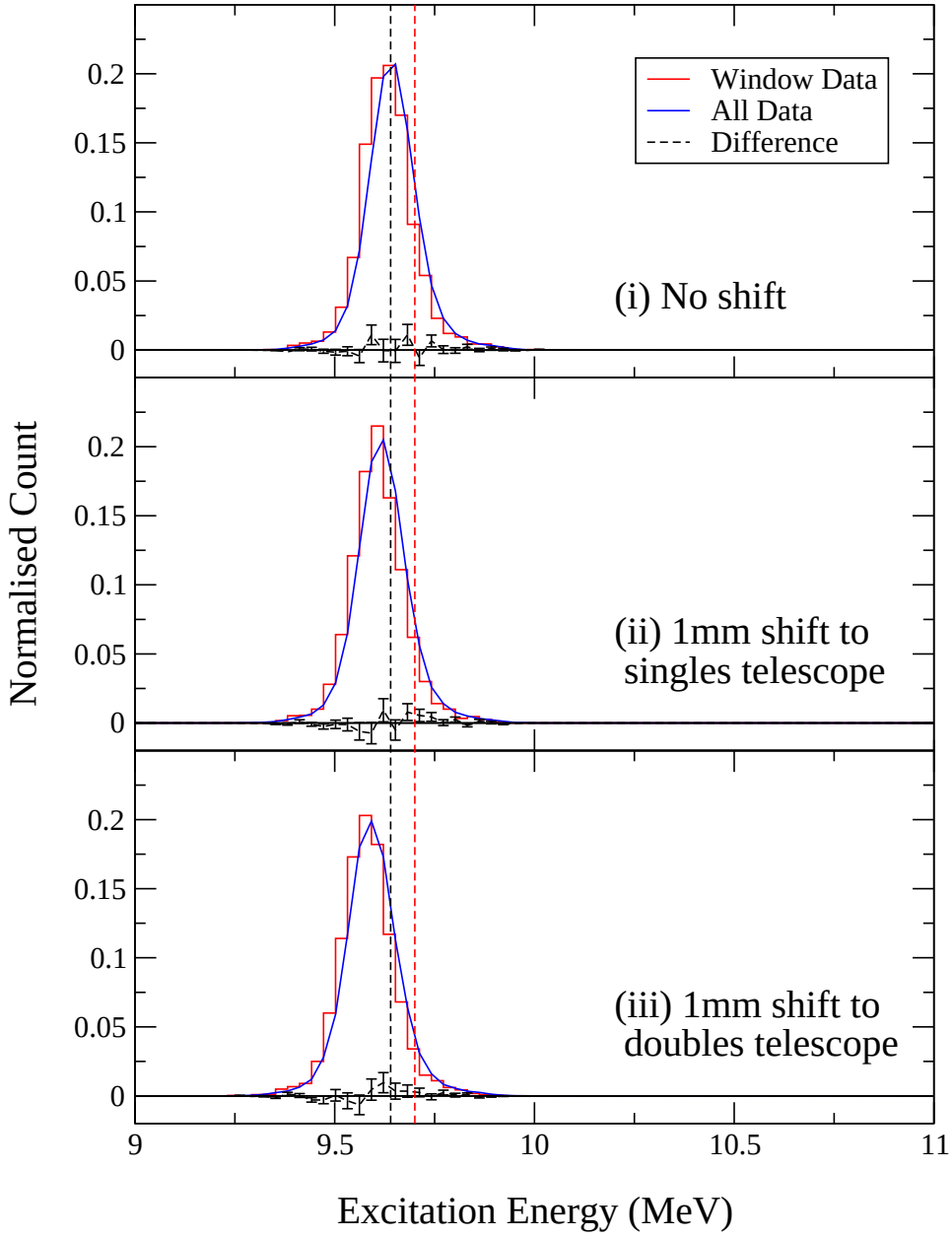

Figure 4.25: A more detailed analysis of the Monte Carlo simulations with a 1 mm shift introduced in a direction parallel to the detector strips. The black and red dashed lines correspond lie at 9.64 MeV and 9.70 MeV respectively. Comparing the normalised spectra from both the windowed and complete data sets shows that there is no significant remainder in any of the spectra. It is also possible to see that there is a noticeable shift in the centroid position of the 3^- peak for even a 1 mm offset. This contradicts what was seen in the experimental data.

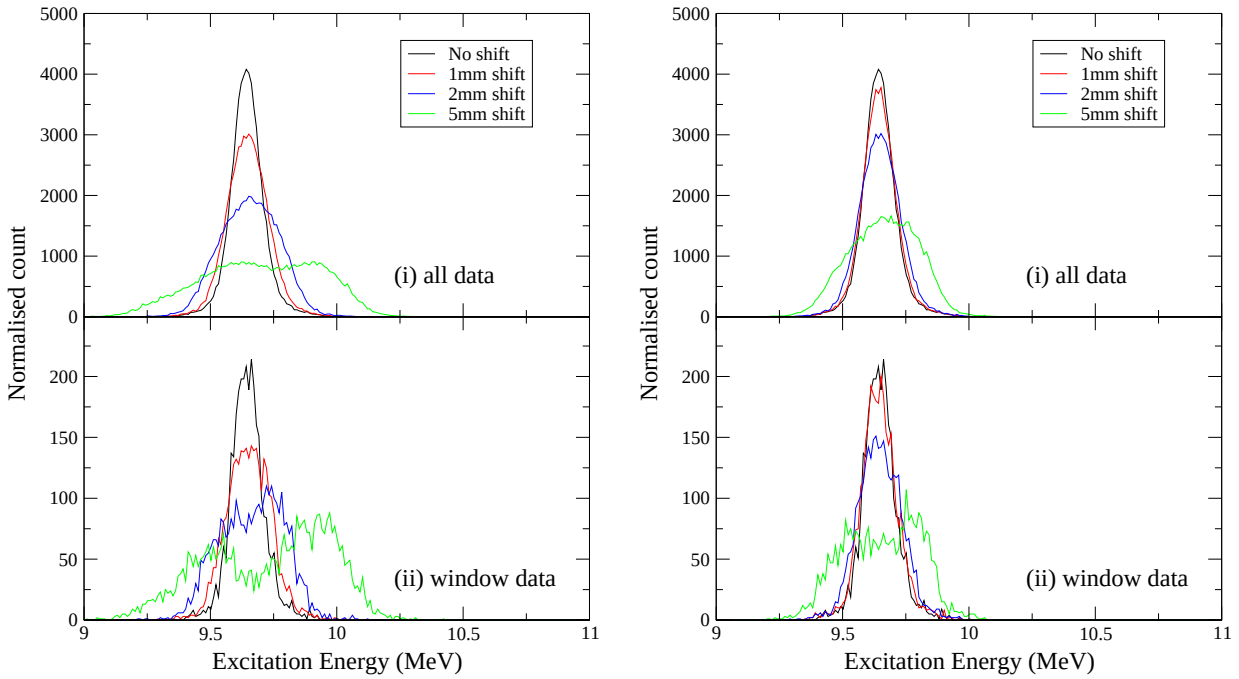

(a) Shift applied to singles telescope.

(b) Shift applied to doubles telescope.

Figure 4.26: Effect of introducing a linear shift to the position of a detector telescope in a direction perpendicular to the (RS detector) strips. The effect of introducing a shift is shown separately for moving (a) the singles telescope, and (b) the doubles telescope. The simulations suggest that the introduction of a rotational shift about the origin will affect the shape and position of the 3^- peak, and though the result is similar for both windows, it appears that it is accentuated in (ii) for both shifts, compared to (i).

In addition to shifts parallel to the (RS) strips, simulations were also performed to investigate the effect of an offset in a perpendicular direction. The results are shown in figure 4.26. Unlike for the 'parallel shifts', the result of a shift in a direction perpendicular to the RS strips appears to affect the 'window' spectra differently to the spectra for 'all the data'. It also appears that the effect is different for $2:1$ compared to $1:2$ coincidences. The simulations also imply that one effect of a perpendicular shift is a splitting of the 3^- peak, especially in the window data, which when employing the analysis techniques discussed earlier, could possibly be mistaken for an underlying energy level after normalising to the local peak area. This is perhaps more likely to mimic an erroneous 2^+ resonance at 9.7 MeV when there is only a slight offset in position, as the splitting would not be too severe.

normalising to the peak area will negate this.

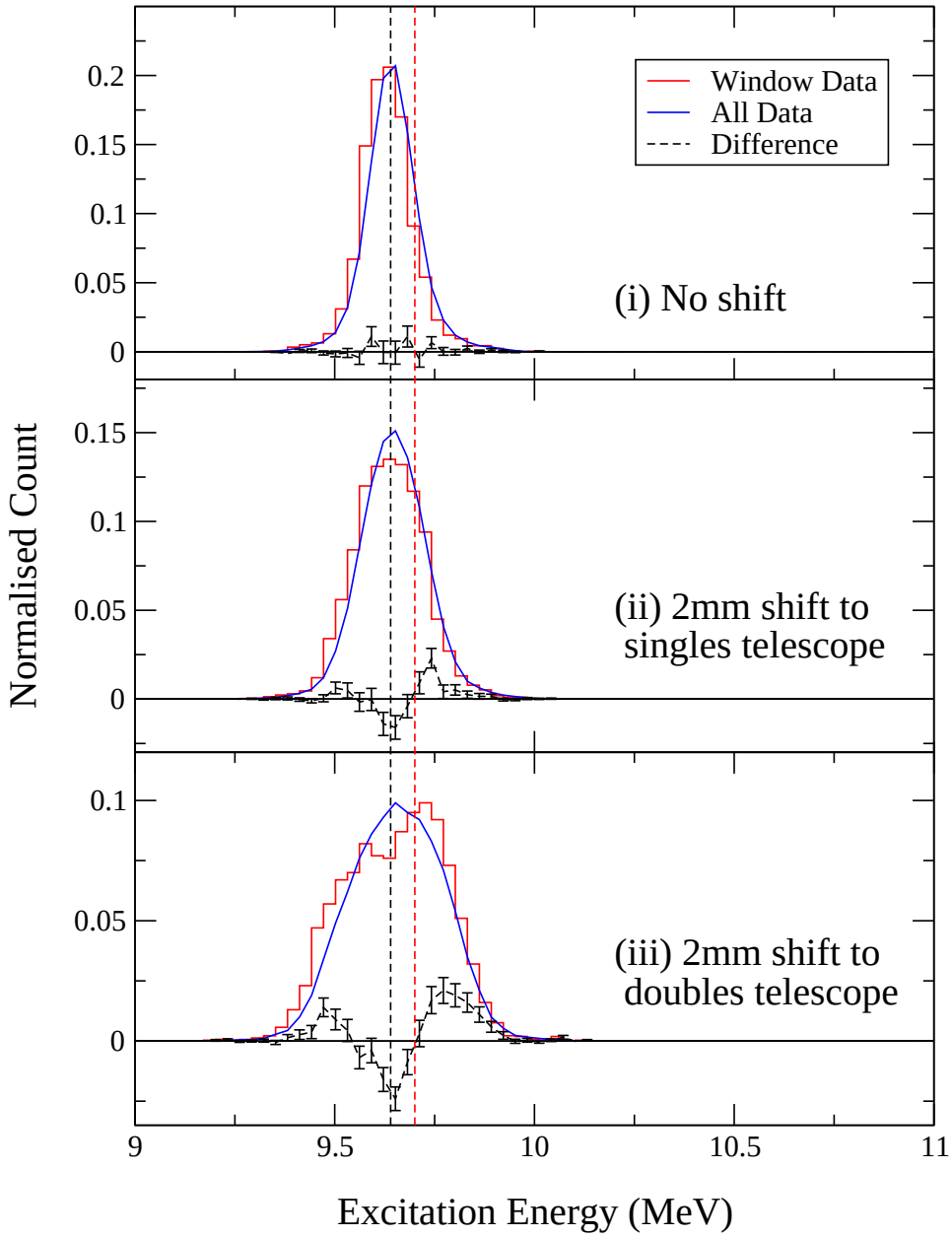

Figure 4.27: A more detailed analysis of the Monte Carlo simulations with a 2 mm shift introduced in a direction perpendicular to the detector strips. The black and red dashed lines correspond lie at 9.64 MeV and 9.70 MeV respectively. While there is some evidence of remainder in the difference between the 'window data' and 'all data' spectra when the shift is introduced in the singles telescope, there is a more noticeable splitting in the windowed-data peak when the shift is introduced in the doubles telescope (and far greater than any effects seen in the experimental data). Furthermore, there is no suggestion of a shift to the centroid position of the peaks in any cases.

When considering the case of a shift in the detector telescope position giving rise to the effects seen in the experimental data then it appears that a shift perpendicular to the direction of the detector strips is most likely. While a shift in a parallel direction does affect a simulated state (figures 4.24 and 4.25) by widening the peak and shifting the centroid position, these effects do not match those seen in the experimental data in which, most notably, there is no evidence of a shift in the centroid positions. Furthermore, the effects are very similar when the shift is introduced to both the singles and the doubles telescope; this suggests it unlikely to be responsible for the asymmetrical results seen in the experimental data. However, the effects seen in introducing a perpendicular shift (figures 4.26 and 4.27) suggest it is a good candidate to explain what is seen in the experimental data. There is clear evidence of a splitting in the 3^- peak when the shift is introduced into either telescope but with the strength of the effect exaggerated in the case of a shift in the doubles telescope; this would allow for the asymmetry seen in the experimental data. There is also importantly no evidence of a shift in the centroid positions which is again consistent with the experimental data. Although the extent of the perpendicular shift shown in figure 4.27 (2 mm) shows a peak splitting far in excess of that seen in the experimental data, the results do suggest a smaller shift (e.g. $\sim$1 mm), along with the background present in the experimental data, is a candidate to explain the effects seen.

4.4.2 Rotational shift offsets

An alternative possibility to an offset is that one of the telescopes may have been subject to a slight rotation in its mount. Without close inspection, this may appear similar to a shift in position and was hence also investigated as a possibility. Initial simulations were performed, which introduced a rotation around the beam spot, and, as previously, were performed for varying degrees of offset. The results of a rotation about the beam spot are shown in figure 4.28. Similar to the perpendicular shift, a rotation about the beam spot results in a splitting of the 3^- peak, and also appears more strongly in the 'window' spectra compared to the 'all data' spectra. However, unlike the simulations showing a perpendicular

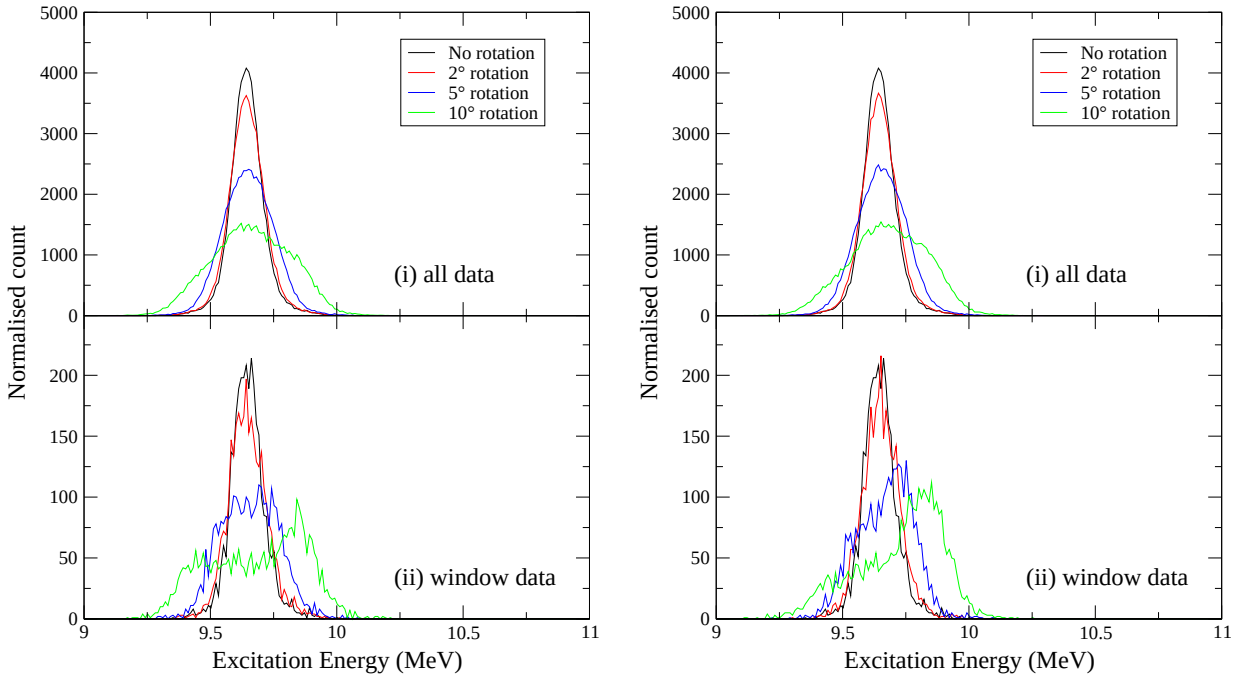

(a) Rotation applied to singles telescope.

(b) Rotation applied to doubles telescope.

Figure 4.28: Effect of introducing a rotational shift to the position of a detector telescope about the beam spot. The effect of introducing a rotation is shown separately for moving (a) the singles telescope, and (b) the doubles telescope. The simulations suggest that the introduction of a detector shift will affect the shape and position of the 3^- peak, and though the result is similar for both windows, it appears that it is accentuated in (ii) for both shifts, compared to (i).

shift, the difference in the the window/'all data' spectra seems more consistent, and hence is perhaps less likely to result in the azimuthal discrepancy seen in the experimental data.

An alternative rotation which can be considered is one about a point which lies on the detector (i.e. the individual detector's mount is twisted). In an attempt to investigate the possible repercussions of such a rotation, simulations were performed which rotated a telescope about three possible points:

1. the mid-point of the near side of the detector;
2. the middle of the detector;
3. the mid-point of the far side of the detector.

By considering three points it is possible to use any trends from a rotation about a point on the detector to understand the rotations about other points that were not simulated (the results are shown in figure 4.29). Once again, it is apparent that a rotation can result in a splitting of the 3^- state, though in this case it only occurs in the window data when the rotation is applied to the singles telescope; in all other cases it involves in a widening of the peak. Much like the perpendicular shifts, and also a rotation about the beam axis, there is no shift in the centroid position of the 3^- peak. All the effects are more pronounced as the point of rotation is moved further out from the beam spot.

4.4.3 Beam shift offsets

For completeness, Monte Carlo simulations were also performed to investigate the effect of offsetting the entire detector mount, i.e. effectively shifting the beam itself (this may be considered analogous to introducing a shift to both telescopes, in the same direction in the x- or y-plane). Figure 4.30 shows the effect of shifting the beam, relative to the both telescopes, in directions both parallel and perpendicular to the RS strips. As a shift to the beam-spot/mount position will always result in a shift to both the singles *and* doubles telescopes, figure 4.30 shows the result to the combined $2:1$ and $1:2$ ^{12}C spectra. Though the figures show a clear peak-splitting, and with only a small offset, the fact that both $2:1$

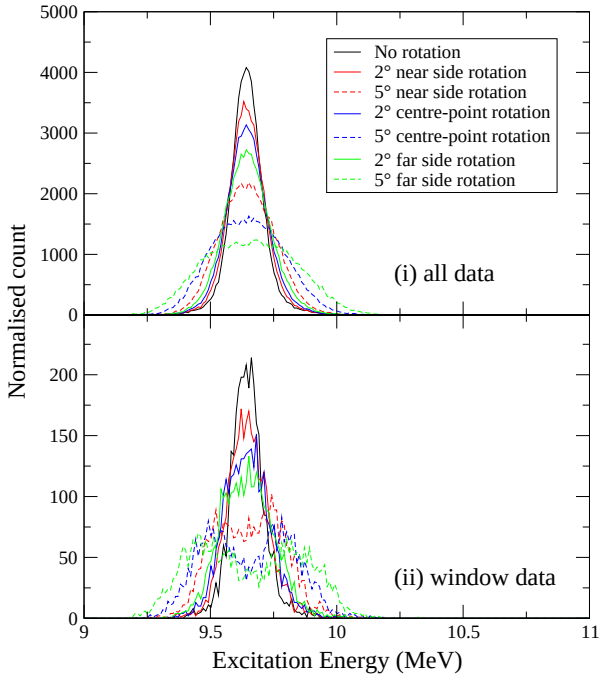

(a) Rotation applied to singles telescope.

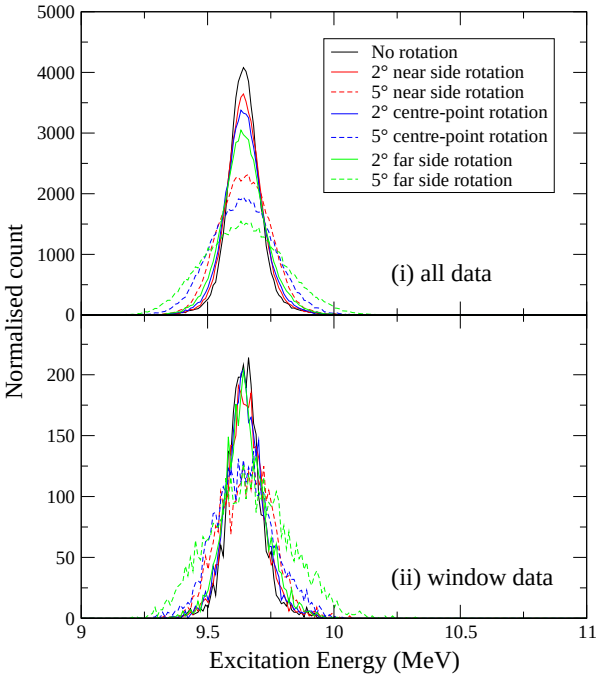

(b) Rotation applied to doubles telescope.

Figure 4.29: Effect of introducing a rotational shift to the position of a detector telescope about three points on the telescope. The effect of introducing a rotation is shown separately for moving (a) the singles telescope, and (b) the doubles telescope. The simulations suggest that the introduction of a rotation will affect the shape and position of the 3^- peak. While there is a clear peak splitting in the singles window data, this is the only spectrum in which it occurs. The rotations affect all the spectra and, as might be expected, a larger rotation results in a more pronounced effect. The further the point of rotation away from the beam spot, the more pronounced the effect.

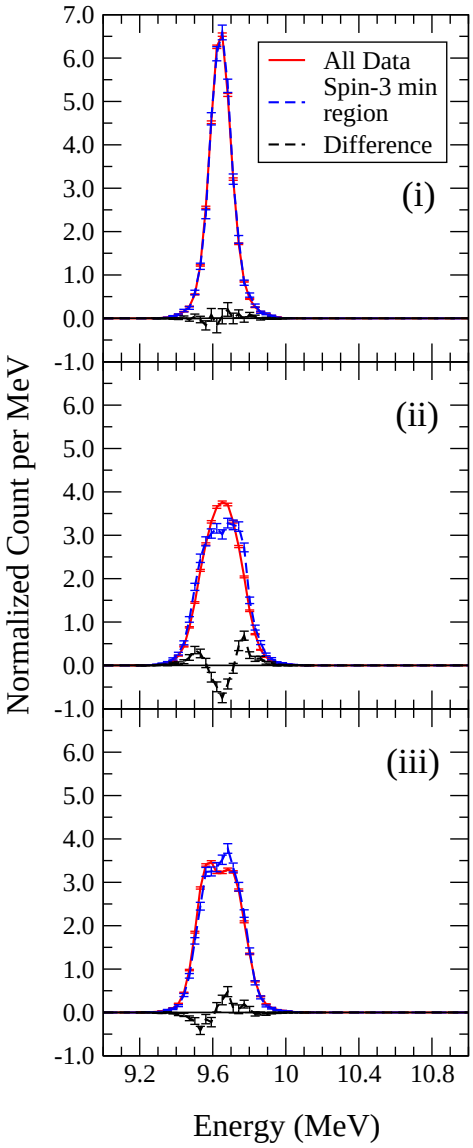

Figure 4.30: The effect of the beam not passing through the central axis of the detector array: (i) Monte Carlo simulation of a 3^- peak with the central axis, (ii) the same simulation as (i) but with the beam shifted 1 mm in a direction parallel to the RS strips, (iii) the same simulation as (i) but with the beam shifted 1 mm in a direction perpendicular to the RS strips.

and 1 : 2 coincidences will be affected suggest that neither a parallel, nor perpendicular, shift in the beam-spot position will explain the effects seen in the experimental data (figure 4.22).

4.4.4 Conclusions concerning offsets and rotations

From the various simulations performed it is believed that a perpendicular shift is the most likely candidate to explain the azimuthal asymmetry seen in figure 4.22, as these simulations were able to most closely recreate the features seen in the experimental data. Importantly, a perpendicular offset of $\sim$1 mm was noted to be present in the position of one of the RS-DSSD-CsI telescopes during the setting up of the experiment. The Monte Carlo simulations also highlight however that the data is sensitive to a number of possible shifts and that it is not possible to say with certainty which, if any, is responsible. It is indeed possible that the system is subject to a number of very small offsets of various types.

4.5 Applying a correction to the experimental data

In the same way that the various types of offsets were introduced into the Res8 Monte Carlo simulations via the analysis sort codes, a number of corrective terms were tested on the experimental data in an attempt to remedy the azimuthal asymmetry. For each correction applied, the ^{12}C excitation spectra for 1 : 2 and 2 : 1 coincidences (as seen in figure 4.22) were re-plotted. The values of the corrections were tuned so as to try and minimise the effects seen in figure 4.22a, whilst not introducing an equivalent artificial effect in figure 4.22b. Care was taken not to introduce shifts at levels which it was believed would have been noticed during the experimental set-up had they been present (i.e. greater than a $\sim$3 mm offset and/or a $\sim$3° rotation).

It was found that a good improvement in the asymmetry was possible by using a single correction: shifting telescope 4 by 2 mm perpendicular to the direction of the RS strips. The resulting ^{12}C excitation spectra for both the window and 'all data' regions, as well as the difference, are shown in figure 4.31.

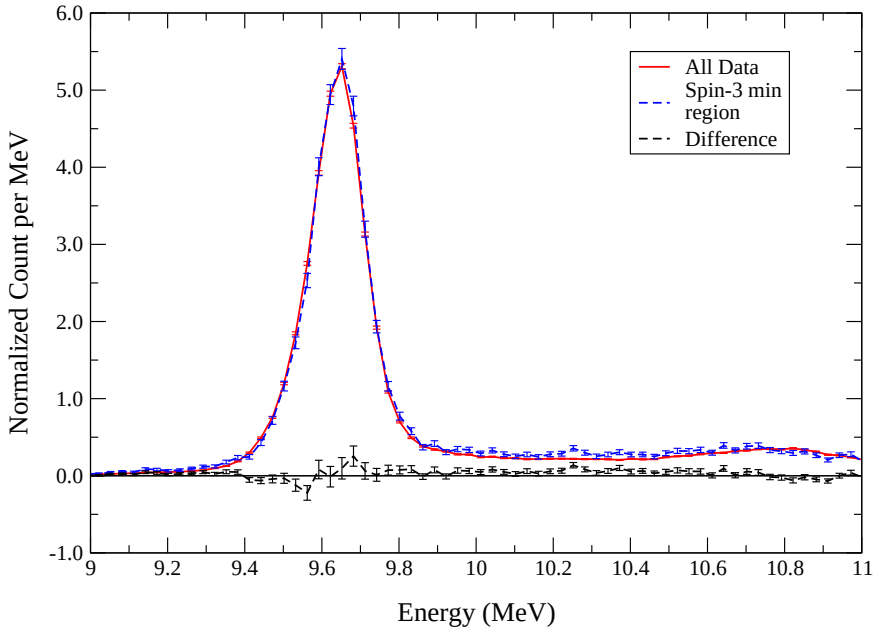

Figure 4.31: ^{12}C excitation energy spectra for different windows after an offset correction has been applied to telescope 4 (offset is 2 mm in a direction perpendicular to the RS strips). There is no evidence of any remaining structure when the normalised 'all data' and 'spin-3 min' peaks have been subtracted from one another. The separated 1 : 2 and 2 : 1 spectra are shown in figure 4.32.

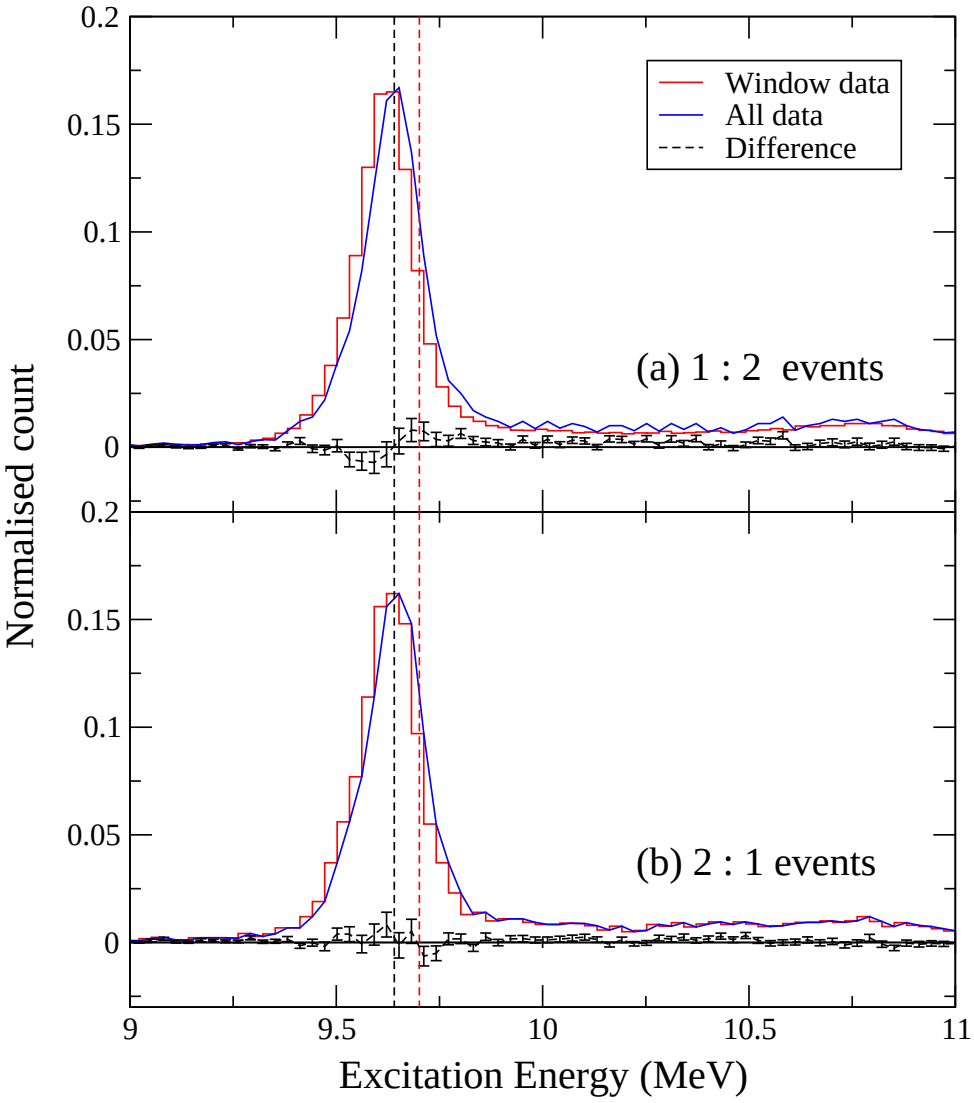

Figure 4.32: Differences in ^{12}C excitation energy spectra between regions of minimum and maximum 3^- contribution for (a) 1 : 2 events, and (b) 2 : 1 events *after a correction for a linear offset in the detector position has been applied*. The vertical dashed lines correspond to excitation energies of 9.64 MeV (black) and 9.7 MeV (red). The remainder seen in (a) in figure 4.22 has been somewhat corrected, whilst not introducing any significant artifacts into (b). The combined spectra is shown in figure 4.31.

4.5.1 Applying the fitting routine to the corrected spectrum

The fitting function previously used to create a 2^+ strength against window number plot (equation 4.7) can be re-written as[12]

$$f(E_x) = \frac{\alpha - \beta}{(\sigma_1 + \alpha\sigma_2)(\sigma_1 + \beta\sigma_2)} \left[-\sigma_2 \frac{\exp\left[-\left(\frac{E_x - c_1}{\sqrt{2}\sigma_1} \right)^2 \right]}{\sqrt{2\pi}} + \sigma_1 \frac{\exp\left[-\left(\frac{E_x - c_2}{\sqrt{2}\sigma_2} \right)^2 \right]}{\sqrt{2\pi}} \right] . \quad (4.9)$$

In the limit that $\alpha\sigma_2 \ll \sigma_1$ and $\beta\sigma_2 \ll \sigma_1$ then equation 4.9 can be approximated to be:

$$f(E_x) \simeq (\alpha - \beta) \frac{\sigma_2}{\sigma_1} \left[-\frac{\mathrm{e}^{-\left(\frac{E_x - c_1}{\sqrt{2}\sigma_1} \right)^2}}{\sqrt{2\pi}\sigma_1} + \frac{\mathrm{e}^{-\left(\frac{E_x - c_2}{\sqrt{2}\sigma_2} \right)^2}}{\sqrt{2\pi}\sigma_2} \right] . \quad (4.10)$$

This shows that the fitting function should have a bipolar form, with a negative-going component described by a Gaussian whose width is represented by that of the 3^- peak and amplitude by $(\alpha - \beta)\frac{\sigma_2}{\sigma_1}$, whilst the positive component is associated with a second Gaussian with a width determined by σ_2 and an amplitude identical to the first Gaussian.

Having introduced the offset correction term, the function described by equation 4.9 was fitted to the difference data shown in figure 4.31 to determine the strength of any possible 2^+ resonance in the data. However, unlike the routine used previously (in section 4.3.1), this time c_2 and σ_2 were also included, alongside β, as variables for the routine to use when optimising the fit. By exploring a range of input parameters to the routine, this produced values of $c_2 = 9.67{-}9.71$ MeV, $\sigma_2 = 32{-}83$ keV (FWHM $= 75{-}195$ keV) and $\beta - \alpha = -0.3\%$ to $+0.2\%$. The quantity $\beta - \alpha$ indicates the change in relative 2^+ and 3^- contributions for the selected regions; a value of zero indicates no additional contribution (and a negative value in fact indicates a negative 2^+ contribution).

It should be noted that the range of widths explored in the analysis contained within this thesis exceed the experimental resolution, and so the Gaussian line shape used is only an approximation to the resonance profile. This approximation is not believed to substantially

[12] Derivations of both equations 4.9 and 4.10 can be found in appendix C.

affect the conclusions.

4.6 Using Monte Carlo simulations to estimate the maximum resolvable contribution of a 2^+ resonance

Although the fitting routine used to distinguish a 2^+ resonance suggests there is little evidence for state at 9.7 MeV, further analysis can be performed to determine the maximum strength that a resonance could have should it exist and lie undetected. To better understand the previous result more precisely, Monte Carlo simulations were performed which replicated the 3^- resonance and background contributions as seen in the experimental data. These simulations were then used to explore the sensitivity of the current technique and the limits at which a 2^+ resonance might be detected.

In addition to the previously described $J^\pi = 3^-$ simulations, further simulations were performed to replicate the 10.84 MeV, 1^-, state; a smooth background was also generated. The simulations and background were combined such that the number of counts replicated those seen in the experimental data. A number of 2^+ simulations were also then performed that generated resonances of varying centroid positions (9.70 MeV, 9.85 MeV, and 10.0 MeV) and widths (FWHM = 250 keV, 500 keV, and 750 keV). Each 2^+ resonance was combined with the 3^-/background mix in a ratio of 15 : 85 (i.e. a 15% level). Similar calculations were also performed with 10%, 5% and 2% contributions from a 2^+ state. The parameters used to simulate the resonances were generally the same as those used previously (see table 4.1); those that were new/varied are shown in table 4.2.

The resulting angular correlations were processed in the same way as previously described for the experimental data, i.e. gating on window (ii) in figure 4.11b and window (iii) in figure 4.19), normalising the energy spectra and computing the difference. Using the same fitting routine as described by equation 4.9, a number of initial 'guess' parameters were passed to the fitting routine in order to probe the sensitivity of the fit, and by minimising the χ^2 value the optimal fit was obtained. For each combination of simulations it was determined whether the fitting routine was able to accurately distinguish the 2^+ resonance

Simulation parameter	Value
J^π	3^-
Excitation energy (E_x)	9.64 MeV
Width (Γ)	0.034 MeV
J^π	1^-
Excitation energy (E_x)	10.84 MeV
Width (Γ)	0.315 MeV
J^π	2^+
Excitation energy (E_x)	9.70, 9.85, 10.0 MeV
Width (Γ)	0.250, 0.500, 0.750 MeV

Table 4.2: Parameters used in the Monte-Carlo simulations of states in ^{12}C for determining the limits of the size of a possible undetected 2^+ resonance as a function of both excitation energy and width.

from the combined data − a successful fit was defined to be one in which the values returned by the routine matched the characteristics of the peak entered into the simulation. Two example MathCad sheets (used to apply the fitting routine to the simulations) are included in appendix D, showing both cases in which the 2^+ can and cannot be distinguished from the $3^-/1^-$/background mix.

At the 15% level the fitting routine was successfully able to distinguish the 2^+ from the background under all conditions. As the ratio was altered (to 10%, 5%, and 2%) to reduce the size of the 2^+ resonance, the fitting routine was eventually no longer able to verify its existence. For each mix the process of supplying the fitting routine with a variety of input parameters was repeated, using a χ^2 calculation to select the optimum values. This allowed a relationship to be found between the position/centroid and the strength of a resonance in order that it might be detected by the techniques employed in this analysis (table 4.3). Examples of some of the simulations and optimal fits are given in figure 4.33.

Table 4.3 indicates that for a 2^+ state well separated from the 9.64 MeV, 3^-, state (e.g. at 10.0 MeV and 250 keV width) it is possible to unambiguously pick out this contribution down to very low levels (2%). Larger contributions (15%) can be distinguished for all widths at all peak separations down to 60 keV. Unambiguous identification of the peak parameters becomes more difficult the smaller the separation from the 3^- state and the larger the width – as might be expected.

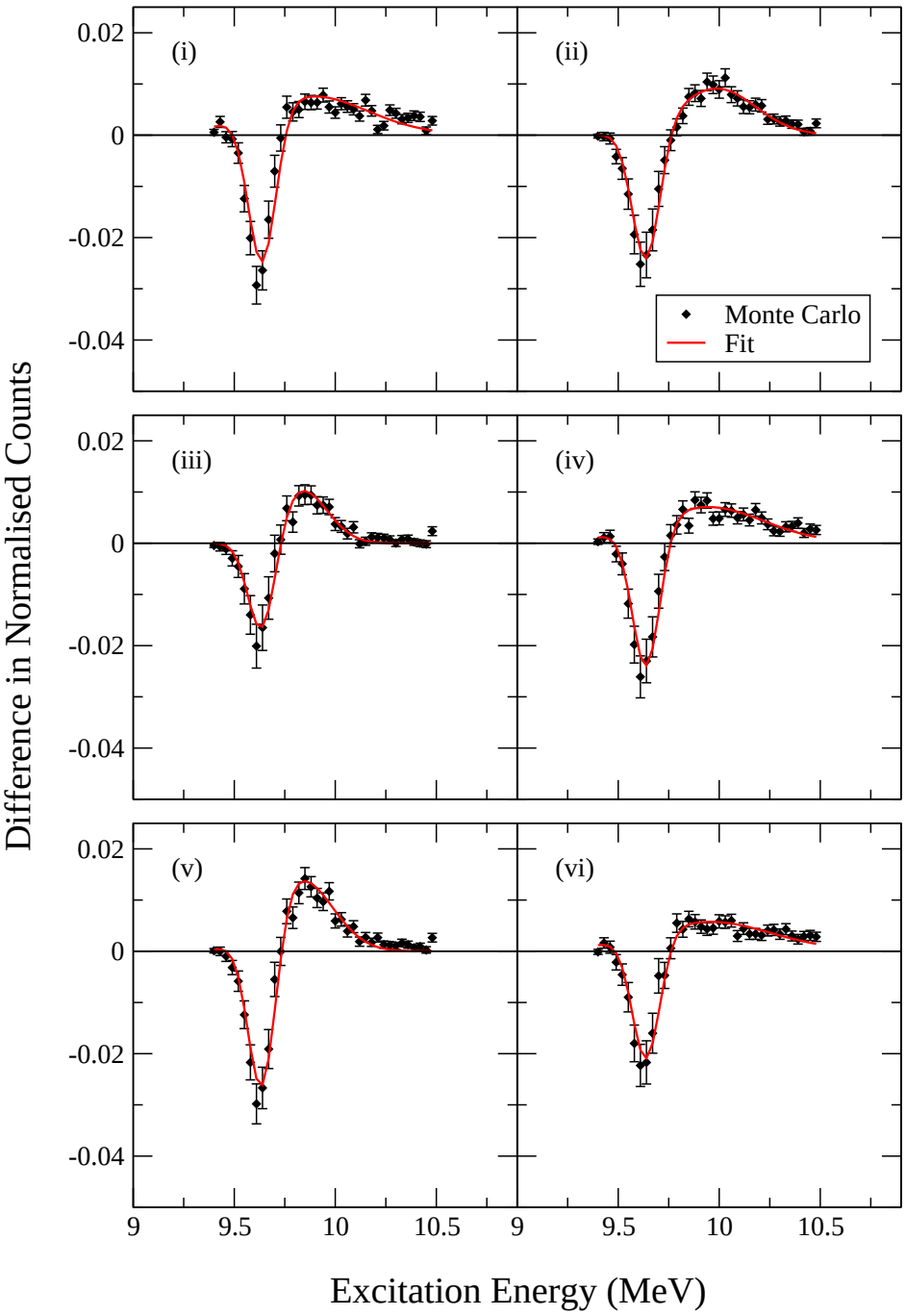

Figure 4.33: Spectra showing the Monte Carlo simulations, and optimised fits, for a variety of 2^+ resonances/contributions. (i), (ii) The effect of varying the centroid position of a 250 keV wide 2^+ resonance from 9.7 MeV to 10.0 MeV for a 10% 2^+ contribution; (iii), (iv) the effect of varying the width of a 2^+ resonance at 9.85 MeV from 250 keV to 750 keV, again for a 10% 2^+ contribution; (v), (vi) the difference between a 15% and 2% contribution of a 2^+ resonance at 9.85 MeV and 250 keV wide.

Resonance characteristics		Resonance resolved at			
Centroid (MeV)	Width (keV)	15%	10%	5%	2%
9.70	250	✓	×	×	×
	500	✓	×	×	×
	750	✓	×	×	×
9.85	250	✓	✓	×	×
	500	✓	×	×	×
	750	✓	×	×	×
10.0	250	✓	✓	✓	✓
	500	✓	✓	✓	×
	750	✓	✓	×	×

Table 4.3: Levels at which a resonance can be detected for various centroids and widths.

From this analysis it is possible to conclude that if an additional 2^+ resonance does exist in the present data and has a width of less than 250 keV, then it must have an excitation energy of less than 9.85 MeV and a population strength that is less than ∼10% of the 3^- peak. If the width lies in the 500 to 750 keV range then to be clearly identified it requires an excitation energy of ∼10 MeV and a population strength which is at least 5% of the 3^- peak. If it lies at a lower energy, much stronger strengths are required for unambiguous identification.

Chapter 5

Additional Analysis

In addition to the analysis described in the previous chapter, two further possibilities were investigated in attempts to find evidence of the 2_2^+ resonance; this chapter discusses both of these. Firstly, events not proceeding through the ground state in ^{8}Be are discussed, along with analysis of the reaction channels which proceed through these states. The findings are discussed along with statistical and analytical limitations which hinder analysis in this direction. The second part of this chapter discusses investigations into the possibility that the 2_2^+ resonance may lie at an energy significantly higher than the primary ($\sim$9.7 MeV) region investigated in the previous chapter.

5.1 Reaction channels involving decays through excited states in ^{8}Be

As discussed previously, the analysis contained in chapter 4 is from the

$$^{12}\mathrm{C}^* \longrightarrow {}^8\mathrm{Be}_{\mathrm{g.s.}} + \alpha$$

decay channel. Another channel which may be fed by the decay of a 2^+ resonance in ^{12}C is the

$$^{12}\mathrm{C}^* \longrightarrow {}^{8}\mathrm{Be}^* + \alpha$$

decay channel. The first excited state in ^{8}Be is perhaps a good candidate for a state through which the 2^+ excitation of the Hoyle state will be populated, as it also has $J^\pi = 2^+$, allowing the decay to proceed via an $l = 0$ emission, and hence with a reduced decay barrier.

5.1.1 Statistical considerations

In order to select this reaction channel it was necessary to re-examine the ^{8}Be excitation energy spectrum used in chapter 4 (figures 4.4 and 4.10). Following the analysis contained in chapter 4, it was possible to remove almost all those counts which could be considered artifacts of the analysis from the ^{8}Be excitation energy spectrum. Figure 5.1 shows both the initial spectrum and the same spectrum with all incorrect $\alpha - \alpha$ pairings removed, as well as some previous double counting of events occurring at the earlier stages of the analysis (the latter of these spectra also confirms that the double peak feature seen at $\sim 1.5 - 2.0$ MeV in all earlier ^{8}Be excitation energy spectra is indeed a result of incorrect $\alpha - \alpha$ pairings and is not a 'real' feature). The dotted line on the plot signifies the upper limit of the gate previously used to select only events proceeding through the $^8\mathrm{Be}_{\mathrm{g.s.}}$. By selecting events in which no pair of α-particles had an excitation energy lying in (or below) the low-energy peak (figure 5.1), it was possible to discard these events and select only events proceeding through excited states in ^{8}Be

Though statistically poor, a ^{12}C excitation energy spectrum can be produced for ^{8}Be* events; this is shown in figure 5.2. In addition to the 9.64 MeV 3^- peak, the locations of several other known states in ^{12}C are marked and though there is some evidence that these states are being populated, the background is considerable. In addition to the 2 : 1 and 3 : 0 hit configurations discussed in chapter 4, statistics can be significantly increased (and to a greater extent at higher energy) by also including 1 : 1 : 1 events (i.e. events in which all

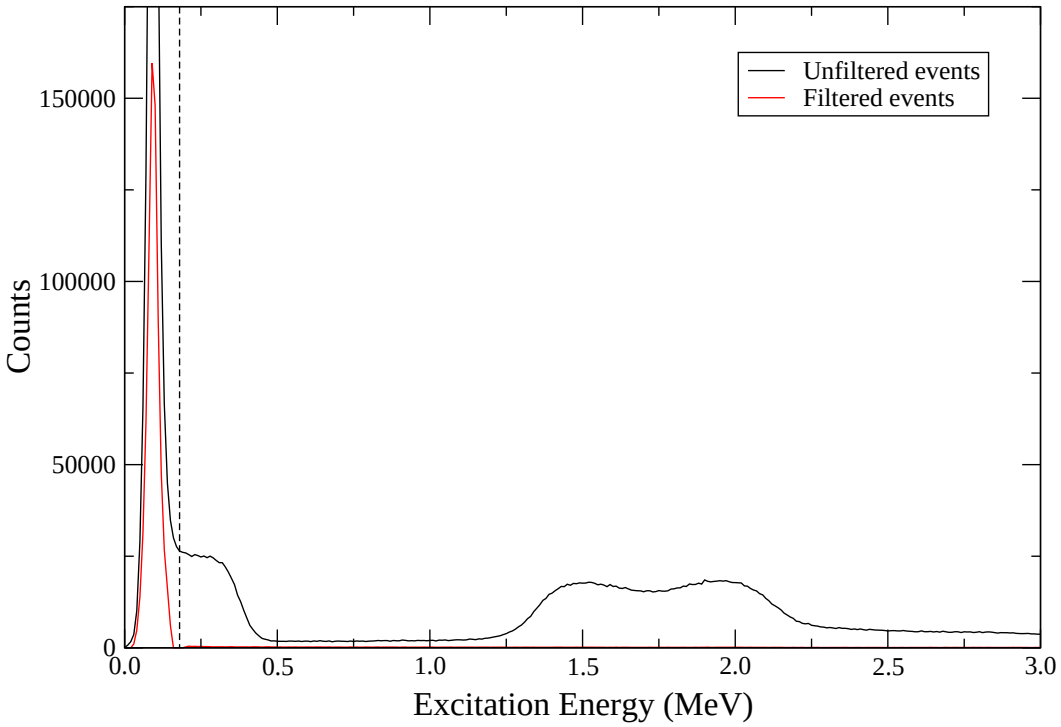

Figure 5.1: ^{8}Be excitation energy spectra for all $2:1$ and $3:0$ events, and also for events filtered to remove any incorrect $\alpha-\alpha$ pairings. The high energy shoulder on the ground state peak, as well as the double-peak structure at $1.5-2.0$ MeV, disappear when the incorrect $\alpha-\alpha$ pairings are removed, confirming that both are artifacts of an earlier sort-code.

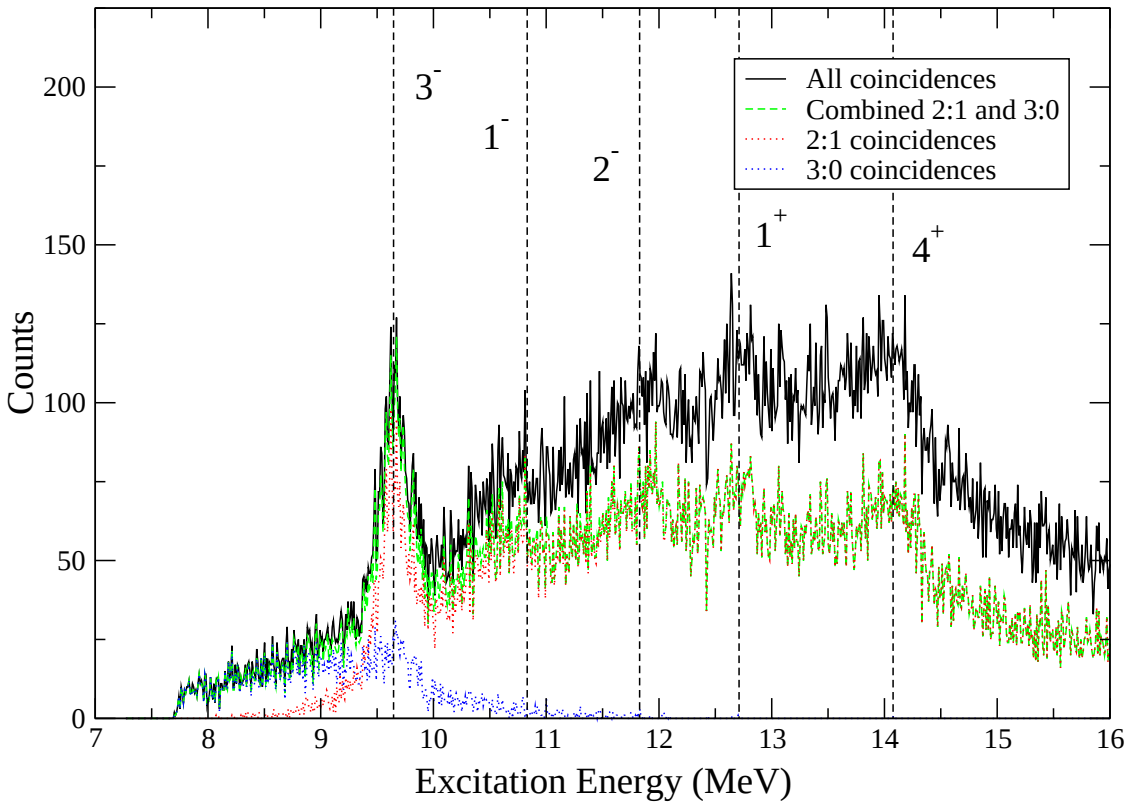

Figure 5.2: ^{12}C excitation energy spectrum for decays *not* through the ^{8}Be ground state. The red and blue dotted lines show the separate contributions of $2:1$ (and $1:2$) and $3:0$ (and $0:3$) hit configurations respectively, and the dashed green line is the sum of the two contributions. The solid black line also includes events in which each particle is incident on a different telescope. Four known states in the energy region have also been marked: the 3^- at 9.65 MeV, the 2^- at 11.83 MeV, the 1^+ at 12.71 MeV, and the 4^+ at 14.08 MeV.

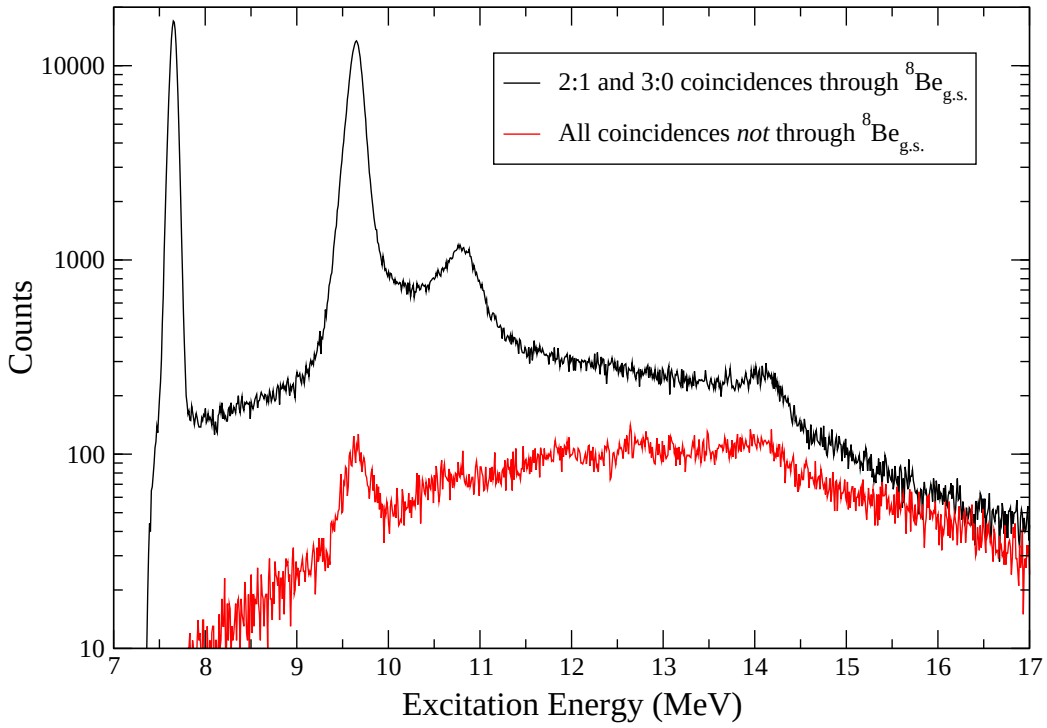

Figure 5.3: ^{12}C excitation energy spectra for 2 : 1 and 3 : 0 decays through the ^{8}Be ground state, and also for all events through the excited states in ^{8}Be. While the statistics for decays through excited states in ^{8}Be are notably poorer than those through the $^{8}Be_{g.s.}$ for all energies, the relative strength of $^{8}Be^{*}$ decays to $^{8}Be_{g.s.}$ decays increases with excitation energy.

three α-particles are deposited in separate telescopes); this can be seen from their inclusion in the 'All coincidences' data shown in figure 5.2.

Figure 5.3 shows the ^{12}C excitation energy spectrum for both $^{8}Be^{*}$ events, and also 2 : 1 and 3 : 0 events proceeding through the $^{8}Be_{g.s.}$, and reveals the statistical limitations of investigating ^{12}C using the $^{8}Be^{*}$ decay channel. The figure also confirms that at higher energy, as seen in figure 5.2, the number of counts from $^{8}Be^{*}$ events increases relative to the number of counts from $^{8}Be_{g.s.}$ events.

5.1.2 Angular correlations for decay to non spin-zero states

In addition to the low statistics, there exists a further difficulty in investigating the ^{8}Be* decay channel. One of the primary analytical tools used in the analysis contained within chapter 4 of this thesis are angular correlation plots. As discussed in appendix A, since the reaction proceeds through a definite intermediate state (the ^{12}C*), then it can be represented by two transition amplitudes, $\mathrm{T}^{\mathrm{m_a m_A}}_{\mathrm{m_b m_B}}$ and $\mathrm{T}^{\mathrm{m_{B^*}}}_{\mathrm{m_c m_C}}$, a formation transition amplitude and a decay transition amplitude (both of the ^{12}C*) respectively. The angular correlations technique requires that the decay amplitude can then be replaced by spherical harmonics:

$$\mathrm{T}^{\mathrm{m_{B^*}}}_{\mathrm{m_c m_C}} \propto \mathrm{Y}_{\mathrm{J_{B^*}\, m_{B^*}}} \left(\Omega_{\psi}\right) .$$

However, this substitution can only be made if the final decay products are formed in spin-zero states, i.e. $\mathrm{T}^{\mathrm{m_{B^*}}}_{\mathrm{m_c m_C}} \longrightarrow \mathrm{T}^{\mathrm{m_{B^*}}}_{0\,0}$. This means that in order to investigate the 9.7 MeV region through the ^{8}Be* reaction channel, a different technique to the angular correlation plots must be found in order to suppress the (still) dominant 3^{-} state.

5.1.3 Conclusions regarding the $^{12}\mathrm{C}^{*} \longrightarrow {}^{8}\mathrm{Be}^{*} + \alpha$ decay channel(s)

As discussed, tentative attempts were made to investigate the feasibility of using the $^{12}\mathrm{C}^{*} \longrightarrow {}^{8}\mathrm{Be}^{*} + \alpha$ decay channel to look for the 2^{+} excitation of the Hoyle state. Whilst a possible decay channel in which the 2^{+}_{2} resonance may be observed, it is clear that there is low experimental sensitivity. Given the statistics available, and following the analysis carried out in chapter 4, it would be necessary for the strength of the 2^{+}_{2} resonance (relative to the 3^{-}) to be *at least* an order of magnitude larger in this reaction channel for any trace of a resonance to be present (even without considering the substantially larger background present in this reaction channel). In addition to the poor statistics, problems arise with the analytical tools available. By proceeding through a state with non-zero spin, the angular correlations technique used in the present analysis is no longer applicable. In order to suppress the still dominant 3^{-} state (figure 5.2) it is clear a new approach must be found.

5.2 Investigating the possibility of 2_2^+ strength at higher excitation energies

Recent R-matrix analysis of the β decays of ^{12}N and ^{12}B has led to the suggestion that the 2_2^+ resonance may lie at a significantly higher energy than 9.7 MeV [62]. Analysis of two experiments, resulting in sequential α-decay through states in ^{8}Be, suggested that the 2_2^+ may in fact lie at an energy in the region of $10.5 - 12$ MeV. Though the data set analysed within this thesis is statistically poor towards the upper limit of this range, further analysis was performed to investigate the lower end of the energy range, specifically the area between the 9.64 MeV, 3^-, peak and the 10.84 MeV, 1^-, peak. In the case that the 2_2^+ resonance lies at the upper end of the $10.5 - 12$ range, it is hoped that evidence of its existence might be found in the form a low-energy tail in the region between the 9.64 MeV and 10.84 MeV peaks. Furthermore, it has been suggested that the 2_2^+ resonance may also exist as a broad state at a lower energy (9.6 MeV) [45]. If this is case then the region between the 9.64 MeV, 3^-, peak and the 10.84 MeV, 1^-, peak is also a good candidate region to find evidence of a high-energy tail. As this region of the ^{12}C excitation energy spectrum is not dominated by a single state, but likely by a combination of the aforementioned peaks, a different approach was taken to that described in chapter 4.

The region of interest was divided into three smaller subsections, each covering an equal energy range (see figure 5.4), and angular correlation plots were created for each. These angular correlation plots were then projected, along with the 9.64 MeV (3^-) and 10.84 MeV (1^-) peaks, onto the $\theta^* = 0$, ψ-axis, at a variety of projection angles. Figure 5.5 shows the (normalised) effect of projecting an angular correlation spectrum (for window II, figure 5.4) onto axes at a variety of angles, including those for the angles associated with ridges of 3^- and 1^- states (171.1° and 177.3° respectively). As the projection angle increases, so too does the number of channels which the projection spans, as well as the difference between the central minimum and its neighbouring maxima.

Assuming that there is no 2^+ resonance in the windowed region, then it should be possible

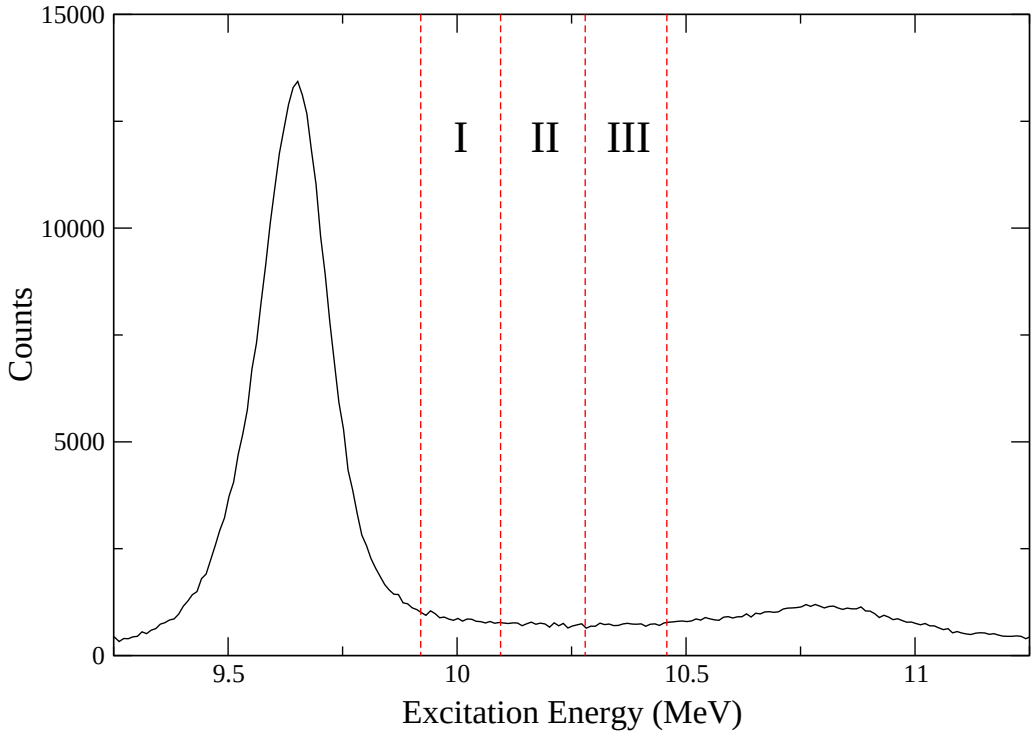

Figure 5.4: ^{12}C excitation energy spectrum showing the windows used for analysing the possibility that the 2_2^+ resonance may lie at a higher energy than the 9.7 MeV region. The windows each span 180 keV, the red dashed lines bounding the regions lying at 9.922, 10.102, 10.282 and 10.462 MeV. The peaks at either side of the regions are the 9.64 MeV, 3^-, and 10.84 MeV, 1^-, states respectively.

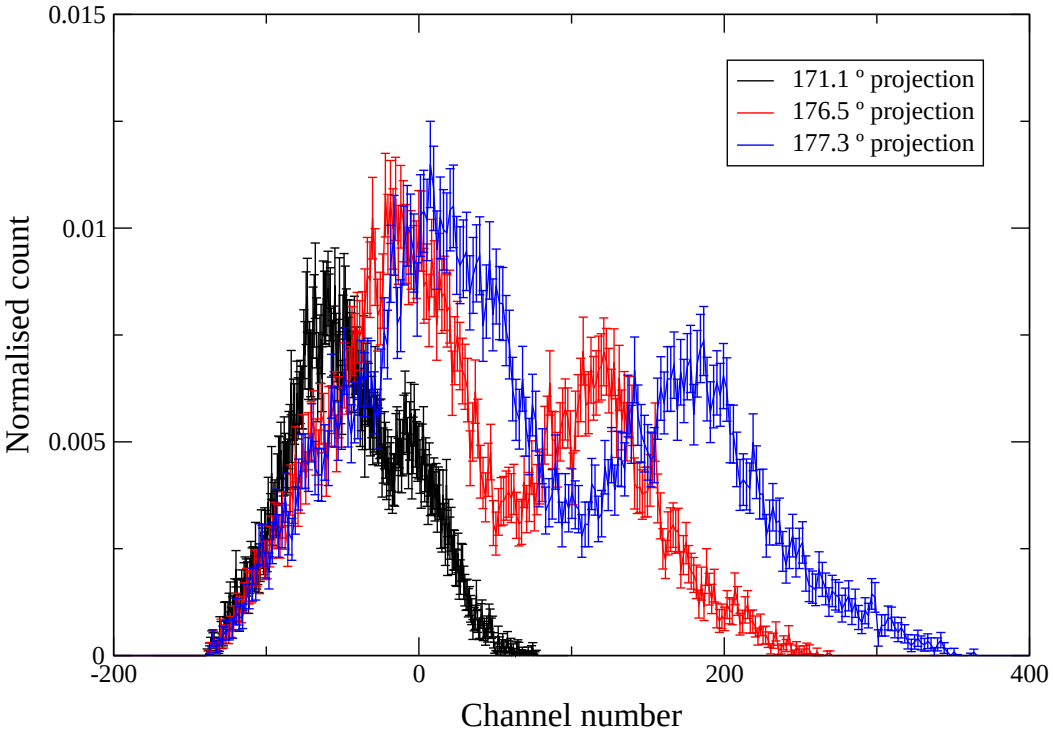

Figure 5.5: Ridge structure of the angular correlations (for window II, figure 5.4) projected at a range of angles. The 171.1° and 177.3° projections are for the theoretical angles for the ridges of a 3^- and 1^- state respectively (as calculated using equation 4.6). The most important feature of increasing the projection angle is the increase in the difference between the central minimum relative to its neighbouring maxima.

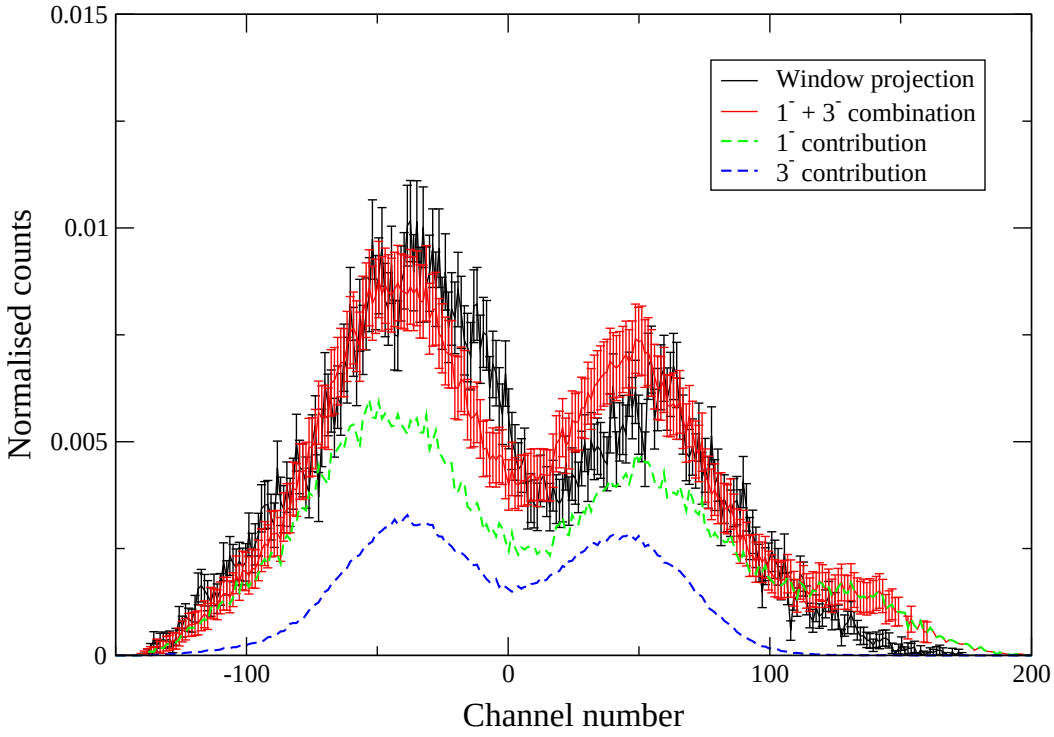

Figure 5.6: An example of the optimised fit to the window (II) data for angular correlation ridges projected at 175.0° using a combination of the projected spectra for the 3^- and 1^- peaks. The $3^- + 1^-$ fit is 31% of the normalised 3^- projection and 71% of the normalised 1^- projection.

to recreate the projection from the intermediate spectrum using a combination of those from the 3^- and 1^- peaks[1]). A simple fitting routine was used to optimise the fit of the combined $3^- + 1^-$ spectrum to the projected spectrum of windows I, II and III. This was done by varying the contributions of each of the (normalised) 3^- and 1^- and subtracting the combined spectrum from that of the window being investigated. A wide range of $3^- + 1^-$ values were tried and the optimal fit deemed to be that for which the square of the differences between the two spectra was minimized. An example of an optimised fit, along with the separate 3^- and 1^- components from which it is constructed, is shown in figure 5.6.

[1]The inclusion of a (approximately) constant background contribution could also be considered in the calculations but has been omitted in the analysis contained within this thesis. In addition, there is a broad (0^+) state known to exist in the region of interest, though its contribution is believed to be minimal and is also isotropic in ψ.

Although the angle at which the projections are performed is in theory an arbitrary selection[2], careful selection allows significantly increased sensitivity[3] in the region of interest (as shown in figure 5.5). Figures 5.7 and 5.8 show the optimised fits for all windows for two different projection angles, 177.3° and 171.1° respectively. These angles have been selected as they are the angles at which the ridges of a 1^- and 3^- state are calculated to lie. As might be expected from the results shown in figure 5.5, the sensitivity available to optimise the fit is increased at a projection angle of 177.3° (compared to the 171.1°, 3^- angle). In both figures 5.7 and 5.8 the $3^- + 1^-$ fit is unable to accurately recreate the windows' projections for all three windows, with an remainder structure present at approximately the same location in both sets of spectra (channel number $\simeq 75$ in figure 5.7 and $\simeq -45$ in figure 5.8). It is not possible to confirm whether this is a signature of a 2^+ resonance, and due to complications arising at projection angles close to 0° (or equivalently 180°) [53], the previous approach of utilising Monte Carlo simulations to help predict the expected behaviour of a 2^+ resonance offers only limited assistance.

Though it only offers an approximate indication of the location of a 2^+ state, the process was nonetheless repeated for a series of Monte Carlo simulations. The angular correlation projections for projection angle of 171.1° are shown in figure 5.9. Unlike for the experimental data, due the absence of any distorting effects at projection angles close to 180°, a good level of sensitivity is achievable. This suggests that though Monte Carlo simulations may be used to predict where the contribution of a $J^\pi = 2^+$ state would be strongest, the approach is, as expected, limited in its capability to replicate features seen in the experimental data. In order to use the simulations to more accurately replicate the results seen in the experimental analysis, the inclusion, and the associated effects, of the spin of a state must be integrated into the Monte Carlo simulations in a more sophisticated manner.

The work of Hyldegaard *et al.* [62] suggests that there may be evidence of the 2_2^+ resonance in the $10.5-12$ MeV region, it has not been possible to confirm nor refute the existence of such

[2]i.e. if the window projection is indeed a mixture of 3^- and 1^- then it should be possible to successfully replicate the spectrum using the constructed $3^- + 1^-$ at any projection angle.

[3]The 'sensitivity' being the difference between the maxima and central minimum of the peaks.

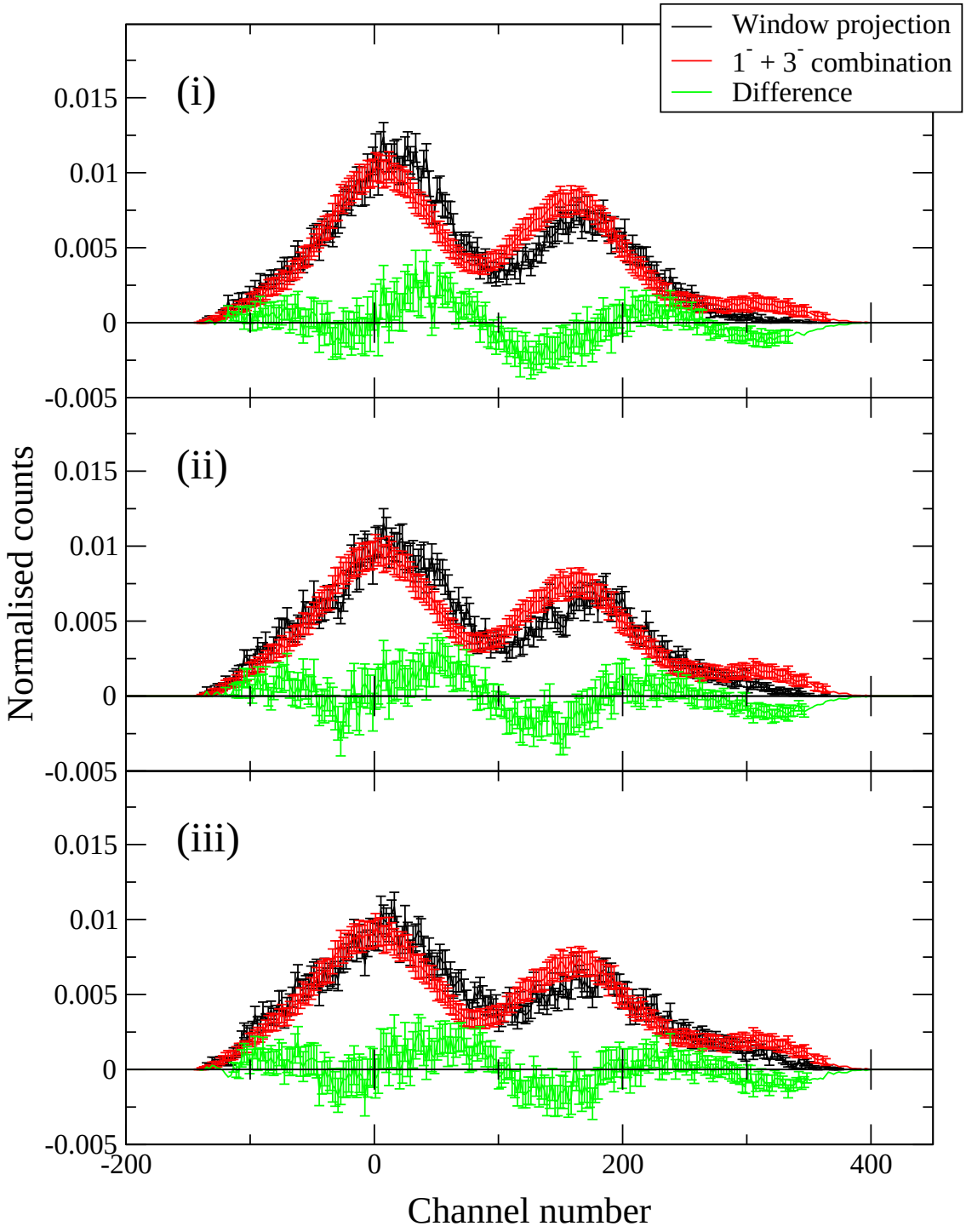

Figure 5.7: Angular correlation ridges projected at 177.3° for all intermediate windows, the optimised $3^- + 1^-$ reconstructions, and the difference between the two. When the fit is subtracted from the windowed projection a remainder is noticeable in all three spectra, becoming progressively weaker from window I through to window III. A projection angle of 177.3° is the angle at which the ridges of a 1^- state are calculated to lie.

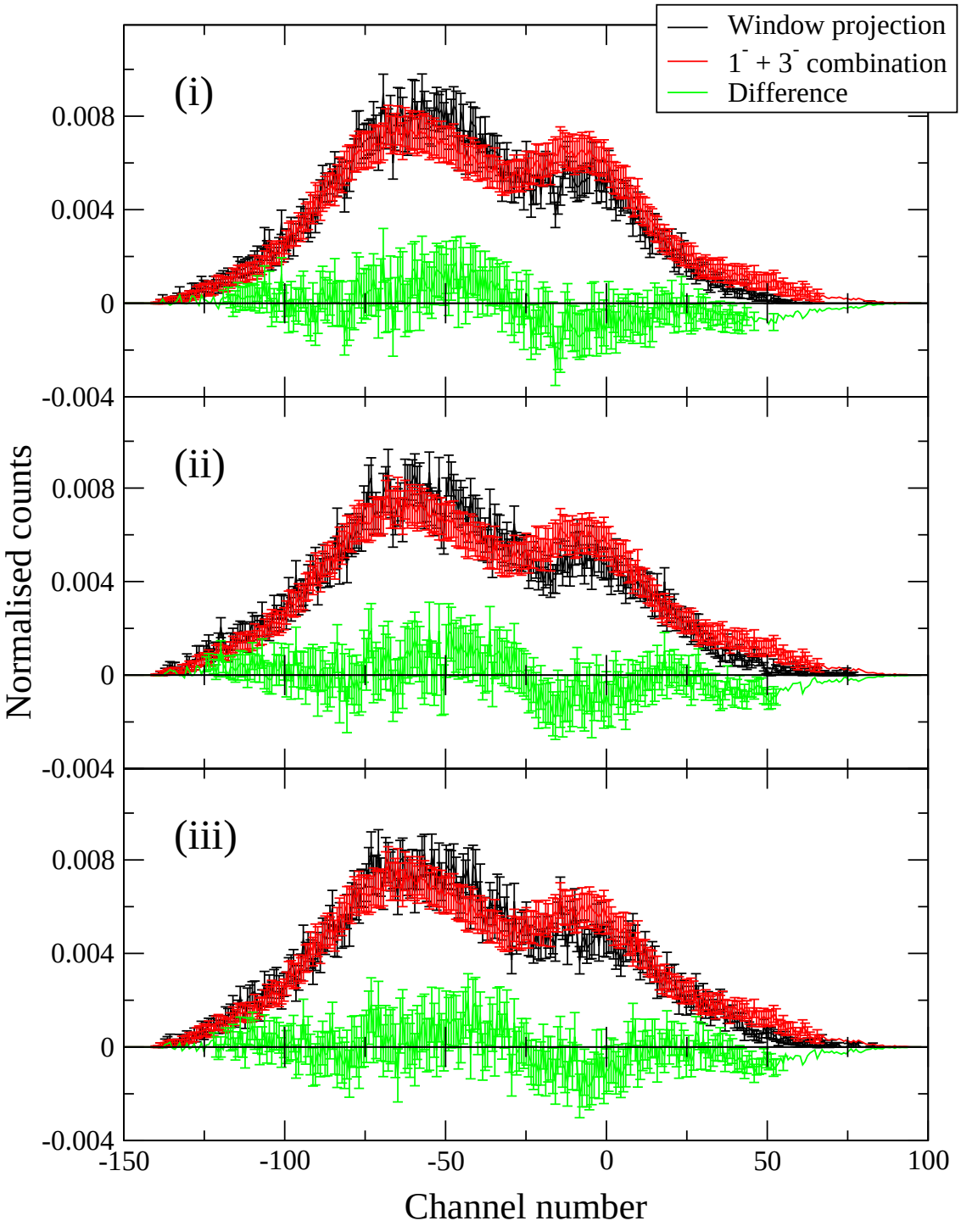

Figure 5.8: Angular correlation ridges projected at 171.1° for all intermediate windows, the optimised $3^- + 1^-$ reconstructions, and the difference between the two. As in figure 5.7, a remainder can be seen in the difference between the projections and optimal fits for all three windows, again becoming progressively weaker from window I through to window III. It is apparent however that the decreased sensitivity at 171.1° makes it harder to clearly identify. A projection angle of 171.1° is the angle at which the ridges of a 3^- state are calculated to lie.

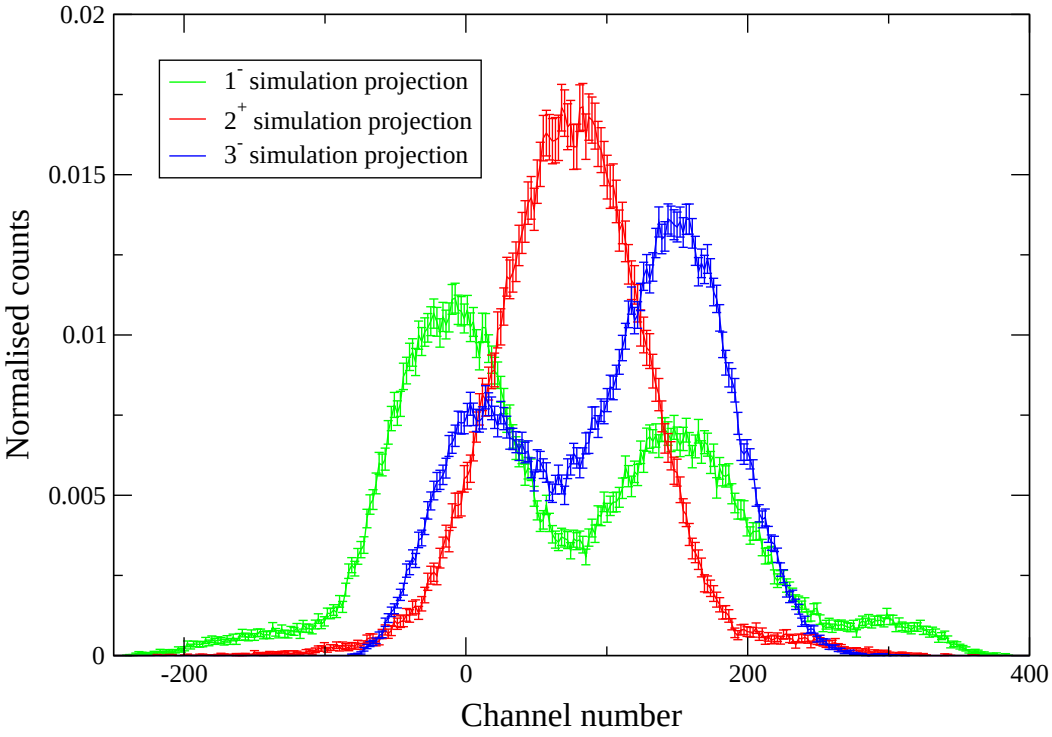

Figure 5.9: Angular correlation ridges projected at 171.1° for Monte Carlo simulations of 1^-, 2^+ and 3^- states. Though the relative positions of the 3^- and 1^- peaks appear similar to those seen in the experimental data, the greatly increased sensitivity predicted by the simulations at the given projection angle suggest that their ability to replicate the experimental data is somewhat limited.

a state in the given region. Though an unexplained structure has indeed been discovered, further analysis is required in order to ascertain whether it is indeed a signature of a 2^+ resonance or not. It is perhaps important to note that the work presented in [62] required the inclusion of decays through excited states in ^{8}Be in order to justify the inclusion of a 2^+ resonance in the calculations. A previous R-matrix analysis also using β-decay from ^{12}N and ^{12}B to populate states in ^{12}C, and also studying sequential α-decay, but *not* including decay channels through excited states in ^{8}Be [63], failed to find any evidence of the 2_2^+ state. However it should also be noted that, for the analysis contained in [62], the reaction being studied involved the β-decay of ^{12}N and ^{12}B into states in ^{12}C, which may result in states being populated quite differently to the data set analysed in this thesis.

Though the work carried out by Hyldegaard *et al.* suggests that the $10.5-12$ MeV region is a good region to investigate in the search for the 2_2^+ excitation of the Hoyle state, the analysis contained within this section cannot confirm nor deny that such a resonance exists. A development of the Monte Carlo simulations used for the present analysis may allow the behaviour of a 2^+ resonance to be better predicted. That the analysis in [62] requires the inclusion of reaction channels through excited states in ^{8}Be, it would perhaps be preferable to include such data (and also preferably with increased statistics) in using the methods contained within this thesis to perform a more complete analysis of the aforementioned energy region. However, problems associated with analysing such reaction channels (discussed in chapter 5.1 of this thesis) may cause problems in any attempts to do so.

Chapter 6

Summary

A search has been made for the 2_2^+ excitation of the 7.65 MeV, 0_2^+, Hoyle state in ^{12}C using the ^{12}C(^{12}C,^{12}C[3α])^{12}C reaction. Previous work carried out by Itoh *et al.* [44] suggested the signature of a 2^+ resonance in the region ^{12}C excitation energy spectrum slightly above the 9.64 MeV, 3^-, state and directed the prime energy region of interest for the work contained within this thesis.

An angular correlations technique was used in to suppress the dominant 9.64 MeV, 3^-, peak and enhance any signature of a 2^+ resonance in the energy spectrum. Though the measurements failed to find any evidence of a new resonance in the 9.7 MeV energy region it is not possible to confirm that a state does not exist. In order to provide more stringent limits to the conclusions drawn from the current work, increased experimental sensitivity would be required. The large energy resolution of the experimental setup result in difficulties in resolving a peak so close in energy to the dominant 9.64 MeV state. Increased angular resolution would also allow improved resolution of the minima/maxima in the angular correlation spectra, in turn allowing the contribution of a 2^+ resonance to be increased relative to the 3^- peak.

Monte Carlo simulations were used in an attempt to understand these results more precisely. By simulating 2^+ resonances with a variety of centroid positions, widths and strengths (relative to the 3^- peak), the sensitivity of the experimental setup was investigated. This

allowed limits to be put on the possible strength of an undetected resonance, depending on its characteristics. This is discussed in detail in chapter 4.6. The Monte Carlo simulations were also used to investigate an apparent aberration in the azimuthal symmetry of the experimental results, allowing various physical offsets in the detector setups to be simulated and investigated as possible causes of the splitting of the 9.64 MeV, 3^-, peak observed (discussed in chapter 4). It was found that the peak splitting seen is indeed consistent with that expected for a physical offset in the position of a detector telescope within the experimental setup.

A more recent R-matrix analysis of the decay of ^{12}N and ^{12}B, carried out by Hyldegaard *et al.* [62], suggests that the 2_2^+ excitation may in fact lie at an energy in the $10.5 - 12$ MeV region. Further analysis of this energy range specifically focussed on the region between the aforementioned 9.64 MeV state and the 10.84 MeV, 1^-, state. This was done by extending the angular correlations technique employed in the previous analysis. Though the analysis did find a structure within the data - indicating a further contribution to the spectrum, it was not possible to confirm, nor dismiss, the possibility that this was a signature of a 2^+ resonance. Due to limitations at the required projection angles of the angular correlations, the Monte Carlo technique used previously to investigate experimental sensitivity was severely limited in this analysis. It is also important to note that the work of Hyldegaard *et al.* required that decays through excited states in ^{8}Be be included in order for a 2^+ resonance to exist in the $10.5 - 12$ MeV region. The inclusion of decays through states in ^{8}Be for which $J \neq 0$ renders the angular correlations technique, used extensively in earlier analysis, unusable and hence requires a new approach in order to suppress the otherwise dominant 3^- and 1^- contributions.

6.1 Significance of the results in relation to other work

Having been initially directed to the $\sim$10 MeV region by the experimental analysis carried out by Itoh *et al.* [44], no evidence has been found supporting the existence of a 2^+ resonance in this region. Following a ^{12}C(p,p')^{12}C experiment carried out by Freer *et al.* [45], which found

evidence of a broad (∼600 keV) 2^+ resonance in the 9.64 MeV region, similar parameters to those found were tried in the fitting routine discussed in chapter 4. The result of forcing the fitting routine to this predicted peak shape resulted in no evidence suggesting the existence of a resonance in the experimental data. It is important to note however that with the resolution of the analysis contained in this thesis (∼300 keV) it would be difficult to resolve a broad state lying at 9.6 MeV from the 9,64 MeV, 3^-, peak; this is confirmed by the Monte Carlo analysis contained in section 4.6. Though the earlier work of Fynbo *et al.* [43] also found no evidence of a 2^+ resonance in the region being investigated, it is important to note that this was done using a considerably different reaction channel, and hence the ^{12}C nucleus was populated in a different manner.

Theoretical models predict significantly varying locations for the likely energy of the 2_2^+ resonance [20, 26, 41, 42]. That no evidence for, or against, the existence of a resonance has been found in the current work, no evidence has been found to support, nor contradict, any of the models.

6.2 Future outlook

Though no evidence of the 2_2^+ resonance has been found, limitations in both energy and angular resolution prevent the dismissal of its existence in either the 9.7 MeV or $10.5-12$ MeV regions. Inelastic scattering experiments using either the ^{12}C(p,p')^{12}C or ^{12}C(α,α')^{12}C reaction are both candidate methods for further investigating the 3^- region in particular. A recent ^{12}C(p,p')^{12}C experiment carried out at iThemba LABS by Freer *et al.* [45], as well as further measurements carried out at Yale by Zimmerman *et al.* [64], has found evidence suggesting a broad 2^+ state lying slightly lower in energy than the 9.64 MeV, 3^-, state. Future measurements are also planned which would combine the α-particle measurements with a magnetic spectrometer, allowing improved angular resolution and a more sensitive angular correlation analysis.

Appendix A

Angular Correlations Measurements

To remain consistent with [53] the reaction considered in this report:

$$^{12}\mathrm{C}[^{12}\mathrm{C}, ^{12}\mathrm{C}^* \rightarrow ^{8}\mathrm{Be} + \alpha]^{12}\mathrm{C} \ ,$$

will be replaced by the notation

$$\mathrm{a}[\mathrm{A}, \mathrm{B}^* \rightarrow \mathrm{c} + \mathrm{C}]\mathrm{b} \ .$$

Assuming that the break-up occurs through a definite intermediate state, B^*, the double differential cross section can be written in a representation in which only magnetic quantum numbers are shown explicitly:

$$\frac{\mathrm{d}^2\sigma}{\mathrm{d}\Omega^*\mathrm{d}\Omega_\psi} \propto \sum_{\mathrm{m_a m_A m_c m_C m_b}} \left| \sum_{\mathrm{m_{B^*}}} \mathrm{T}^{\mathrm{m_a m_A}}_{\mathrm{m_b m_{B^*}}} \left(\Omega^*\right) \mathrm{T}^{\mathrm{m_{B^*}}}_{\mathrm{m_c m_C}} \left(\Omega_\psi\right) \right|^2 \tag{A.1}$$

where $\mathrm{T}^{\mathrm{m_a m_A}}_{\mathrm{m_b m_{B^*}}} \left(\Omega^*\right)$ is the formation transition amplitude between the states with quantum numbers $\mathrm{m_a}$, $\mathrm{m_A}$ and $\mathrm{m_b}$, $\mathrm{m_{B^*}}$; $\mathrm{T}^{\mathrm{m_{B^*}}}_{\mathrm{m_c m_C}} \left(\Omega_\psi\right)$ is the decay transition amplitude from the B^* resonance with quantum number $\mathrm{m_{B^*}}$ to the break-up fragments with quantum numbers $\mathrm{m_c}$ and $\mathrm{m_C}$.

If the decay from the B^* resonance into break-up fragments c and C produces two spin-

zero ground state nuclei then the decay transition amplitude can be replaced in terms of spherical harmonics:

$$\mathrm{T}^{\mathrm{m_{B^*}}}_{0\,0} \propto \mathrm{Y}_{\mathrm{J_{B^*}m_{B^*}}}\left(\Omega_\psi\right) \tag{A.2}$$

and hence equation A.1 simplifies to

$$\frac{\mathrm{d}^2\sigma}{\mathrm{d}\Omega^*\mathrm{d}\Omega_\psi} \propto \sum_{\mathrm{m_a m_A m_b}} \left| \sum_{\mathrm{m_{B^*}}} \mathrm{T}^{\mathrm{m_a m_A}}_{\mathrm{m_b m_{B^*}}}\left(\Omega^*\right) \mathrm{Y}^{\mathrm{m_{B^*}}}_{\mathrm{J_{B^*}}}\left(\Omega_\psi\right) \right|^2 \tag{A.3}$$

If the target and projectile are also spin-zero nuclei, and the recoil nucleus is also produced in its ground state, then parity conservation laws dictate that the intermediate state of spin $\mathrm{J_{B^*}}$ has a natural parity (-1)$^{\mathrm{J}}$. This reduction in possible combinations of m-substates results in the truncation of the coherent sum an incoherent sum over the magnetic substates of B*. The cross section for the formation of the intermediate state becomes

$$\frac{\mathrm{d}\sigma}{\mathrm{d}\Omega^*}\left(0 \rightarrow \mathrm{J_{B^*}}\right) = \sum_{\mathrm{m_{B^*}}=-\mathrm{J_{B^*}}}^{\mathrm{J_{B^*}}} \left|\mathrm{f}_{\mathrm{J_{B^*}m_{B^*}}}\left(\Omega^*\right)\right|^2 \tag{A.4}$$

where the transition amplitudes, $\mathrm{T}^{0\,0}_{0\mathrm{m_{B^*}}}$, have been replaced by the m-substate populations $\mathrm{f}_{\mathrm{J_{B^*}m_{B^*}}}(\theta^*, \phi^*)$ (which also transform as spherical harmonics), and hence equation A.3 reduces to

$$\frac{\mathrm{d}^2\sigma}{\mathrm{d}\Omega^*\mathrm{d}\Omega_\psi} = \left|\mathrm{f}_{\mathrm{J_{B^*}m_{B^*}}}\left(\Omega^*\right) \mathrm{Y}^{\mathrm{m_{B^*}}}_{\mathrm{J_{B^*}}}\left(\Omega_\psi\right)\right|^2 \tag{A.5}$$

Expanding the spherical harmonics then allows the azimuthal dependence of the decay process to be separated from the ψ dependence:

$$\frac{\mathrm{d}^2\sigma}{\mathrm{d}\Omega^*\mathrm{d}\Omega_\psi} = \frac{2\mathrm{J_{B^*}}+1}{4\pi} \left| \sum_{\mathrm{m_{B^*}}} (-1)^{\mathrm{m_{B^*}}} \sqrt{\frac{(\mathrm{J_{B^*}} - |\mathrm{m_{B^*}}|)!}{(\mathrm{J_{B^*}} + |\mathrm{m_{B^*}}|)!}} \mathrm{f}_{\mathrm{J_{B^*}m_{B^*}}}\left(\Omega^*\right) \mathrm{e}^{\mathrm{im_{B^*}}\chi} \mathrm{P}^{\mathrm{m_{B^*}}}_{\mathrm{J_{B^*}}}\left(\psi\right) \right|^2 \tag{A.6}$$

The exponential factor can be further expanded in terms of $\cos(\mathrm{m_{B^*}}\chi)$ and $\sin(\mathrm{m_{B^*}}\chi)$ components. If the beam axis is taken as the quantization axis then $\mathrm{f_{Jm}} = (-1)^{\mathrm{m}}\mathrm{f_{J-m}}$ and

$P_J^m = (-1)^m P_J^{-m}$, all the $\sin(m_{B^*}\chi)$ terms cancel, and equation A.6 becomes

$$\frac{d^2\sigma}{d\Omega^* d\Omega_\psi} = \frac{2J_{B^*}+1}{4\pi}\Bigg| f_{J_{B^*}0}(\Omega^*)P_{J_{B^*}}(\cos\psi) + \sum_{m_{B^*}=1}^{J_{B^*}} 2\,(-1)^{m_{B^*}} \sqrt{\frac{(J_{B^*}-|m_{B^*}|)!}{(J_{B^*}+|m_{B^*}|)!}} f_{J_{B^*}m_{B^*}}\,(\Omega^*)\,P_{J_{B^*}}^{m_{B^*}}\,(\psi)\cos(m_{B^*}\chi)\Bigg|^2 \quad \text{(A.7)}$$

If the case is considered when the correlations are restricted to the area around $\theta^* \approx 0$ then the nucleus can only be formed in the $m = 0$ substate. Under this condition all the m-state populations vanish except $f_{J_{B^*}0}$ and so

$$\frac{d^2\sigma}{d\Omega^* d\Omega_\psi} = \frac{2J_{B^*}+1}{4\pi}\left|P_{J_{B^*}}(\cos\psi)\right|^2 \quad \text{(A.8)}$$

If θ^* is restricted to the region $\theta^* \approx 0$, the correlations will therefore follow a Legendre polynomial in $\cos\psi$, of order J_{B^*}.

The case can also be considered when θ^* is unrestricted, but ψ is constrained such that $\psi = 0$ or 180. In this case then all the non-zero magnetic substates vanish once again and equation A.7 becomes

$$\frac{d^2\sigma}{d\Omega^* d\Omega_\psi} = \frac{2J_{B^*}+1}{4\pi}\left|f_{J_{B^*}0}\,(\Omega^*)\right|^2 \quad \text{(A.9)}$$

By considering the angular momenta involved in the reaction process, and also assuming that the reaction is dominated by a single entrance channel partial wave, l_i, (i.e. the reaction proceeds through a resonance in the intermediate system), then the transition amplitude for the excitation process can be written as

$$T_{m_{B^*}}^{J_{B^*}}\,(\theta^*) = \sum_{m_i m_f} \langle J_{B^*}, m_{B^*}, l_f, m_f | l_i, m_i\rangle \times Y_{l_i}^0\,(0,0)\,Y_{l_f}^{m_f}\,(\theta^*,0) \quad \text{(A.10)}$$

where m_i and m_f are the magnetic substates associated with the initial and final state angular momenta l_f and l_f. If for a reaction $\psi = 0$ (and hence m_{B^*}) and $m_i = 0$ then $m_f = 0$ and the

differential cross section becomes

$$\frac{\mathrm{d}^2\sigma}{\mathrm{d}\Omega}^2 = |\mathrm{P}_{\mathrm{l_f}}(\cos\theta^*)|^2 \tag{A.11}$$

This means that if the reaction proceeds through a dominant single entrance channel partial wave, it is possible to determine the final state orbital angular momentum:

$$\mathrm{l_f} = \mathrm{l_i} - \mathrm{J_{B^*}}$$

In order to use equation A.7 to calculate the correlation patterns away from the region around $\theta^* = 0$ and $\psi = 0, 180^\circ$ it is necessary to compute the transition amplitudes or magnetic substate populations within the framework of a suitable reaction model[1]. As discussed previously, in the $\theta^* = 0$ region the correlation follows a Legendre polynomial of order $\mathrm{J_{B^*}}$. Away from $\theta^* = 0$ the periodicity of the correlation structure remains constant, however a shift in the phase occurs. This shift has been described semi-classically by da Silviera [54], and can be related to the exit channel, and hence also the entrance channel, angular momentum:

$$\frac{\Delta\theta^*}{\Delta\psi} = \frac{\mathrm{J_{B^*}}}{\mathrm{l_f}} = \frac{\mathrm{J_{B^*}}}{\mathrm{l_i} - \mathrm{J_{B^*}}} \tag{A.12}$$

The results is a ridge structure in the correlation pattern seen in the $\theta^* - \psi$ plane, with a gradient describable by the initial state angular momentum, $\mathrm{l_i}$, and the spin of the excited state, $\mathrm{J_{B^*}}$.

[1] An example showing a case in which the transition amplitudes are calculated for the ^{12}C(^{24}Mg,^{24}Mg*)^{12}C reaction proceeding through a $\mathrm{J}^\pi = 4^+$ resonance in ^{24}Mg using a DWBA code is discussed in [53].

Appendix B

Calculation of angular hit position

After determining the position of a hit on a detector (section 3.1.4), it is necessary to convert this into a position measured relative to the complete detector setup. This was done by converting an x- and y-coordinate measured on a detector, to a ϕ_{x} and ϕ_{y} angle relative to the beam axis. Due to the orientation of the detector telescopes, this resulted in the method used to calculate ϕ_{y} for telescopes 1 and 2 also being used calculate ϕ_{x} for telescopes 3 and 4, and vice-versa. The following discussion assumes that ϕ_{x} and ϕ_{y} are being calculated for either telescope 1 or 2, and thus x and y must be swapped with one another if considering telescope 3 or 4.

B.1 Angular hit position parallel to strip direction, ϕ_{y}

Figure B.1 shows a cross-sectional, schematic view of a detector, and its position relative to the beam axis. The red arrow indicates the path of a particle, incident on the detector at a distance y_{strip} along a strip. This distance can be converted to a distance y_{tot} using

$$y_{tot} = \frac{l}{\cos\psi} - (65 - y_{strip}) \ , \tag{B.1}$$

where

$$\psi = \sin^{-1}\left(\frac{h}{70}\right) \ . \tag{B.2}$$

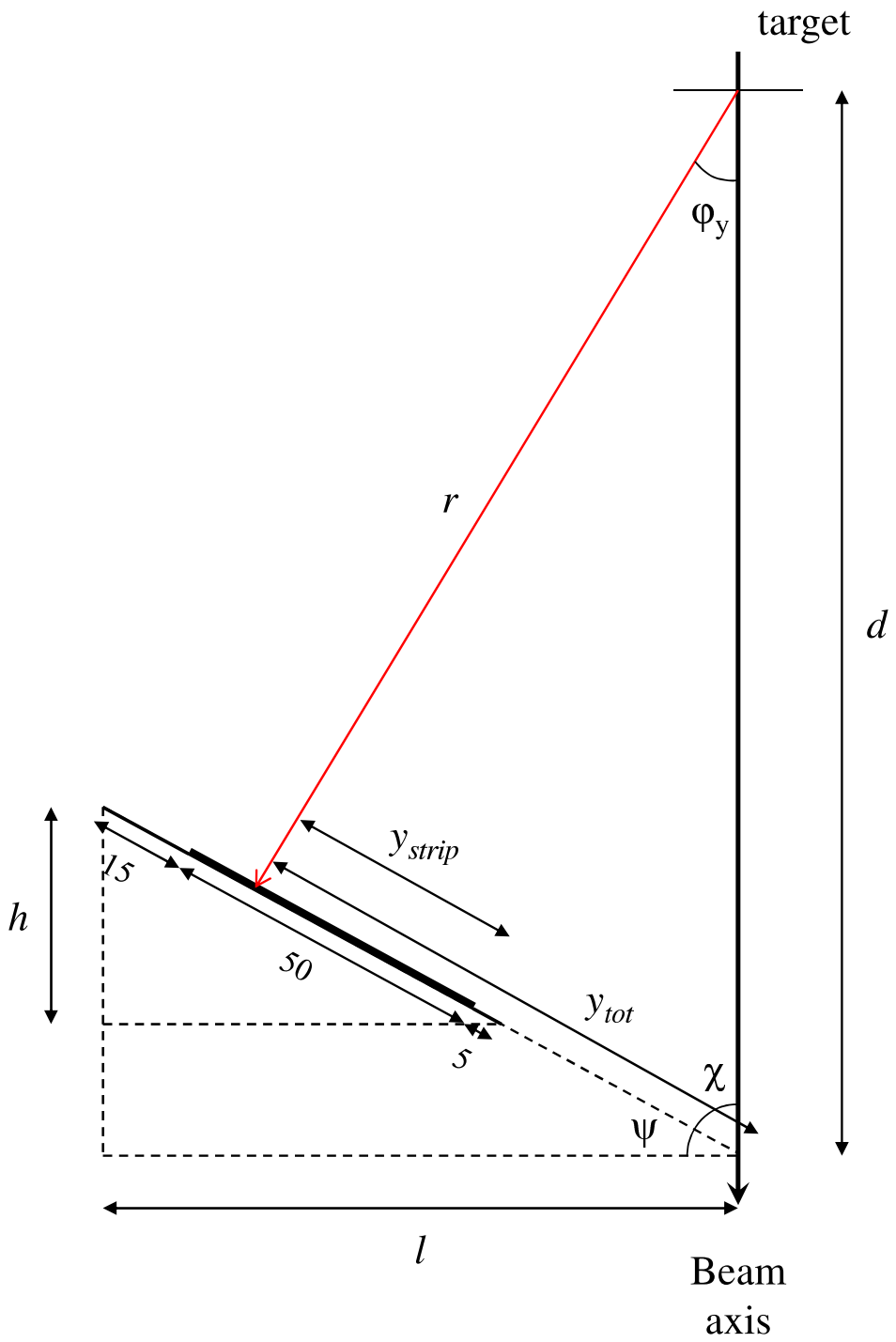

Figure B.1: Schematic diagram showing how the angular position of a hit was calculated; the red arrow indicates the path of the incident particle. The distances d, h, and l are constant for a detector, but vary for each of the four telescopes. All measurements are in mm.

The path length of the particle, r, can then be calculated using the cosine rule:

$$r^2 = {y_{tot}}^2 + d^2 - 2y_{tot}d\cos\chi \ , \tag{B.3}$$

where

$$\chi = 90 - \psi \ . \tag{B.4}$$

Finally, the sine rule can be used to calculate the desired angle, ϕ_{y}:

$$\sin\phi_{\mathrm{y}} = y_{tot}\frac{\sin\chi}{r} \ . \tag{B.5}$$

B.2 Angular hit position perpendicular to strip direction, ϕ_{x}

The angular hit position perpendicular to the strip direction, ϕ_{x}, was calculated by considering which of the 16 strips was hit. The angular position of a hit on strip j is given by:

$$\phi_{\mathrm{x}} = \tan^{-1}\left(\frac{(8 - j + \epsilon) \times x_{width}}{d}\right) \ , \tag{B.6}$$

where ϵ is a randomly generated number between 0 and 1 (included to spread hits across the full width of each strip), x_{width} is the width of a strip (3.125 mm), and d is as defined in figure B.1.

B.3 Parameters required for converting to angular positions

The distances d, h, and l, required to calculate the angular position of a hit, are different for each telescope. The measurements for each telescope are shown in table B.1.

Variable	Telescope number			
	1	2	3	4
d	164.4	161.4	145.4	145.3
h	33.5	32.0	20.5	20.0
l	98.0	98.0	76.5	76.5

Table B.1: Parameters associated with the different telescopes required to calculate the angular position of a hit (all values in mm).

Appendix C

Fitting Routine Derivations

$$
\begin{aligned}
f(E_x) &= \frac{\mathrm{e}^{-\left(\frac{E_x-c_1}{\sqrt{2}\sigma_1}\right)^2} + \alpha\mathrm{e}^{-\left(\frac{E_x-c_2}{\sqrt{2}\sigma_2}\right)^2}}{\sqrt{2\pi}\left(\sigma_1+\alpha\sigma_2\right)} - \frac{\mathrm{e}^{-\left(\frac{E_x-c_1}{\sqrt{2}\sigma_1}\right)^2} + \beta\mathrm{e}^{-\left(\frac{E_x-c_2}{\sqrt{2}\sigma_2}\right)^2}}{\sqrt{2\pi}\left(\sigma_1+\beta\sigma_2\right)} \qquad \text{(C.1)}\\
&= \frac{1}{\sqrt{2\pi}\left(\sigma_1+\alpha\sigma_2\right)\left(\sigma_1+\beta\sigma_2\right)}\left[\left(\mathrm{e}^{-\left(\frac{E_x-c_1}{\sqrt{2}\sigma_1}\right)^2} + \alpha\mathrm{e}^{-\left(\frac{E_x-c_2}{\sqrt{2}\sigma_2}\right)^2}\right)\left(\sigma_1+\beta\sigma_2\right)\right.\\
&\qquad \left. - \left(\mathrm{e}^{-\left(\frac{E_x-c_1}{\sqrt{2}\sigma_1}\right)^2} + \beta\mathrm{e}^{-\left(\frac{E_x-c_2}{\sqrt{2}\sigma_2}\right)^2}\right)\left(\sigma_1+\alpha\sigma_2\right)\right]\\
&= \frac{1}{\sqrt{2\pi}\left(\sigma_1+\alpha\sigma_2\right)\left(\sigma_1+\beta\sigma_2\right)}\left[\sigma_1\mathrm{e}^{-\left(\frac{E_x-c_1}{\sqrt{2}\sigma_1}\right)^2} + \beta\sigma_2\mathrm{e}^{-\left(\frac{E_x-c_1}{\sqrt{2}\sigma_1}\right)^2}\right.\\
&\qquad + \alpha\sigma_1\mathrm{e}^{-\left(\frac{E_x-c_2}{\sqrt{2}\sigma_2}\right)^2} + \alpha\beta\sigma_2\mathrm{e}^{-\left(\frac{E_x-c_2}{\sqrt{2}\sigma_2}\right)^2}\\
&\qquad - \sigma_1\mathrm{e}^{-\left(\frac{E_x-c_1}{\sqrt{2}\sigma_1}\right)^2} - \alpha\sigma_2\mathrm{e}^{-\left(\frac{E_x-c_1}{\sqrt{2}\sigma_1}\right)^2}\\
&\qquad \left. - \beta\sigma_1\mathrm{e}^{-\left(\frac{E_x-c_2}{\sqrt{2}\sigma_2}\right)^2} - \alpha\beta\sigma_2\mathrm{e}^{-\left(\frac{E_x-c_2}{\sqrt{2}\sigma_2}\right)^2}\right]\\
&= \frac{1}{\sqrt{2\pi}\left(\sigma_1+\alpha\sigma_2\right)\left(\sigma_1+\beta\sigma_2\right)}\left[\beta\sigma_2\mathrm{e}^{-\left(\frac{E_x-c_1}{\sqrt{2}\sigma_1}\right)^2} + \alpha\sigma_1\mathrm{e}^{-\left(\frac{E_x-c_2}{\sqrt{2}\sigma_2}\right)^2}\right.\\
&\qquad \left. - \alpha\sigma_2\mathrm{e}^{-\left(\frac{E_x-c_1}{\sqrt{2}\sigma_1}\right)^2} - \beta\sigma_1\mathrm{e}^{-\left(\frac{E_x-c_2}{\sqrt{2}\sigma_2}\right)^2}\right]\\
&= \frac{1}{\sqrt{2\pi}\left(\sigma_1+\alpha\sigma_2\right)\left(\sigma_1+\beta\sigma_2\right)}\left[\left(\beta-\alpha\right)\sigma_2\mathrm{e}^{-\left(\frac{E_x-c_1}{\sqrt{2}\sigma_1}\right)^2} + \left(\alpha-\beta\right)\sigma_1\mathrm{e}^{-\left(\frac{E_x-c_2}{\sqrt{2}\sigma_2}\right)^2}\right]\\
f(E_x) &= \frac{\alpha-\beta}{\left(\sigma_1+\alpha\sigma_2\right)\left(\sigma_1+\beta\sigma_2\right)}\left[-\sigma_2\frac{\mathrm{e}^{-\left(\frac{E_x-c_1}{\sqrt{2}\sigma_1}\right)^2}}{\sqrt{2\pi}} + \sigma_1\frac{\mathrm{e}^{-\left(\frac{E_x-c_2}{\sqrt{2}\sigma_2}\right)^2}}{\sqrt{2\pi}}\right] \qquad \text{(C.2)}
\end{aligned}
$$

In the limit that $\alpha\sigma_2 \ll \sigma_1$ and $\beta\sigma_2 \ll \sigma_1$ then C.2 becomes

$$\begin{aligned} f(E_x) &\simeq \frac{\alpha-\beta}{\sigma_1^2}\left[-\sigma_2\frac{\mathrm{e}^{-\left(\frac{E_x-c_1}{\sqrt{2}\sigma_1}\right)^2}}{\sqrt{2\pi}}+\sigma_1\frac{\mathrm{e}^{-\left(\frac{E_x-c_2}{\sqrt{2}\sigma_2}\right)^2}}{\sqrt{2\pi}}\right] \\ &= (\alpha-\beta)\frac{\sigma_2}{\sigma_1}\left[-\frac{\mathrm{e}^{-\left(\frac{E_x-c_1}{\sqrt{2}\sigma_1}\right)^2}}{\sqrt{2\pi}\sigma_1}+\frac{\mathrm{e}^{-\left(\frac{E_x-c_2}{\sqrt{2}\sigma_2}\right)^2}}{\sqrt{2\pi}\sigma_2}\right] \end{aligned} \tag{C.3}$$

Appendix D

Example MathCad sheet

Contained within this appendix is an example of the MathCad sheets used to perform the analysis from section 4.6. The simulation used is a 15%, 250keV wide 2^+ resonance, with a centroid position of 9.85 MeV. The example sheet shows parameters for a case in which the routine is considered to have accurately matched the features of the underlying 2^+ simulation, and therefore has a relatively low χ^2 value. The later pages show plots of χ^2 values for a variety of guess parameters, from which the routine's optimum values of percentage/width/centroid position can be determined.

Import Data

Data exported from SunSort and imported as lists.

on_1:=

	0	1
0	0	0
1	1	0
2	2	0
3	3	0
4	4	0
5	5	0
6	6	0
7	7	0
8	8	0
9	9	...

toton:=107294

off1:=

	0	1
0	0	0
1	1	0
2	2	0
3	3	0
4	4	0
5	5	0
6	6	0
7	7	0
8	8	0
9	9	...

toton:=6713

Data is compressed by a factor of three (i.e. 3 channels are combined into 1) and the spectra are then normalised to the areas of the 3^- peaks (toton1 and totoff1 respectively).

$$\text{comp} := 3 \qquad \text{i} := 0..\frac{1023 - \text{comp}}{\text{comp}}$$

$$\text{on1}_{i,0} := \sum_{k=0}^{\text{comp}-1} \frac{\text{on\_1}_{k+i\cdot\text{comp},0}}{\text{comp}} \qquad \text{on1}_{i,1} := \sum_{k=0}^{\text{comp}-1} \text{on\_1}_{k+i\cdot\text{comp},1}$$

$$\text{off1c}_{i,0} := \sum_{k=0}^{\text{comp}-1} \frac{\text{off\_1}_{k+i\cdot\text{comp},0}}{\text{comp}} \qquad \text{off1c}_{i,1} := \sum_{k=0}^{\text{comp}-1} \text{off1\_1}_{k+i\cdot\text{comp},1}$$

Apply the fitting routine

Calculate the number of the new compressed channels that make up the 3^- peak, and also at which compressed channel number the 3^- peak begins. Redefine i *to range from* 0 *to* N.

$$\text{N} := \frac{321 - 213}{\text{comp}} \qquad \text{i} := 0..\text{N}$$

The compressed channel data is then converted into excitation energy (x) and the difference between the normalised data sets (y).

$$x_i := 7.272 + \frac{10.2 \cdot \left(i + \frac{213}{comp}\right)}{340} \qquad y_i := \frac{off1c_{i+\frac{213}{comp},1}}{totoff1} - \frac{on1_{i+\frac{213}{comp},1}}{toton1}$$

Errors on the data are calculated. It is assumed that the error on the windowed data set is dominant due to the significantly worse statistics. The total error is therefore approximated as the windowed error.

$$error_i := \left(off1c_{i+\frac{213}{comp},1}\right)^{\frac{1}{2}}$$

$$error\_hi_i := \frac{error_i}{totoff1} + \frac{off1c_{i+\frac{213}{comp},1}}{totoff1} - \frac{on1_{i+\frac{213}{comp},1}}{toton1}$$

$$error\_lo_i := \frac{(-error_i)}{totoff1} + \frac{off1c_{i+\frac{213}{comp},1}}{totoff1} - \frac{on1_{i+\frac{213}{comp},1}}{toton1}$$

Known parameters about the width and centroid position of the 3^- peak are entered, as well as an estimated percentage strength of the 2^+ resonance (the value α in the equations discussed in chapter 4).

Gaussian width:

$$w_1 := \frac{0.16}{2.35}$$

Gaussian centroid:

$$c_1 := 9.64$$

Percentage contribution:

$$percent := 0.02$$

Next, the fitting routine is constructed and passed to MathCad as a matrix, of which the elements consist of the fitting function itself, followed by the derivatives of the routine with respect to each of the fitting variables.

$$
\mathrm{f}(\mathrm{x},\mathrm{u}) := \left[
\begin{array}{ll}
0.03 \cdot \left[\dfrac{\exp\left[-\left(\frac{\mathrm{x}-\mathrm{c}_1}{\sqrt{2}\mathrm{w}_1}\right)^2\right] + \mathrm{percent}\cdot\exp\left[-\left(\frac{\mathrm{x}-\mathrm{u}_1}{\sqrt{2}\mathrm{u}_2}\right)^2\right]}{\sqrt{2\pi}\left(\mathrm{w}_1 + \mathrm{percent}\cdot\mathrm{u}_2\right)} + \dfrac{\exp\left[-\left(\frac{\mathrm{x}-\mathrm{c}_1}{\sqrt{2}\mathrm{w}_1}\right)^2\right] + \mathrm{u}_0\cdot\exp\left[-\left(\frac{\mathrm{x}-\mathrm{u}_1}{\sqrt{2}\mathrm{u}_2}\right)^2\right]}{\sqrt{2\pi}\left(\mathrm{w}_1 + \mathrm{u}_0\cdot\mathrm{u}_2\right)} + \mathrm{u}_3 \right] & \parallel \textit{Fitting function} \\
0.03 \cdot \left[-\dfrac{\exp\left[-\left(\frac{\mathrm{x}-\mathrm{u}_1}{\sqrt{2}\mathrm{u}_2}\right)^2\right]}{\sqrt{2\pi}\left(\mathrm{w}_1 + \mathrm{u}_0\cdot\mathrm{u}_2\right)} + \dfrac{\mathrm{u}_2\cdot\exp\left[-\left(\frac{\mathrm{x}-\mathrm{c}_1}{\sqrt{2}\mathrm{w}_1}\right)^2\right] + \mathrm{u}_0\cdot\exp\left[-\left(\frac{\mathrm{x}-\mathrm{u}_1}{\sqrt{2}\mathrm{u}_2}\right)^2\right]}{\sqrt{2\pi}\left(\mathrm{w}_1 + \mathrm{u}_0\cdot\mathrm{u}_2\right)^2} \right] & \parallel \textit{Derivative w.r.t. } \mathrm{u}_0 \\
0.03 \cdot \left[\mathrm{percent} \cdot \dfrac{\mathrm{x}-\mathrm{u}_1}{{\mathrm{u}_2}^2} \cdot \dfrac{\exp\left[-\left(\frac{\mathrm{x}-\mathrm{u}_1}{\sqrt{2}\mathrm{u}_2}\right)^2\right]}{\sqrt{2\pi}\left(\mathrm{w}_1 + \mathrm{u}_0\cdot\mathrm{u}_2\right)} - \mathrm{u}_0 \cdot \dfrac{\mathrm{x}-\mathrm{u}_1}{{\mathrm{u}_2}^2} \cdot \dfrac{\exp\left[-\left(\frac{\mathrm{x}-\mathrm{u}_1}{\sqrt{2}\mathrm{u}_2}\right)^2\right]}{\sqrt{2\pi}\left(\mathrm{w}_1 + \mathrm{u}_0\cdot\mathrm{u}_2\right)} \right] & \parallel \textit{Derivative w.r.t. } \mathrm{u}_1 \\
0.03 \cdot \left[\mathrm{percent} \left(\dfrac{\left(\mathrm{x}-\mathrm{u}_1\right)^2}{{\mathrm{u}_2}^3} \cdot \dfrac{\exp\left[-\left(\frac{\mathrm{x}-\mathrm{u}_1}{\sqrt{2}\mathrm{u}_2}\right)^2\right]}{\sqrt{2\pi}\left(\mathrm{w}_1 + \mathrm{percent}\cdot\mathrm{u}_2\right)} - \dfrac{\exp\left[-\left(\frac{\mathrm{x}-\mathrm{c}_1}{\sqrt{2}\mathrm{w}_1}\right)^2\right] + \mathrm{percent}\cdot\exp\left[-\left(\frac{\mathrm{x}-\mathrm{u}_1}{\sqrt{2}\mathrm{u}_2}\right)^2\right]}{\sqrt{2\pi}\left(\mathrm{w}_1 + \mathrm{percent}\cdot\mathrm{u}_2\right)} \right) \right. & \parallel \textit{Derivative w.r.t. } \mathrm{u}_2 \\
\qquad \left. - \mathrm{u}_0 \left(\dfrac{\left(\mathrm{x}-\mathrm{u}_1\right)^2}{{\mathrm{u}_2}^3} \cdot \dfrac{\exp\left[-\left(\frac{\mathrm{x}-\mathrm{u}_1}{\sqrt{2}\mathrm{u}_2}\right)^2\right]}{\sqrt{2\pi}\left(\mathrm{w}_1 + \mathrm{u}_0\cdot\mathrm{u}_2\right)} - \dfrac{\exp\left[-\left(\frac{\mathrm{x}-\mathrm{c}_1}{\sqrt{2}\mathrm{w}_1}\right)^2\right] + \mathrm{u}_0\cdot\exp\left[-\left(\frac{\mathrm{x}-\mathrm{u}_1}{\sqrt{2}\mathrm{u}_2}\right)^2\right]}{\sqrt{2\pi}\left(\mathrm{w}_1 + \mathrm{u}_0\cdot\mathrm{u}_2\right)} \right) \right] & \\
0.03 \cdot 1 & \parallel \textit{Derivative w.r.t. } \mathrm{u}_3
\end{array}
\right]
$$

A vector is created to pass starting values to the routine, from which the fit is optimised:

$$\text{guess} := \begin{pmatrix} 0.03 \cdot 0.021 \\ 9.7 \\ \frac{0.05}{2.35} \\ 0.030 \end{pmatrix}$$

The genfit *function is used to instruct MathCad to apply the fitting routine.*

$$\text{result} := \text{genfit}(x, y, \text{guess}, f) \qquad \text{result} = \begin{pmatrix} -0.037 \\ 9.818 \\ 0.138 \\ 8.139 \times 10^{-5} \end{pmatrix}$$

$$\text{width} := \text{result}_2 \times 2.35 \qquad \text{width} = 0.325$$

The fit is plotted against the original data.

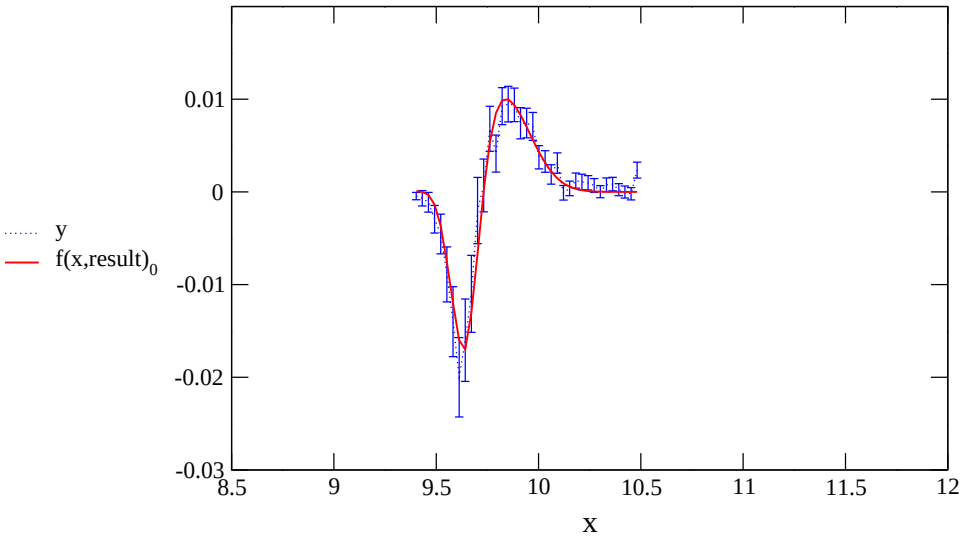

A χ^2 *value is then calculated for the fit.*

$$\text{chi} := \sum_{x=0}^{N} \frac{(\text{fit}_x - y_x)^2}{\left(\frac{\text{error}_x}{\text{totoff1}}\right)^2} \qquad \text{chi} = 33.23$$

$$\text{chi2} := \frac{\text{chi}}{36 - 5} \qquad \text{chi2} = 1.067$$

For a given 'percent' value, a range of width values are tried in the guess factor, whilst keeping the guess values for the centroid position and percentage contribution constant. The value of chi2 for each width is then stored in a list. The value of the 'percent' variable is e.g. 0.02 for the res2 values and 0.05 for the res5 values.

Guesses at 0.1% above the 'percent' level and with a centroid guess of 9.70 MeV:

$$\text{res2} := \begin{pmatrix} 0.05 & 1.067 \\ 0.1 & 1.073 \\ 0.15 & 1.072 \\ 0.2 & 1.073 \\ 0.25 & 9.808 \\ 0.3 & 1.069 \\ 0.35 & 1.073 \\ 0.4 & 1.073 \\ 0.45 & 1.068 \\ 0.5 & 5.087 \\ 0.55 & 1.068 \\ 0.6 & 1.068 \\ 0.65 & 1.073 \\ 0.7 & 1.068 \end{pmatrix} \quad \text{res5} := \begin{pmatrix} 0.05 & 1.067 \\ 0.1 & 1.067 \\ 0.15 & 1.068 \\ 0.2 & 1.068 \\ 0.25 & 1.068 \\ 0.3 & 1.068 \\ 0.35 & 1.067 \\ 0.4 & 1.068 \\ 0.45 & 1.068 \\ 0.5 & 1.068 \\ 0.55 & 1.068 \\ 0.6 & 1.068 \\ 0.65 & 1.067 \\ 0.7 & 1.068 \end{pmatrix} \quad \text{res10} := \begin{pmatrix} 0.05 & 1.075 \\ 0.1 & 1.075 \\ 0.15 & 1.066 \\ 0.2 & 1.075 \\ 0.25 & 1.066 \\ 0.3 & 1.076 \\ 0.35 & 1.075 \\ 0.4 & 1.075 \\ 0.45 & 1.075 \\ 0.5 & 1.075 \\ 0.55 & 1.075 \\ 0.6 & 1.066 \\ 0.65 & 1.075 \\ 0.7 & 1.076 \end{pmatrix} \quad \text{res15} := \begin{pmatrix} 0.05 & 1.077 \\ 0.1 & 1.079 \\ 0.15 & 1.077 \\ 0.2 & 1.076 \\ 0.25 & 1.077 \\ 0.3 & 1.077 \\ 0.35 & 1.077 \\ 0.4 & 1.077 \\ 0.45 & 1.077 \\ 0.5 & 1.076 \\ 0.55 & 1.066 \\ 0.6 & 1.078 \\ 0.65 & 1.076 \\ 0.7 & 1.072 \end{pmatrix}$$

The chi2 values are then plotted to identify the optimum guess parameters.

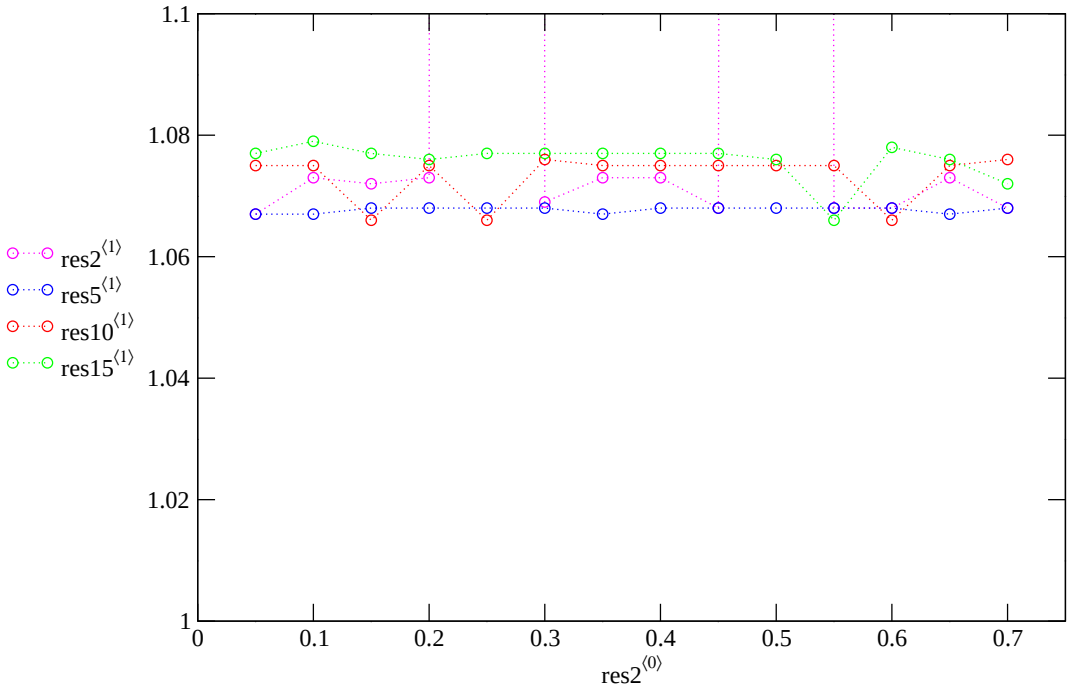

Guesses at 0.1% above the 'percent' level and with a centroid guess of 9.85 MeV:

$$\text{res2} := \begin{pmatrix} 0.05 & 1.073 \\ 0.1 & 1.069 \\ 0.15 & 1.069 \\ 0.2 & 1.069 \\ 0.25 & 1.069 \\ 0.3 & 1.072 \\ 0.35 & 1.074 \\ 0.4 & 1.068 \\ 0.45 & 1.069 \\ 0.5 & 1.043 \\ 0.55 & 1.069 \\ 0.6 & 1.069 \\ 0.65 & 1.069 \\ 0.7 & 1.049 \end{pmatrix} \quad \text{res5} := \begin{pmatrix} 0.05 & 1.068 \\ 0.1 & 1.067 \\ 0.15 & 1.069 \\ 0.2 & 1.067 \\ 0.25 & 1.068 \\ 0.3 & 1.075 \\ 0.35 & 1.067 \\ 0.4 & 1.067 \\ 0.45 & 1.066 \\ 0.5 & 1.048 \\ 0.55 & 1.075 \\ 0.6 & 1.075 \\ 0.65 & 1.069 \\ 0.7 & 1.068 \end{pmatrix} \quad \text{res10} := \begin{pmatrix} 0.05 & 1.075 \\ 0.1 & 1.075 \\ 0.15 & 1.075 \\ 0.2 & 1.075 \\ 0.25 & 1.074 \\ 0.3 & 1.076 \\ 0.35 & 1.067 \\ 0.4 & 1.079 \\ 0.45 & 1.075 \\ 0.5 & 1.067 \\ 0.55 & 1.066 \\ 0.6 & 1.067 \\ 0.65 & 1.076 \\ 0.7 & 1.075 \end{pmatrix} \quad \text{res15} := \begin{pmatrix} 0.05 & 1.077 \\ 0.1 & 1.077 \\ 0.15 & 1.077 \\ 0.2 & 1.077 \\ 0.25 & 1.076 \\ 0.3 & 1.066 \\ 0.35 & 1.066 \\ 0.4 & 1.079 \\ 0.45 & 1.076 \\ 0.5 & 1.077 \\ 0.55 & 1.077 \\ 0.6 & 1.078 \\ 0.65 & 1.073 \\ 0.7 & 1.067 \end{pmatrix}$$

The chi2 values are then once again plotted to identify the optimum guess parameters.

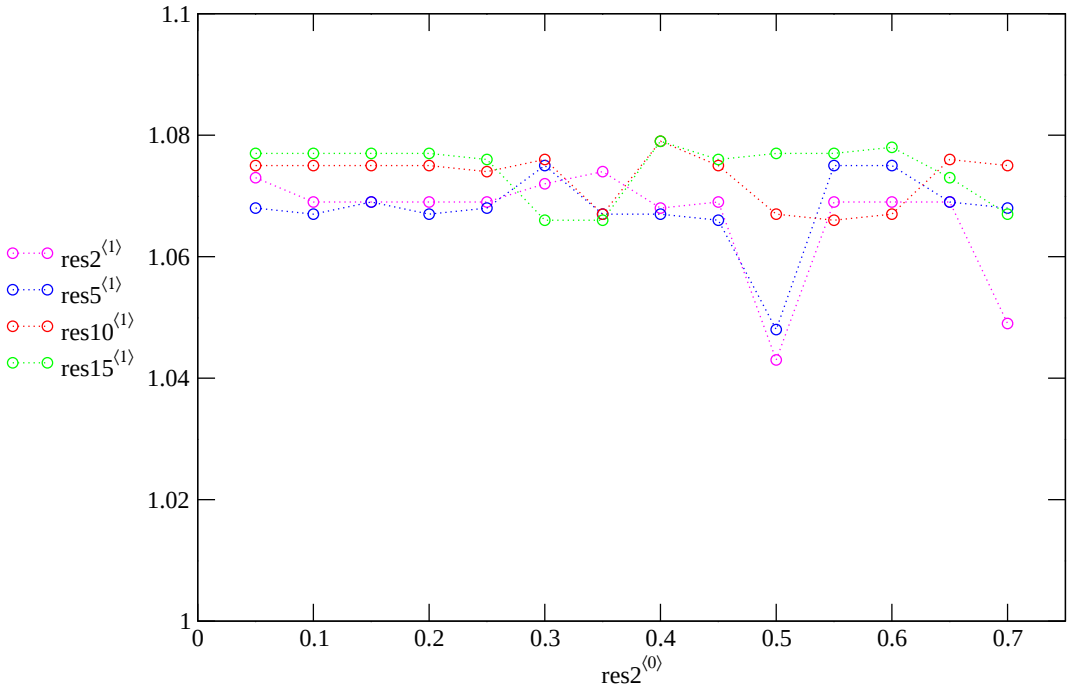

Guesses at 0.1% above the 'percent' level and with a centroid guess of 10.0 MeV:

$$\text{res2} := \begin{pmatrix} 0.05 & 1.073 \\ 0.1 & 1.073 \\ 0.15 & 1.073 \\ 0.2 & 1.073 \\ 0.25 & 1.069 \\ 0.3 & 1.069 \\ 0.35 & 1.073 \\ 0.4 & 1.073 \\ 0.45 & 1.069 \\ 0.5 & 1.073 \\ 0.55 & 1.049 \\ 0.6 & 1.073 \\ 0.65 & 1.073 \\ 0.7 & 1.073 \end{pmatrix} \quad \text{res5} := \begin{pmatrix} 0.05 & 1.075 \\ 0.1 & 1.067 \\ 0.15 & 1.067 \\ 0.2 & 1.048 \\ 0.25 & 1.048 \\ 0.3 & 1.075 \\ 0.35 & 1.075 \\ 0.4 & 1.068 \\ 0.45 & 1.068 \\ 0.5 & 1.068 \\ 0.55 & 1.068 \\ 0.6 & 1.068 \\ 0.65 & 1.069 \\ 0.7 & 1.067 \end{pmatrix} \quad \text{res10} := \begin{pmatrix} 0.05 & 1.067 \\ 0.1 & 1.075 \\ 0.15 & 1.046 \\ 0.2 & 1.075 \\ 0.25 & 1.067 \\ 0.3 & 1.075 \\ 0.35 & 1.047 \\ 0.4 & 1.075 \\ 0.45 & 1.078 \\ 0.5 & 1.075 \\ 0.55 & 1.046 \\ 0.6 & 1.046 \\ 0.65 & 1.048 \\ 0.7 & 1.075 \end{pmatrix} \quad \text{res15} := \begin{pmatrix} 0.05 & 1.067 \\ 0.1 & 1.077 \\ 0.15 & 1.277 \\ 0.2 & 1.076 \\ 0.25 & 1.077 \\ 0.3 & 1.077 \\ 0.35 & 1.077 \\ 0.4 & 1.077 \\ 0.45 & 1.077 \\ 0.5 & 1.077 \\ 0.55 & 1.077 \\ 0.6 & 1.077 \\ 0.65 & 1.077 \\ 0.7 & 1.077 \end{pmatrix}$$

The chi2 values are then once again plotted to identify the optimum guess parameters.

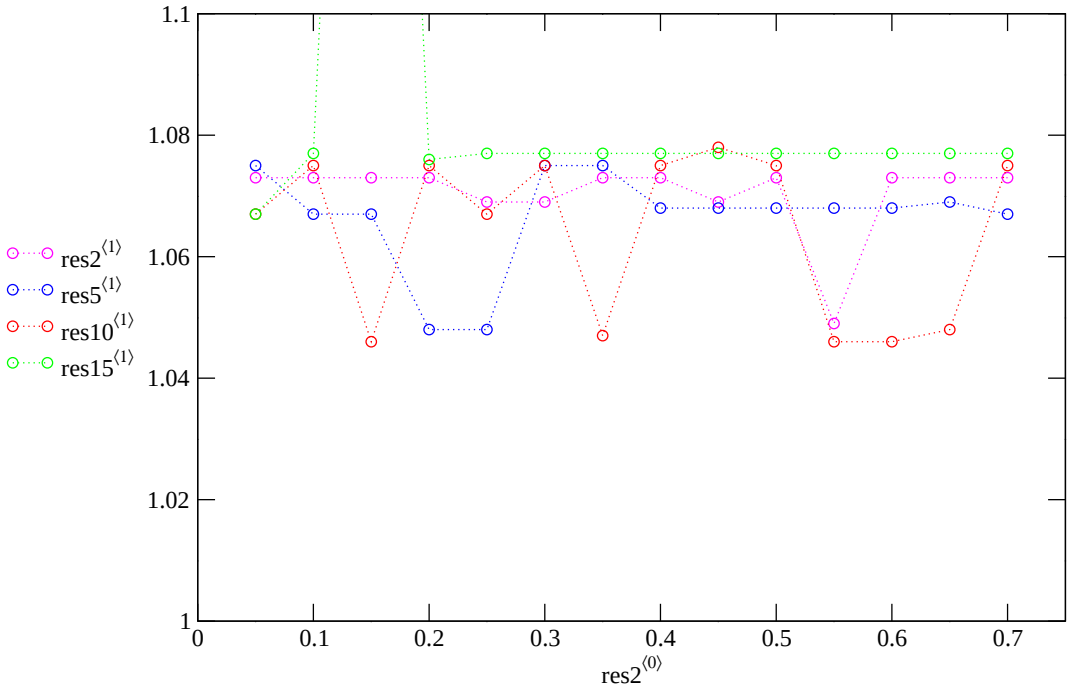

Guesses at 5% above the ‘percent’ level and with a centroid guess of 9.70 MeV:

$$\text{res2} := \begin{pmatrix} 0.05 & 1.068 \\ 0.1 & 1.069 \\ 0.15 & 1.068 \\ 0.2 & 1.073 \\ 0.25 & 1.048 \\ 0.3 & 1.069 \\ 0.35 & 1.073 \\ 0.4 & 1.069 \\ 0.45 & 1.073 \\ 0.5 & 1.069 \\ 0.55 & 1.069 \\ 0.6 & 1.073 \\ 0.65 & 1.069 \\ 0.7 & 1.068 \end{pmatrix} \quad \text{res5} := \begin{pmatrix} 0.05 & 1.068 \\ 0.1 & 1.067 \\ 0.15 & 1.068 \\ 0.2 & 1.068 \\ 0.25 & 1.067 \\ 0.3 & 1.068 \\ 0.35 & 1.067 \\ 0.4 & 1.068 \\ 0.45 & 1.068 \\ 0.5 & 1.068 \\ 0.55 & 1.068 \\ 0.6 & 1.069 \\ 0.65 & 1.060 \\ 0.7 & 1.067 \end{pmatrix} \quad \text{res10} := \begin{pmatrix} 0.05 & 1.075 \\ 0.1 & 1.075 \\ 0.15 & 1.075 \\ 0.2 & 1.075 \\ 0.25 & 1.075 \\ 0.3 & 1.066 \\ 0.35 & 1.075 \\ 0.4 & 1.075 \\ 0.45 & 1.075 \\ 0.5 & 1.075 \\ 0.55 & 1.075 \\ 0.6 & 1.066 \\ 0.65 & 1.066 \\ 0.7 & 1.067 \end{pmatrix} \quad \text{res15} := \begin{pmatrix} 0.05 & 1.046 \\ 0.1 & 1.078 \\ 0.15 & 1.077 \\ 0.2 & 1.076 \\ 0.25 & 1.077 \\ 0.3 & 1.077 \\ 0.35 & 1.077 \\ 0.4 & 1.077 \\ 0.45 & 1.077 \\ 0.5 & 1.077 \\ 0.55 & 1.076 \\ 0.6 & 1.066 \\ 0.65 & 1.077 \\ 0.7 & 1.075 \end{pmatrix}$$

The chi2 values are then once again plotted to identify the optimum guess parameters.

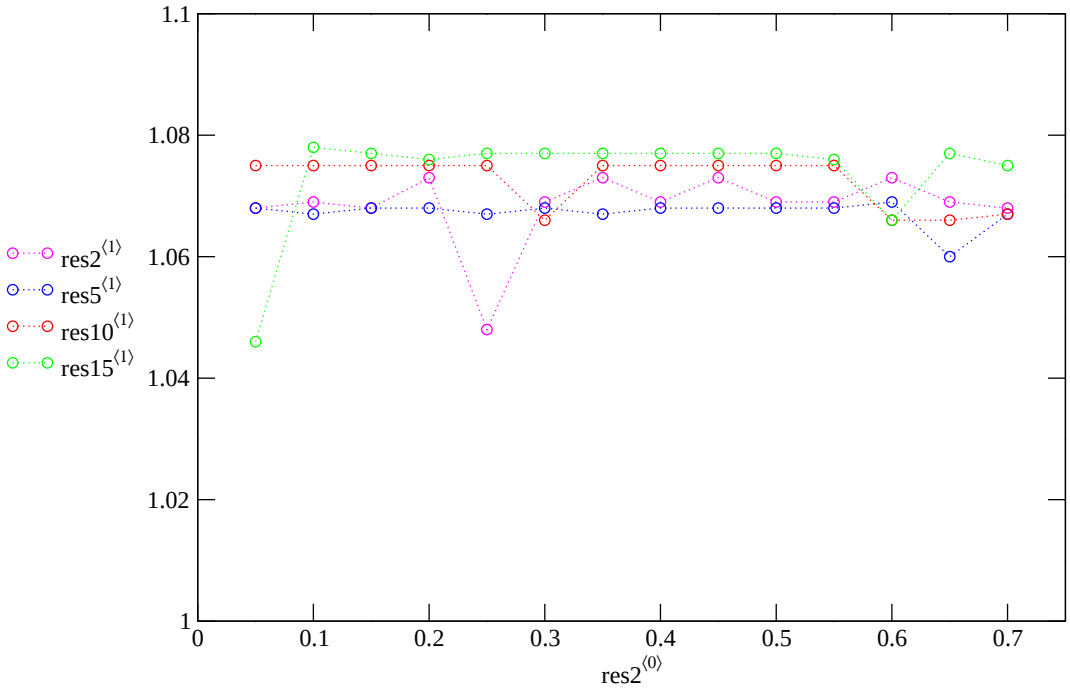

Guesses at 5% above the ‘percent’ level and with a centroid guess of 9.85 MeV:

$$\text{res2} := \begin{pmatrix} 0.05 & 1.074 \\ 0.1 & 1.069 \\ 0.15 & 1.069 \\ 0.2 & 1.069 \\ 0.25 & 1.069 \\ 0.3 & 1.069 \\ 0.35 & 1.069 \\ 0.4 & 1.069 \\ 0.45 & 1.068 \\ 0.5 & 1.069 \\ 0.55 & 1.073 \\ 0.6 & 1.073 \\ 0.65 & 1.069 \\ 0.7 & 1.069 \end{pmatrix} \quad \text{res5} := \begin{pmatrix} 0.05 & 1.046 \\ 0.1 & 1.068 \\ 0.15 & 1.068 \\ 0.2 & 1.067 \\ 0.25 & 1.068 \\ 0.3 & 1.075 \\ 0.35 & 1.067 \\ 0.4 & 1.067 \\ 0.45 & 1.073 \\ 0.5 & 1.048 \\ 0.55 & 1.075 \\ 0.6 & 1.075 \\ 0.65 & 1.069 \\ 0.7 & 1.068 \end{pmatrix} \quad \text{res10} := \begin{pmatrix} 0.05 & 1.046 \\ 0.1 & 1.075 \\ 0.15 & 1.075 \\ 0.2 & 1.075 \\ 0.25 & 1.074 \\ 0.3 & 1.076 \\ 0.35 & 1.067 \\ 0.4 & 1.077 \\ 0.45 & 1.075 \\ 0.5 & 1.067 \\ 0.55 & 1.066 \\ 0.6 & 1.067 \\ 0.65 & 1.067 \\ 0.7 & 1.075 \end{pmatrix} \quad \text{res15} := \begin{pmatrix} 0.05 & 1.077 \\ 0.1 & 1.077 \\ 0.15 & 1.077 \\ 0.2 & 1.077 \\ 0.25 & 1.076 \\ 0.3 & 1.076 \\ 0.35 & 1.066 \\ 0.4 & 1.079 \\ 0.45 & 1.076 \\ 0.5 & 1.077 \\ 0.55 & 1.077 \\ 0.6 & 1.079 \\ 0.65 & 1.063 \\ 0.7 & 1.068 \end{pmatrix}$$

The chi2 values are then once again plotted to identify the optimum guess parameters.

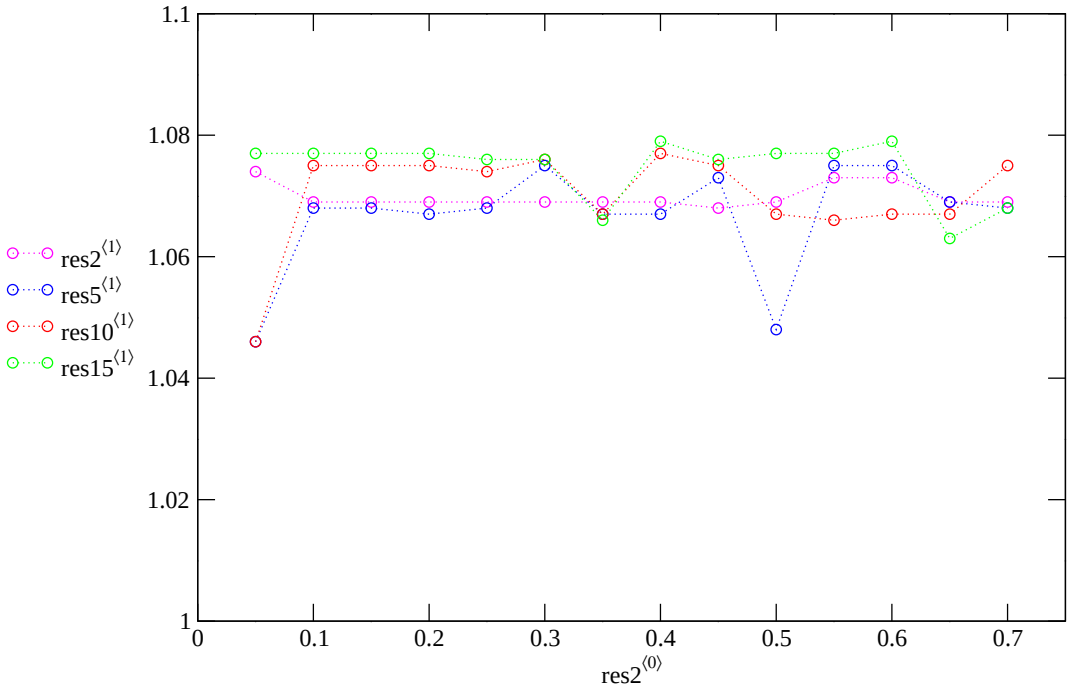

Guesses at 5% above the ‘percent’ level and with a centroid guess of 10.0 MeV:

$$\text{res2} := \begin{pmatrix} 0.05 & 1.068 \\ 0.1 & 5.278 \\ 0.15 & 1.073 \\ 0.2 & 1.074 \\ 0.25 & 1.069 \\ 0.3 & 1.069 \\ 0.35 & 1.073 \\ 0.4 & 1.073 \\ 0.45 & 1.073 \\ 0.5 & 1.049 \\ 0.55 & 1.069 \\ 0.6 & 1.044 \\ 0.65 & 1.069 \\ 0.7 & 1.069 \end{pmatrix} \quad \text{res5} := \begin{pmatrix} 0.05 & 1.075 \\ 0.1 & 1.067 \\ 0.15 & 1.068 \\ 0.2 & 1.069 \\ 0.25 & 1.067 \\ 0.3 & 1.067 \\ 0.35 & 1.069 \\ 0.4 & 1.068 \\ 0.45 & 1.068 \\ 0.5 & 1.067 \\ 0.55 & 1.067 \\ 0.6 & 1.068 \\ 0.65 & 1.075 \\ 0.7 & 1.047 \end{pmatrix} \quad \text{res10} := \begin{pmatrix} 0.05 & 1.076 \\ 0.1 & 1.076 \\ 0.15 & 1.075 \\ 0.2 & 1.075 \\ 0.25 & 1.076 \\ 0.3 & 1.075 \\ 0.35 & 1.075 \\ 0.4 & 1.075 \\ 0.45 & 1.075 \\ 0.5 & 1.076 \\ 0.55 & 1.200 \\ 0.6 & 1.066 \\ 0.65 & 1.048 \\ 0.7 & 1.047 \end{pmatrix} \quad \text{res15} := \begin{pmatrix} 0.05 & 1.067 \\ 0.1 & 1.077 \\ 0.15 & 1.077 \\ 0.2 & 1.077 \\ 0.25 & 1.077 \\ 0.3 & 1.077 \\ 0.35 & 1.078 \\ 0.4 & 1.077 \\ 0.45 & 1.077 \\ 0.5 & 1.077 \\ 0.55 & 1.077 \\ 0.6 & 1.079 \\ 0.65 & 1.077 \\ 0.7 & 1.077 \end{pmatrix}$$

The chi2 values are then once again plotted to identify the optimum guess parameters.

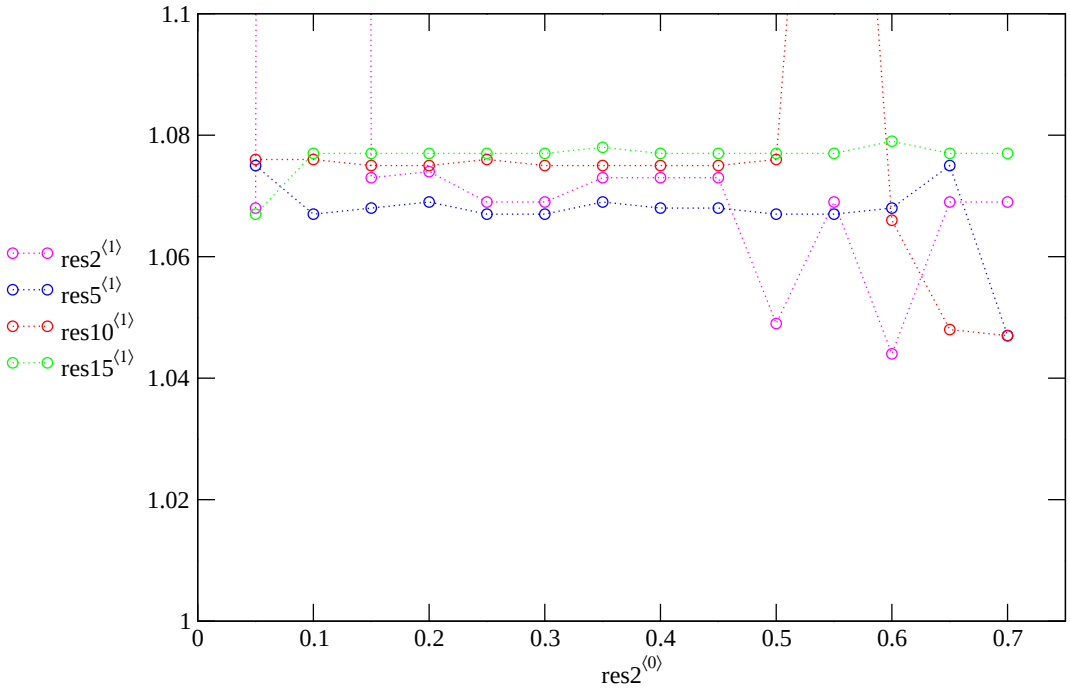

Guesses at 20% above the 'percent' level and with a centroid guess of 9.70 MeV:

$$\text{res2} := \begin{pmatrix} 0.05 & 1.069 \\ 0.1 & 1.073 \\ 0.15 & 1.068 \\ 0.2 & 1.046 \\ 0.25 & 1.073 \\ 0.3 & 1.073 \\ 0.35 & 1.073 \\ 0.4 & 1.069 \\ 0.45 & 1.073 \\ 0.5 & 1.073 \\ 0.55 & 1.073 \\ 0.6 & 1.068 \\ 0.65 & 1.073 \\ 0.7 & 1.069 \end{pmatrix} \quad \text{res5} := \begin{pmatrix} 0.05 & 1.068 \\ 0.1 & 1.068 \\ 0.15 & 1.075 \\ 0.2 & 1.073 \\ 0.25 & 1.067 \\ 0.3 & 1.068 \\ 0.35 & 1.068 \\ 0.4 & 1.069 \\ 0.45 & 1.068 \\ 0.5 & 1.068 \\ 0.55 & 1.623 \\ 0.6 & 1.068 \\ 0.65 & 1.067 \\ 0.7 & 1.075 \end{pmatrix} \quad \text{res10} := \begin{pmatrix} 0.05 & 1.075 \\ 0.1 & 1.075 \\ 0.15 & 1.075 \\ 0.2 & 1.075 \\ 0.25 & 1.076 \\ 0.3 & 1.077 \\ 0.35 & 1.075 \\ 0.4 & 1.075 \\ 0.45 & 1.075 \\ 0.5 & 1.076 \\ 0.55 & 1.075 \\ 0.6 & 1.067 \\ 0.65 & 1.076 \\ 0.7 & 1.076 \end{pmatrix} \quad \text{res15} := \begin{pmatrix} 0.05 & 1.077 \\ 0.1 & 1.071 \\ 0.15 & 1.077 \\ 0.2 & 1.077 \\ 0.25 & 1.077 \\ 0.3 & 1.076 \\ 0.35 & 1.077 \\ 0.4 & 1.077 \\ 0.45 & 1.077 \\ 0.5 & 1.077 \\ 0.55 & 1.077 \\ 0.6 & 1.077 \\ 0.65 & 1.076 \\ 0.7 & 1.075 \end{pmatrix}$$

The chi2 values are then once again plotted to identify the optimum guess parameters.

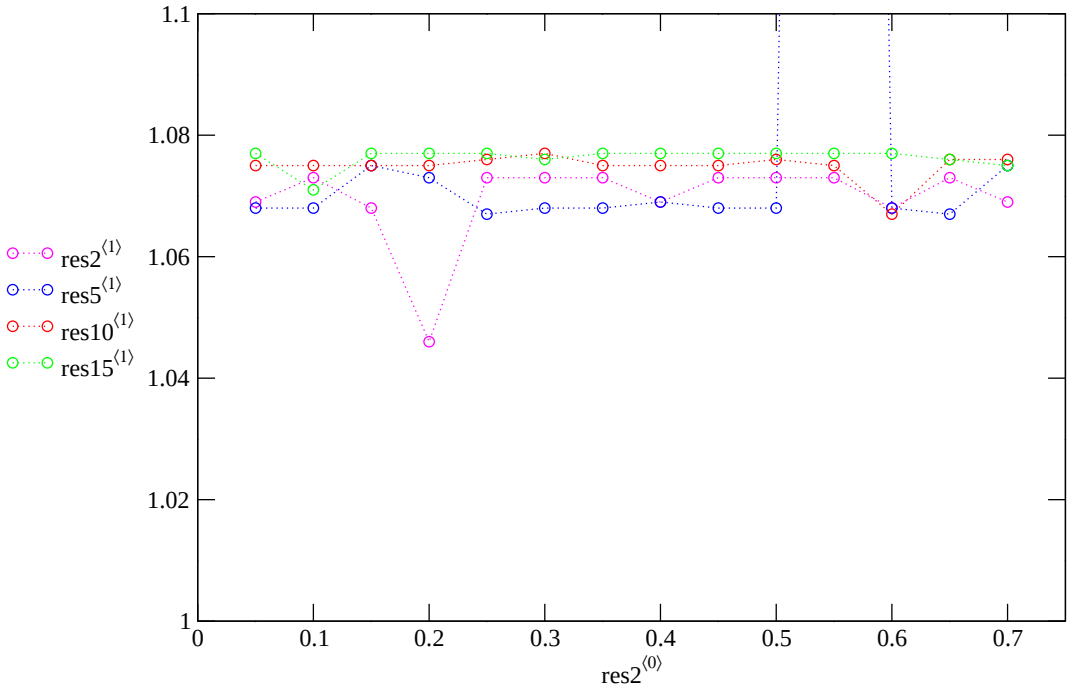

Guesses at 20% above the 'percent' level and with a centroid guess of 9.85 MeV:

$$\text{res2} := \begin{pmatrix} 0.05 & 1.073 \\ 0.1 & 1.073 \\ 0.15 & 1.075 \\ 0.2 & 1.073 \\ 0.25 & 1.073 \\ 0.3 & 1.073 \\ 0.35 & 1.073 \\ 0.4 & 1.073 \\ 0.45 & 1.069 \\ 0.5 & 1.068 \\ 0.55 & 1.074 \\ 0.6 & 1.074 \\ 0.65 & 1.074 \\ 0.7 & 1.068 \end{pmatrix} \quad \text{res5} := \begin{pmatrix} 0.05 & 1.068 \\ 0.1 & 1.068 \\ 0.15 & 1.044 \\ 0.2 & 1.066 \\ 0.25 & 1.069 \\ 0.3 & 1.044 \\ 0.35 & 1.067 \\ 0.4 & 1.049 \\ 0.45 & 1.044 \\ 0.5 & 1.067 \\ 0.55 & 1.075 \\ 0.6 & 1.068 \\ 0.65 & 1.068 \\ 0.7 & 1.067 \end{pmatrix} \quad \text{res10} := \begin{pmatrix} 0.05 & 1.076 \\ 0.1 & 1.075 \\ 0.15 & 1.075 \\ 0.2 & 1.075 \\ 0.25 & 1.076 \\ 0.3 & 1.076 \\ 0.35 & 1.066 \\ 0.4 & 1.071 \\ 0.45 & 1.067 \\ 0.5 & 1.077 \\ 0.55 & 1.066 \\ 0.6 & 1.066 \\ 0.65 & 1.067 \\ 0.7 & 1.075 \end{pmatrix} \quad \text{res15} := \begin{pmatrix} 0.05 & 1.077 \\ 0.1 & 1.077 \\ 0.15 & 1.077 \\ 0.2 & 1.077 \\ 0.25 & 1.076 \\ 0.3 & 1.077 \\ 0.35 & 1.076 \\ 0.4 & 1.092 \\ 0.45 & 1.076 \\ 0.5 & 1.077 \\ 0.55 & 1.077 \\ 0.6 & 1.076 \\ 0.65 & 1.077 \\ 0.7 & 1.071 \end{pmatrix}$$

The chi2 values are then once again plotted to identify the optimum guess parameters.

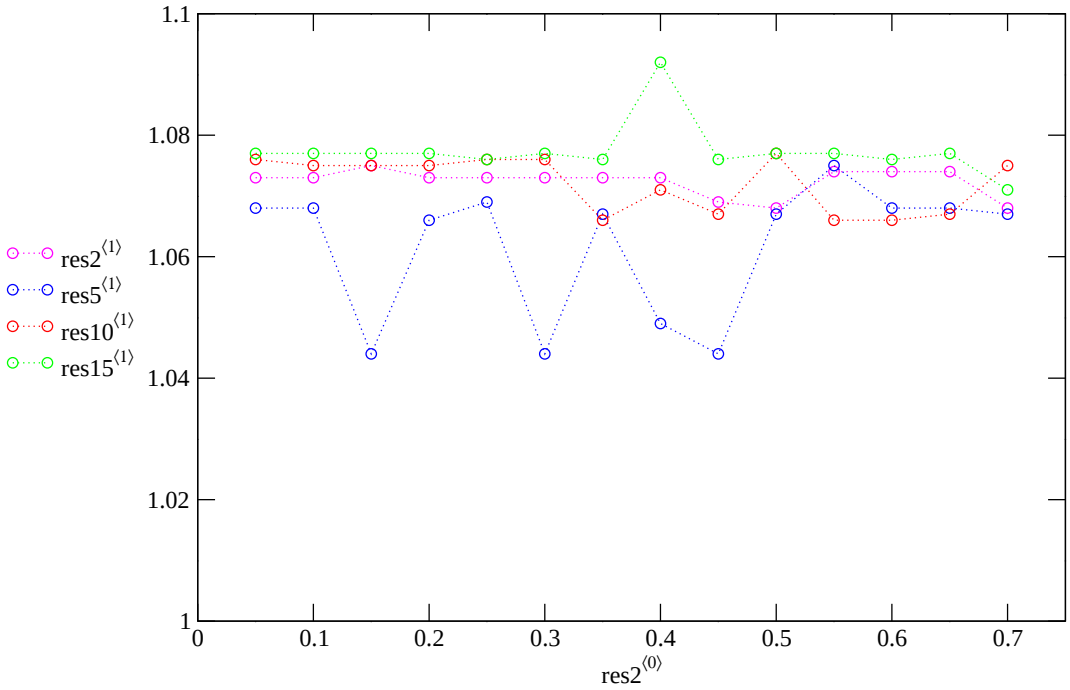

Guesses at 30% above the 'percent' level and with a centroid guess of 10.0 MeV:

$$\text{res2} := \begin{pmatrix} 0.05 & 1.049 \\ 0.1 & 1.073 \\ 0.15 & 1.049 \\ 0.2 & 1.048 \\ 0.25 & 1.068 \\ 0.3 & 1.069 \\ 0.35 & 1.073 \\ 0.4 & 1.069 \\ 0.45 & 1.069 \\ 0.5 & 5.072 \\ 0.55 & 1.069 \\ 0.6 & 1.140 \\ 0.65 & 1.069 \\ 0.7 & 1.049 \end{pmatrix} \quad \text{res5} := \begin{pmatrix} 0.05 & 1.075 \\ 0.1 & 1.069 \\ 0.15 & 1.073 \\ 0.2 & 1.067 \\ 0.25 & 1.068 \\ 0.3 & 1.075 \\ 0.35 & 1.068 \\ 0.4 & 1.068 \\ 0.45 & 1.074 \\ 0.5 & 1.068 \\ 0.55 & 1.069 \\ 0.6 & 1.068 \\ 0.65 & 1.068 \\ 0.7 & 1.067 \end{pmatrix} \quad \text{res10} := \begin{pmatrix} 0.05 & 1.076 \\ 0.1 & 1.077 \\ 0.15 & 1.075 \\ 0.2 & 1.075 \\ 0.25 & 1.075 \\ 0.3 & 1.075 \\ 0.35 & 1.067 \\ 0.4 & 1.076 \\ 0.45 & 1.074 \\ 0.5 & 1.075 \\ 0.55 & 1.075 \\ 0.6 & 1.075 \\ 0.65 & 1.075 \\ 0.7 & 1.075 \end{pmatrix} \quad \text{res15} := \begin{pmatrix} 0.05 & 1.068 \\ 0.1 & 1.077 \\ 0.15 & 1.077 \\ 0.2 & 1.078 \\ 0.25 & 1.077 \\ 0.3 & 1.076 \\ 0.35 & 1.077 \\ 0.4 & 1.077 \\ 0.45 & 1.262 \\ 0.5 & 1.077 \\ 0.55 & 1.077 \\ 0.6 & 1.077 \\ 0.65 & 1.077 \\ 0.7 & 1.077 \end{pmatrix}$$

The chi2 values are then once again plotted to identify the optimum guess parameters.

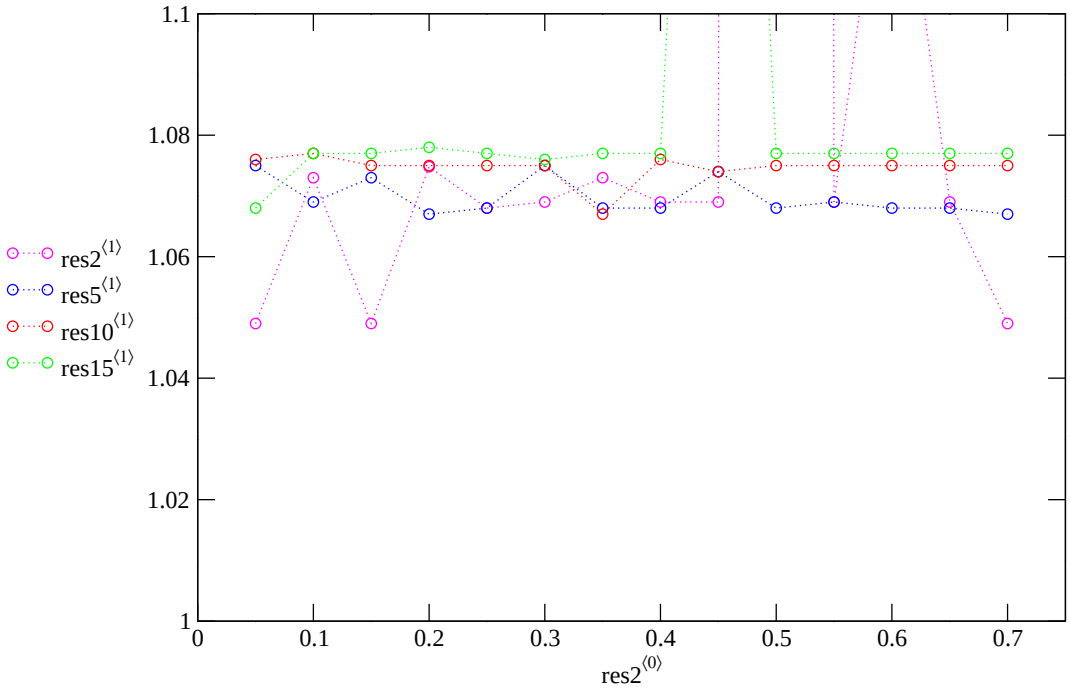

Appendix E

Publication: The search for the 2^+ excitation of the Hoyle state in ^{12}C using the ^{12}C(^{12}C,3α)^{12}C reaction

IOP Publishing Journal of Physics G: Nuclear and Particle Physics

J. Phys. G: Nucl. Part. Phys. **37** (2010) 105104 (13pp) doi:10.1088/0954-3899/37/10/105104

[This paper is not available in the digital version of the thesis]

Search for the 2^+ excitation of the Hoyle state in ^{12}C using the ^{12}C(^{12}C,3α)^{12}C reaction

T Muñoz-Britton[1], M Freer[1], N I Ashwood[1], T A D Brown[2], W N Catford[3], N Curtis[1], S P Fox[2], B R Fulton[2], C W Harlin[3], A M Laird[2], P Mumby-Croft[2], A St J Murphy[4], P Papka[2], D L Price[1], K Vaughan[2], D L Watson[2] and D C Weisser[5]

[1] School of Physics and Astronomy, University of Birmingham, Edgbaston, Birmingham B15 2TT, UK
[2] Department of Physics, University of York, Heslington, York YO10 5DD, UK
[3] Department of Physics, Faculty of Engineering and Physical Sciences, University of Surrey, Guildford GU2 7XH, UK
[4] School of Physics and Astronomy, The University of Edinburgh, James Clerk Maxwell Building, Mayfield Road, Edinburgh EH9 3JZ, UK
[5] The Research School of Physics and Engineering, Building 60, The Australian National University, Canberra ACT 0200, Australia

E-mail: tdm@np.ph.bham.ac.uk

Received 10 March 2010
Published 26 July 2010
Online at stacks.iop.org/JPhysG/37/105104

Abstract

A search for the 2^+ excitation of the Hoyle state in ^{12}C has been performed using the ^{12}C(^{12}C,3α)^{12}C reaction at a beam energy of 101.5 MeV. An angular correlation analysis was used to suppress known contributions to the excitation energy spectrum, enhancing the experimental sensitivity. No strong evidence was found for new states in ^{12}C between 9 and 11 MeV; rather upper limits for their excitation in the ^{12}C+^{12}C inelastic scattering reaction are determined.

(Some figures in this article are in colour only in the electronic version)

List of References

[1] E. Rutherford. The Scattering of α and β Particles by Matter and the Structure of the Atom. Philos. Mag., 6(21):669–688, 1911.

[2] G. Gamow. Mass Defect and Nuclear Constitution. Proc. Roy. Soc., A126:632–644, 1930.

[3] J. Chadwick. The Existence of the Neutron. Proc. Roy. Soc., A 136:692–708, 1932.

[4] J. A. Wheeler. Wave Functions for Large Arguments by the Amplitude-Phase Method. Phys. Rev., 52(11):1123–1127, Dec 1937.

[5] W. Wefelmeier. Zeit. f. Physik, 107:332, 1937.

[6] C. F. von Weizsacker. Naturwiss, 26:209, 1938.

[7] L. R. Hafstad and E. Teller. The Alpha-Particle Model of the Nucleus. Phys. Rev., 54(9):681–692, Nov 1938.

[8] D. M. Brink. Nucl. Phys. A, 91, 1967.

[9] H. Morinaga. Interpretation of some of the excited states of $4n$ self-conjugate nuclei. Phys. Rev., 101(1):254–258, Jan 1956.

[10] K. Ikeda, N. Tagikawa, and H. Horiuchi. The Systematic Structure-Change into the Molecule-like Structures in the Self-Conjugate 4n Nuclei. Prog. Theor. Phys. (Suppl.), (464), 1968.

[11] M Freer. The clustered nucleus - cluster structures in stable and unstable nuclei. Rep. Prog. Phys., 70(12):2149–2210, Dec 2007.

[12] D.M. Brink and J.J. Castro. Alpha clustering effects in nuclear matter. Nucl. Phys., A216:109–124, Nov 1973.

[13] B. Buck, C. B. Dover, and J. P. Vary. Simple potential model for cluster states in light nuclei. Phys. Rev. C, 11(5):1803–1821, May 1975.

[14] K. A. Erb, R. R. Betts, S. K. Korotky, M. M. Hindi, P. P. Tung, M. W. Sachs, S. J. Willett, and D. A. Bromley. Resonant and average behavior of the ^{12}C + ^{12}C total reaction cross section: $5.6 \leq E_{c.m.} \leq 10.0$ MeV. Phys. Rev. C, 22(2):507–514, Aug 1980.

[15] T. M. Cormier. Annu. Rev. Nucl. Part. Sci., 32:271–308, 1982.

[16] K. A. Erb and D. A. Bromley. Rotational and vibrational excitations in nuclear molecular spectra. Phys. Rev. C, 23(6):2781–2784, Jun 1981.

[17] R. B. Wiringa, Steven C. Pieper, J. Carlson, and V. R. Pandharipande. Quantum Monte Carlo calculations of $A = 8$ nuclei. Phys. Rev. C, 62(1):014001, Jun 2000.

[18] H. Horiuchi and Y. Kanada-En'yo. Structure of light exotic nuclei studied with AMD model. Nuclear Physics A, 616(1-2):394 – 405, 1997. Radioactive Nuclear Beams.

[19] Y. Kanada-En'yo and H. Horiuchi. Prog. Theor. Phys. Suppl. (Japan), 143:205, 2001.

[20] M. Chernykh, H. Feldmeier, T. Neff, P. von Neumann-Cosel, and A. Richter. Structure of the Hoyle State in ^{12}C. Phys. Rev. Lett., 98(3):032501, Jan 2007.

[21] P. Navrátil, J. P. Vary, and B. R. Barrett. Properties of ^{12}C in the Ab Initio Nuclear Shell Model. Phys. Rev. Lett., 84(25):5728–5731, Jun 2000.

[22] F. Hoyle. Resonances and nuclear molecular configurations in heavy-ion reactions. Astrophys. J. (Suppl.), 1:12, 1954.

[23] E. Margaret Burbidge, G. R. Burbidge, William A. Fowler, and F. Hoyle. Synthesis of the Elements in Stars. Rev. Mod. Phys., 29(4):547–650, Oct 1957.

[24] Brink, D. M. and Castro, J. J. Nucl. Phys., A 216(109), 1967.

[25] Crannell, H. and O'Brien, J. T. and Sober, D. I. Proc. Int. Conf. On Nuclear Physics with Electromagnetic Interactions, Mainz, 1979.

[26] A. C. Merchant and W. D. M. Rae. Systematics of alpha-chain states in 4N-nuclei. Nuclear Physics A, 549(3):431 – 438, 1992.

[27] N. De Takacsy and S. Das Gupta. Can the 7.65 MeV 0^+ state in ^{12}C belong to a linear chain of α-clusters? Physics Letters B, 33(8):556 – 558, 1970.

[28] H. Friedrich, L. Satpathy, and A. Weiguny. Why is there no rotational band based on the 7.65 MeV 0^+ state in ^{12}C? Physics Letters B, 36(3):189 – 192, 1971.

[29] N. De Takacsy. The structure of ^{12}C in a cluster model with varying hinge angle. Nuclear Physics A, 178(2):469 – 478, 1972.

[30] A. Tohsaki, H. Horiuchi, P. Schuck, and G. Röpke. Alpha Cluster Condensation in ^{12}C and ^{16}O. Phys. Rev. Lett., 87(19):192501, Oct 2001.

[31] P. Chevallier, F. Scheibling, G. Goldring, I. Plesser, and M. W. Sachs. Breakup of ^{16}O into ^{8}Be + ^{8}Be. Phys. Rev., 160(4):827–834, Aug 1967.

[32] F. Brochard, P. Chevallier, D. Disdier, V. Rauch, G. Rudolf, and F. Scheibling. ^{12}C(α,^{8}Be)^{8}Be reaction in the energy range $E_\alpha = 17-33$ MeV. Phys. Rev. C, 13(3):967–975, Mar 1976.

[33] Betts R. R. Proc. 6th Int. Conf. on Cluster in Nuclear Structure and Dynamics (Strasbourg), 1994.

[34] Bromley D. A. Proc. 4th Int. Conf. on Clustering Aspects of Nuclear Structure and Nuclear Reactions (Chester, UK), 1, 1985.

[35] B. Buck, J. C. Johnston, A. C. Merchant, and S. M. Perez. Unified treatment of scattering and cluster structure in α + closed shell nuclei: ^{20}Ne and ^{44}Ti. Phys. Rev. C, 52(4):1840–1844, Oct 1995.

[36] Horiuchi H. and Ikeda K. A Molecule-like Structure in Atomic Nuclei of $^{16}O^*$ and ^{10}Ne. Prog. Theor. Phys., 40(2):277–287, 1968.

[37] P. A. Butler and W. Nazarewicz. Intrinsic reflection asymmetry in atomic nuclei. Rev. Mod. Phys., 68(2):349–421, Apr 1996.

[38] Kanada-En'yo Y. and Horiuchi H. Clustering in Yrast States of ^{20}Ne Studied with Antisymmetrized Molecular Dynamics. Prog.Theor.Phys., 93(1):115–136, 1995.

[39] T. Tomoda and A. Arima. Coexistence of shell structure and cluster structure in ^{20}Ne. Nuclear Physics A, 303(1-2):217 – 253, 1978.

[40] D. G. Kovar, D. F. Geesaman, T. H. Braid, Y. Eisen, W. Henning, T. R. Ophel, M. Paul, K. E. Rehm, S. J. Sanders, P. Sperr, J. P. Schiffer, S. L. Tabor, S. Vigdor, B. Zeidman, and F. W. Prosser. Systematics of carbon- and oxygen-induced fusion on nuclei with $12 \leq A \leq 19$. Phys. Rev. C, 20(4):1305–1331, Oct 1979.

[41] Y. Funaki, A. Tohsaki, H. Horiuchi, P. Schuck, and G. Röpke. Analysis of previous microscopic calculations for the second 0^+ state in ^{12}C in terms of 3α-particle Bose-condensed state. Phys. Rev. C, 67(5):051306, May 2003.

[42] P. Descouvemont and D. Baye. Microscopic theory of the $^8\mathrm{Be}(\alpha,\gamma)^{12}\mathrm{C}$ reaction in a three-cluster model. Phys. Rev. C, 36(1):54–59, Jul 1987.

[43] H. O. U. *et al.* Fynbo. Revised rates for the stellar triple-α process from measurement of ^{12}C nuclear resonances. Phys. Rev. C, 36(1):54–59, Jul 1987.

[44] M. *et al.* Itoh. Study of the cluster state at E_x=10.3 MeV in ^{12}C. Nucl. Phys. A, 738:268, 2004.

[45] M. Freer, H. Fujita, Z. Buthelezi, J. Carter, R. W. Fearick, S. V. Förtsch, R. Neveling, S. M. Perez, P. Papka, F. D. Smit, J. A. Swartz, and I. Usman. 2^+ excitation of the ^{12}C Hoyle state. Phys. Rev. C, 80(4):041303, Oct 2009.

[46] T. Muñoz and N. Sparks. MSci report. (Unpublished), 2007.

[47] K. S. Krane. Introductory Nuclear Physics. John Wiley & Sons, 1988.

[48] A. H. Wapstra and K. Bos. The 1977 atomic mass evaluation: in four parts. Atomic Data and Nuclear Data Tables, 19(3):175 – 176, 1977.

[49] B. Buck, H. Friedrich, and C. Wheatley. Local potential models for the scattering of complex nuclei. Nuclear Physics A, 275(1):246 – 268, 1977.

[50] J. Hiura and R. Tamagaki. Alpha-Like Four-Body Correlations and Molecular Aspects in Nuclei. Chapter II. Typical Realization of Alpha-Particle-Model Aspects in Beryllium Region. Suppl. Prog. Theor. Phys., 52(25), 1972.

[51] J. Zhang and W.D.M. Rae. Systematics of 2-dimensional α-cluster configurations in 4N nuclei from ^{12}C to ^{44}Ti. Nuclear Physics A, 564(2):252 – 270, 1993.

[52] C. Bremner. New High Spin Resonances in ^{12}C + ^{12}C Scattering. PhD thesis, University of Oxford, 1995.

[53] M. Freer. The Analysis of Angular Correlations in Breakup Reactions: The effect of coordinate geometries. Nucl. Instrum. Methods Phys. Res., A383:463, 1996.

[54] E. F. Da Silviera. Proc. 14th Winter Meeting on Nuclear Physics (Borneo). 1976.

[55] Dec 2010. http://physics.anu.edu.au/nuclear/.

[56] S. P. G. Chappell, W. D. M. Rae, and P. M. Simmons. Calibration of position sensitive detectors with low-energy elastic scattering. Nuclear Instruments and Methods in Physics Research Section A: Accelerators, Spectrometers, Detectors and Associated Equipment, 396(3):383 – 387, 1997.

[57] S. Chappell. New High Spin Resonances in ^{12}C +^{12} C Scattering. PhD thesis, University of York, 1995.

[58] S. Singer. SunSort Reference Manual (http://npg.dl.ac.uk/MIDAS/manual/SunSort/index.html).

[59] H. A. Bethe. Ann. Physik, 5:325, 1930.

[60] F. Bloch. Ann. Physik, 16:285, 1933.

[61] M. Freer. Measurements of the Spins of Symmetrically Fissioning States in ^{24}Mg. PhD thesis, 1991.

[62] S. Hyldegaard, M. Alcorta, B. Bastin, M. J. G. Borge, R. Boutami, S. Brandenburg, J. Büscher, P. Dendooven, C. Aa. Diget, P. Van Duppen, T. Eronen, S. P. Fox, L. M. Fraile, B. R. Fulton, H. O. U. Fynbo, J. Huikari, M. Huyse, H. B. Jeppesen, A. S. Jokinen, B. Jonson, K. Jungmann, A. Kankainen, O. S. Kirsebom, M. Madurga, I. Moore, A. Nieminen, and T. Nilsson. R-matrix analysis of the β decays of ^{12}N and ^{12}B. Phys. Rev. C, 81(2):024303, Feb 2010.

[63] C. Aa. Diget and F. C. Barker and M. J. G. Borge and J. Cederkäll and V. N. Fedosseev and L. M. Fraile and B. R. Fulton and H. O. U. Fynbo and H. B. Jeppesen and B. Jonson and U. Kster and M. Meister and T. Nilsson and G. Nyman and Y. Prezado and K. Riisager and S. Rinta-Antila and O. Tengblad and M. Turrion and K. Wilhelmsen and J. Äystö. Properties of the ^{12}C 10 MeV state determined through β-decay. Nuclear Physics A, 760(1-2):3 – 18, 2005.

[64] W. R. Zimmerman, N. E. Destefano, M. Freer, M. Gai, and F. D. Smit. Further Evidence for the broad 2_2^+ at 9.6 MeV in ^{12}C. Awaiting Publication, 2011.